MODELING AND DESIGN OF ARCHITECTURES FOR HIGH-SPEED ADC-BASED SERIAL LINKS

A Dissertation

by

SHIVA KIRAN

Submitted to the Office of Graduate and Professional Studies of
Texas A&M University
in partial fulfillment of the requirements for the degree of

DOCTOR OF PHILOSOPHY

Chair of Committee,	Sebastian Hoyos
Co-Chair of Committee,	Samuel Palermo
Committee Members,	Sunil Khatri
	Jorge Alvarado
Head of Department,	Miroslav M. Begovic

December 2018

Major Subject: Electrical Engineering

ABSTRACT

There is an ongoing dramatic rise in the volume of internet traffic. Standards such as 56Gb/s OIF very short reach (VSR), medium reach (MR) and long reach (LR) standards for chip to chip communication over channels with up to 10dB, 20dB and 30dB insertion loss at the PAM-4 Nyquist frequency, respectively, are being adopted. These standards call for the spectrally efficient PAM-4 signaling over NRZ signaling. PAM-4 signaling offers challenges such as a reduced SNR at the receiver, susceptibility to nonlinearities and increased sensitivity to residual ISI. Equalization provided by traditional mixed signal architectures can be insufficient to achieve the target BER requirements for very long reach channels. ADC-based receiver architectures for PAM-4 links take advantage of the more powerful equalization techniques, which lend themselves to easier and robust digital implementations, to extend the amount of insertion loss that the receiver can handle. However, ADC-based receivers can consume more power compared to mixed-signal implementations. Techniques that model the receiver performance to understand the various system trade-offs are necessary.

This research presents a fast and accurate hybrid modeling framework to efficiently investigate system trade-offs for an ADC-based receiver. The key contribution being the addition of ADC related non-idealities such as quantization noise in the presence of integral and differential nonlinearities, and time-interleaving mismatch errors such as gain mismatch, bandwidth mismatch, offset mismatch and sampling skew.

The research also presents a 52Gb/s ADC-based PAM-4 receiver prototype employing a 32-way time-interleaved, 2-bit/stage, 6-bit SAR ADC and a DSP with a 12-tap FFE and a 2-tap DFE. A new DFE architecture that reduces the complexity of a PAM-4 DFE to that of an NRZ

DFE while simultaneously nearly doubling the maximum achievable data rate is presented. The receiver architecture also includes an analog front-end (AFE) consisting of a programmable two stage CTLE. A digital baud-rate CDR's utilizing a Mueller-Muller phase detector sets the sampling phase. Measurement results show that for 32Gb/s operation a BER $< 10^{-9}$ is achieved for a 30dB loss channel while for 52 Gb/s operation achieves a BER $< 10^{-6}$ for a 31dB loss channel with a power efficiency of 8.06pj/bit.

ACKNOWLEDGEMENTS

Finally, I would like to thank my parents and my sister for being the pillars on which I can stand securely. I am indebted for their unconditional love and support and for that I dedicate this dissertation to them.

CONTRIBUTORS AND FUNDING SOURCES

Contributors

This work was supported by a dissertation committee consisting of Professor Sebastian Hoyos (advisor), Professor Samuel Palermo (co-advisor) and Professor Sunil Khatri of the Department of Electrical and Computer Engineering and Professor Jorge Alvarado of Department of Engineering Technology and Industrial Distribution.

Funding Sources

TABLE OF CONTENTS

LIST OF FIGURES

LIST OF TABLES

Page

1. INTRODUCTION

With IOT and cloud computing becoming ubiquitous, there has been an explosion in the bandwidth demand placed on servers and routers operating over legacy channels. In order to tackle the significant frequency dependent attenuation encountered on these legacy channels, PAM-4 signaling is emerging as the choice of modulation format, particularly, for medium reach (MR) and long reach (LR) links. Several recent designs [1-6] employ ADC based receiver architectures for PAM-4 links to take advantage of process scaling and process, voltage and temperature (PVT) robustness of the CMOS process in the DSP. These architectures employs a DSP followed by an ADC as shown in Fig. 1.1. The more powerful equalization techniques that lend themselves to easier digital implementations extend the amount of insertion loss that the receiver can handle in comparison to mixed signal implementations. Despite these advantages, ADC-based serial links are generally more complex and consume more power than mixed signal serial links. Both the ADC and the DSP can consume significant amount of power which is often prohibitive for systems where link power efficiency is the key metric. This motivates the development of a fast and reliable modeling framework to efficiently investigate system trade-offs and determine the optimal ADC resolution and digital equalization complexity.
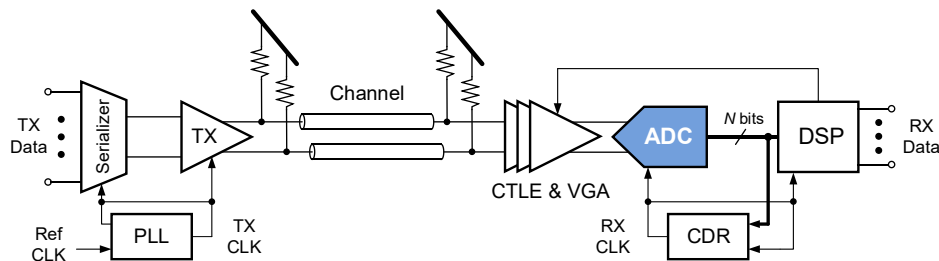
Figure 1.1. ADC-based serial link.

1

Moreover, efficient modeling techniques approaches can quantify the effectiveness of system and circuit techniques used to save power in ADC-based links such as partial analog pre-equalization embedded in the ADC. Time-domain Monte Carlo (transient) simulations are impractical for system performance prediction for typical BER $< 10^{-12}$ since the simulation time and memory requirements would be impractically large. Worst case methodologies like peak distortion analysis are pessimistic and result in over design [7]. For these reasons, today's high-speed links employs statistical tools for predicting system performance [8-10]. Since these statistical tools were developed for mixed signal links, they do not model several ADC related non-idealities. Efficient modeling techniques that capture ADC quantization noise, integral and differential non-linearity (INL/DNL), and time-interleaving mismatches are necessary to determine key ADC specifications and digital equalization complexity.

In ADC based links, traditionally, a baud rate linear feed-forward equalizer (FFE) is cascaded with a non-linear decision feedback equalizer (DFE) to equalize the channel [1, 11]. NRZ modulation is commonly employed but as data rates continue to increase, more bandwidth efficient modulation schemes such as PAM-4 have to be employed in order to compensate the severe attenuation introduced by the channel. The Nyquist frequency of PAM-4 modulation is half of that of NRZ modulation and hence is more bandwidth efficient. However, PAM-4 modulation has its own drawbacks in terms of the receiver complexity. While PAM-4 modulation relaxes the bandwidth requirement of the analog-front end and reduces the ADC sampling rate requirement by half, the DSP complexity can grow significantly. The linear FFE is modulation format agnostic and it is primarily the DFE complexity that suffers when PAM-4 modulation is employed. The DFE has a timing loop whose timing requirements can be very challenging to meet. Traditional techniques such as parallel implementation and pipelining do not solve the critical timing path

2

issue in the DFE. This necessitates the use of techniques such loop-unrolling and look-ahead multiplexing. While these techniques successfully solve the critical timing path issue in the DFE, their complexity grows exponentially for each additional tap of the DFE. The number of summers and digital comparators in a PAM-4 DFE grows as 4^N where N is the number of DFE taps as opposed to 2^N as in an NRZ-DFE implementation. The number of multiplexers needed for a look-ahead implementation also grows as 4^N. This requires the investigation in to a new PAM-4 DFE architecture that can simplify the DFE architecture.

Forward error correction (FEC) is of interest in serial links employing PAM-4 modulation to relax the stringent equalization and non-linearity requirements. However, decoders for well-known error correction codes such as the RS and BEC codes can be power hungry and more importantly introduce large latency.

ADC-based serial links employ some equalization in the analog-front end in the form a CTLE or embed low-overhead equalization inside the ADC. Previous work [11] has utilized the information in the partially equalized signal to determine whether a symbol requires further equalization or if a decision can be reliably made with no further equalization. This allows the digital equalizer power to be gated on a symbol by symbol basis leading to considerable power savings in the DSP. This principle can be also be utilized to employ simple error correction techniques without the power and latency overhead introduced by more complex coding schemes. Timing errors in the form of jitter are another major impairment as data rates continue to scale. While time-interleaved ADCs relax the sampling frequency for each track and hold, each time-interleaved channel still samples the full bandwidth signal. Hence, the jitter induced noise in time-interleaved system is the same as a single channel system. Frequency channelized receivers are promising architectures for providing jitter robustness.

3

This dissertation is organized as follows. Chapter 2 presents background material on high speed serial link systems including the impairments introduced by the various compoments that make up the channel and the techniques available at the receiver to combat these impairments. It also introduces the existing mixed-signal statistical modeling techniques to predict system performance.

Chapter 3 presents a hybrid statistical framework for ADC-based serial links receivers. The framework builds upon existing statistical modeling techniques for mixed-signal receivers and adds the support of ADC quantization noise, radix errors (INL/DNL) and time-interleaving mismatch errors. The results of the statistical model are compared with transient simulation to verify the modeling technique.

Chapter 4 presents a 52Gb/s PAM-4 ADC-based receiver that employs a 32-way time-interleaved 6-bit SAR ADC and DSP architectures which utilize the information in the partially equalized signal to simplify the loop-unrolled PAM-4 DFE complexity to that of an NRZ DFE while simultaneously nearly doubling data rate. Circuit design details and measurement results that verify the performance of a prototype in GP 65nm process are presented.

Chapter 5 presents a bit erasure filling architecture that can relax both the analog front-end and the DSP design by targeting a higher raw pre-erasure filled BER. Chapter 5 also presents a frequency domain ADC-based receiver architecture that can support multi-tone modulation to provide robustness to jitter.

2. BACKGROUND

This chapter introduces the topic of modeling and design of high-speed ADC-based serial link receivers. The primary challenge of high speed data transmission through a lossy channel utilizing less than perfect circuit blocks and the consequent necessity of accurately modeling the channel and circuit imperfections are presented. Various available choices for modulation techniques, equalization architectures and their implementation styles, and their relative trade-offs are also presented.

2.1 Channel Components and Characteristics

A typical backplane serial link along with its constituent components such as the IC package, connector, vias, and the backplane trace is shown in Fig. 2.1 [12]. Each of these components can introduce dispersion and reflections which leads to symbols transmitted in different time intervals interfering with each other. This is known as inter-symbol interference (ISI) and constitutes the main challenge of signaling at high data rates over a bandlimited channel.
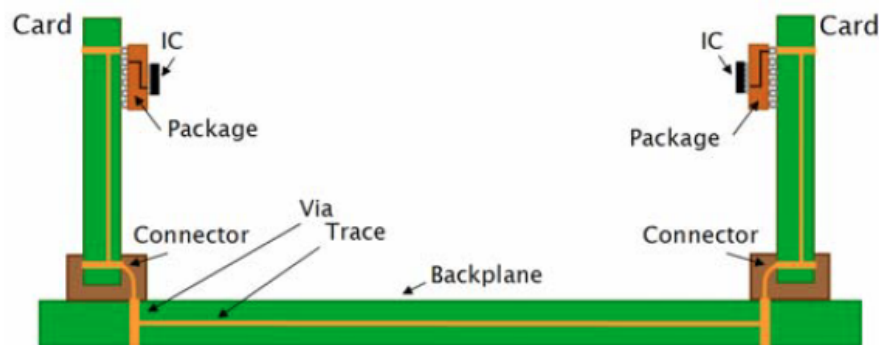
Figure 2.1. A typical backplane link.
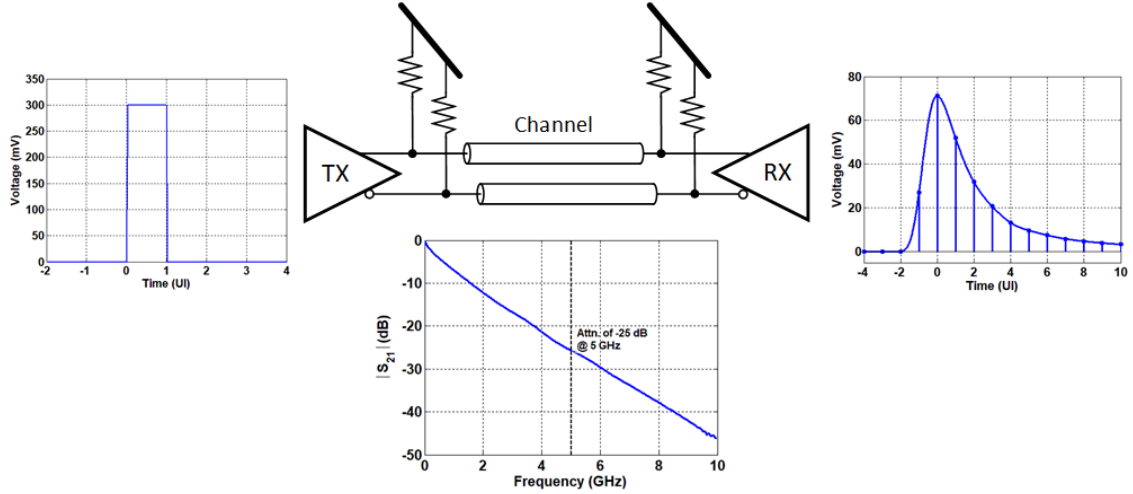
Figure 2.2. Link system model showing a transmitter, an effective channel and a receiver. Also shown is the dispersion of a pulse at the receiver as it travels through the channel.

While the IC package, connectors, and vias are primarily responsible for reflections due to the impedance discontinuities that these components introduce the backplane trace introduces dispersion due to its frequency dependent loss and non-linear phase characteristics. The frequency dependent loss of the backplane trace in turn results from physical phenomenon such as skin effect and dielectric absorption. The entire link can be modeled as a transmitter and receiver connected through a lossy, reflective equivalent channel comprising of all the components previously described as shown in Fig 2.2. A pulse at the transmitter occupying one symbol interval or unit interval (UI) of time, which is 100ps in the example of Fig. 2.2 spreads out into several UIs at the receiver as it travels over a channel, which has a loss of 25dB at 5GHz in this example. The signal at the receiver can be written as

$$z(t) = \sum_k b_k c(t - kT) + w(t), \qquad (2.1)$$

where b_k is the transmitted symbol, k is the symbol index, T is the symbol period, and $c(t)$ is the channel pulse response that is extracted by convolving the channel impulse response with a single

6

pulse similar to the pulse on the transmitter side in Fig. 2.2 and $w(t)$ is a additive white Gaussian

noise (AWGN) term. After sampling, t is replaced by nT and the received signal can be written as

$$z(n) = \sum_k b_k c(n-k) + w(n). \tag{2.2}$$

Equation 2.2 can be re-written to separate out the desired received signal from the ISI as in

Equation 2.3, where the second term represents the ISI and third term represents the additive noise

term.

$$z(n) = b_n c(0) + \sum_{k \neq n} b_k c(n-k) + w(n). \tag{2.3}$$

Now that it has been identified that the impact of the channel is to introduce ISI, techniques

to combat this ISI at the receiver are introduced in the next section.

2.2 Receiver Equalization Techniques

Receiver architectures can be classified as mixed-signal architectures and ADC-based

architectures. Both mixed-signal receivers and ADC-based receivers employ equalization that can

be broadly divided into linear equalization and non-linear equalization. Examples of linear

equalization are continuous time linear equalizers (CTLE) and discrete time finite impulse

response (FIR) equalizers. Examples of non-linear equalizers are decision feedback equalizers

(DFE) and maximum-likelihood sequence estimation (MLSE). It should be noted that while the

FIR equalizer and the DFE are symbol-symbol equalizers, the MLSE equalizer operates on

sequences of received symbols and hence can be thought of as belonging to a different class of

equalizers compared to the FIR equalizer and the DFE. While mixed-signal receivers mainly

employ CTLE and DFE (both FIR and IIR feedback), ADC-based receivers employ some analog

equalization before the ADC in the form of a CTLE and an optional discrete time FIR filter

followed by a powerful linear feedforward equalizer (FFE) and DFE in the digital domain in the DSP.

2.2.1 Linear Equalizers

A commonly employed linear equalizer is the CTLE that can effectively cancel both the precursor and postcursor ISI components by having a frequency response that inverts the channel's frequency dependent loss. Further, the CTLE can also be employed to cancel the long ISI tail caused by channel's loss at relatively low frequencies [13]. The CTLE can be implemented either through passive elements [4] or as an active circuit as shown in Fig. 2.3(a) and Fig. 2.3(b) respectively with the passive CTLE providing better linearity than the active CTLE. The zero for the passive CTLE is given by $w_z = {}^1\!/_{R_1 C_1}$ while the pole is given by $w_p = {}^1\!/_{(R_1||R_2)C_1}$ leading to a gain peaking of $1 + {}^{R_1}\!/_{R_2}$. The passive CTLE, however, attenuates the signal at low frequencies instead of providing a gain at high frequencies. The active CTLE is commonly realized using a source degenerated differential amplifier with the zero and the poles given by $w_z = {}^1\!/_{R_s C_s}$ and $w_{p1} = {}^1\!/_{R_D C_D}$ and $w_{p2} = {}^{1 + gmR_s}\!/_{R_s C_s}$ where gm is the transconductance of the differential pair. Discrete time FIR filters can be realized using analog delay elements as in [14-15] or can be realized in an efficient manner using an embedded capacitive DAC in a SAR ADC [16]. When analog linear equalization is provided either through a CTLE, a discrete time FIR equalizer or an embedded FFE, it can potentially lead to lower resolution requirements for the ADC or fewer digital FFE taps in an ADC-based receiver. Simulation results in Fig. 2.4 shows the receiver voltage margin for 56Gb/s operation over a channel with 37.2dB loss at 14GHz for 3 different CTLE-based analog front-end frequency responses (Fig. 2.4(a)) as a function of ADC resolution (Fig. 2.4(b)) and number of FFE taps (Fig.2.4(c)).
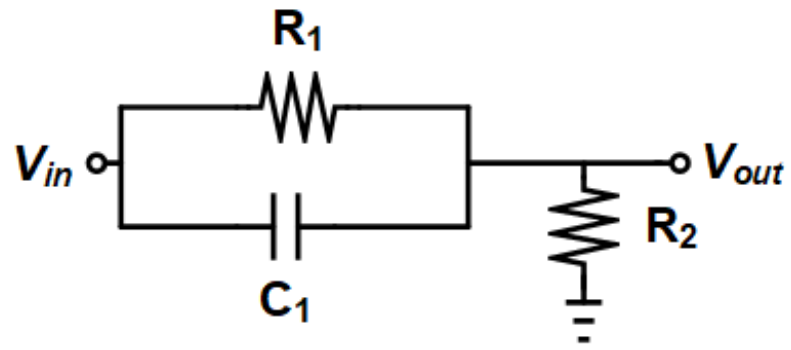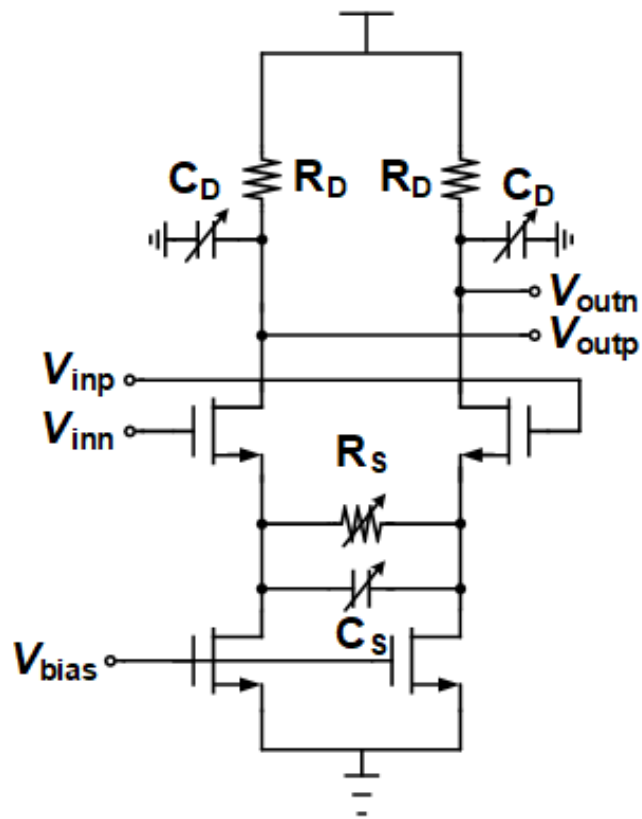
Figure 2.3. (a) Passive and (b) Active realization of a CTLE.

(a)

(b)

10
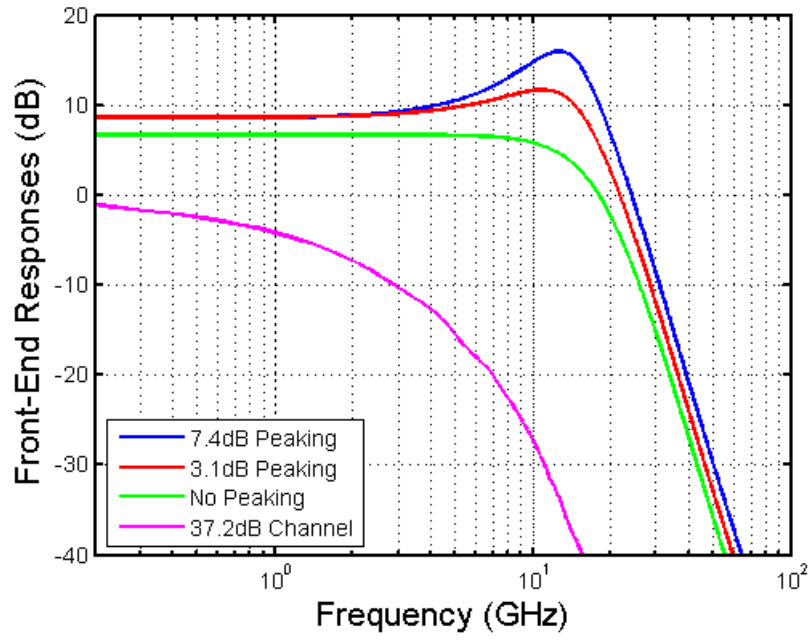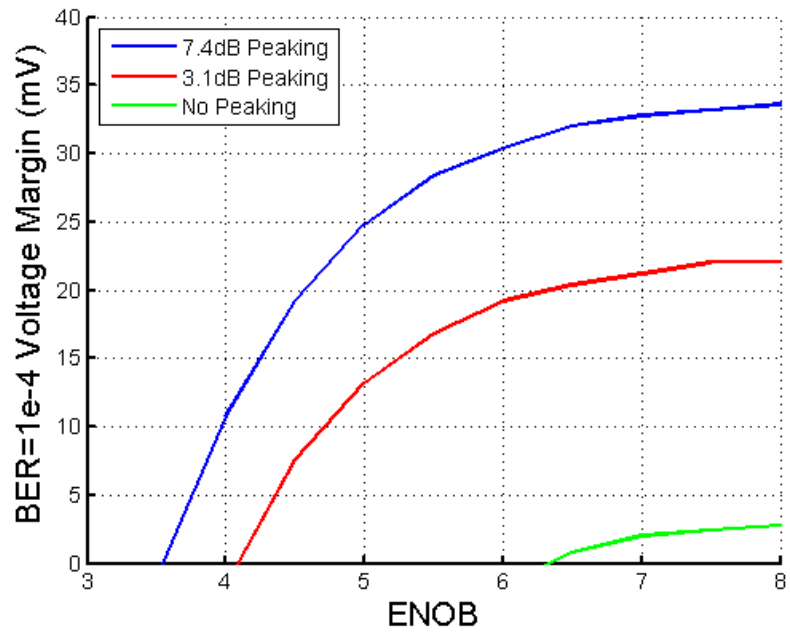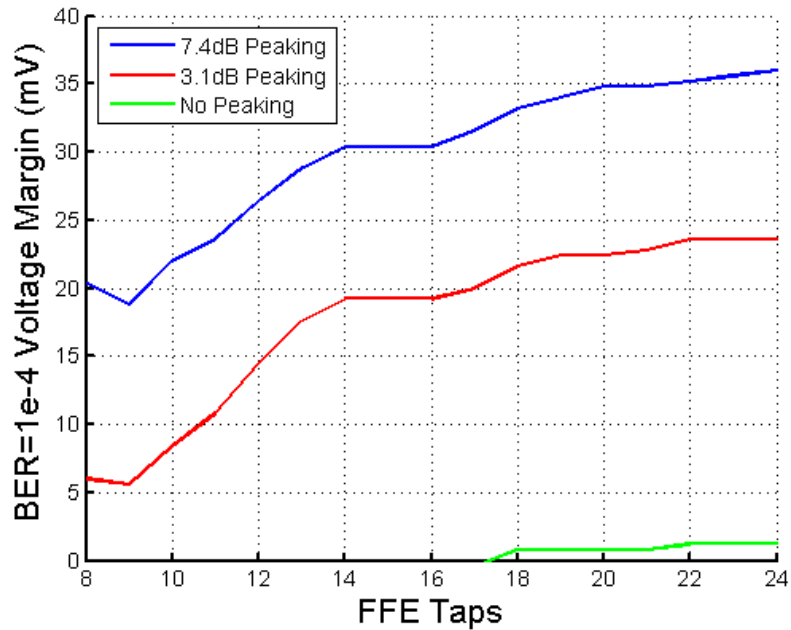
(c)

Figure 2.4. (a) A channel with 37.2dB loss at 14GHz 3 different CTLE-based analog front-end frequency responses and their impact on voltage margin for a BER of 10^{-4} for various (b) ADC resolutions and number of (c) digital FFE tap counts.

These simulation results assume 56Gbps operation utilizing PAM-4 modulation with a 1V peak to peak swing and a 3-tap FIR equalizer at the transmitter. A Random jitter of 300fs$_{rms}$ is also assumed.

FFEs render themselves to be very suitable for digital implementations and are as such the most commonly employed for of equalization in ADC-based receivers. As mentioned earlier, FFEs are symbol-by-symbol linear equalizers and their conceptual full rate implementation is shown in Fig 2.5. FFEs can be effectively pipelined and implemented in a parallel architecture as shown in Fig. 2.6, leading to relaxed timing requirements. The relaxed timing requirements can be exploited through power scaling to improve the FFEs power efficiency.

11
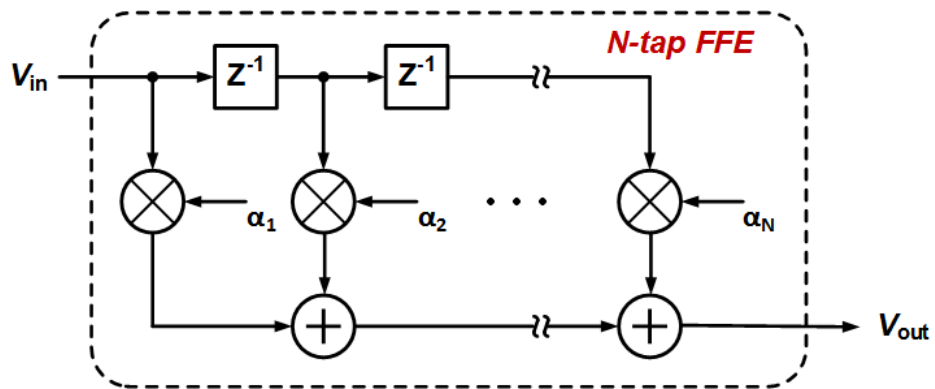
Figure 2.5. Conceptual full rate implementation of a digital FFE.
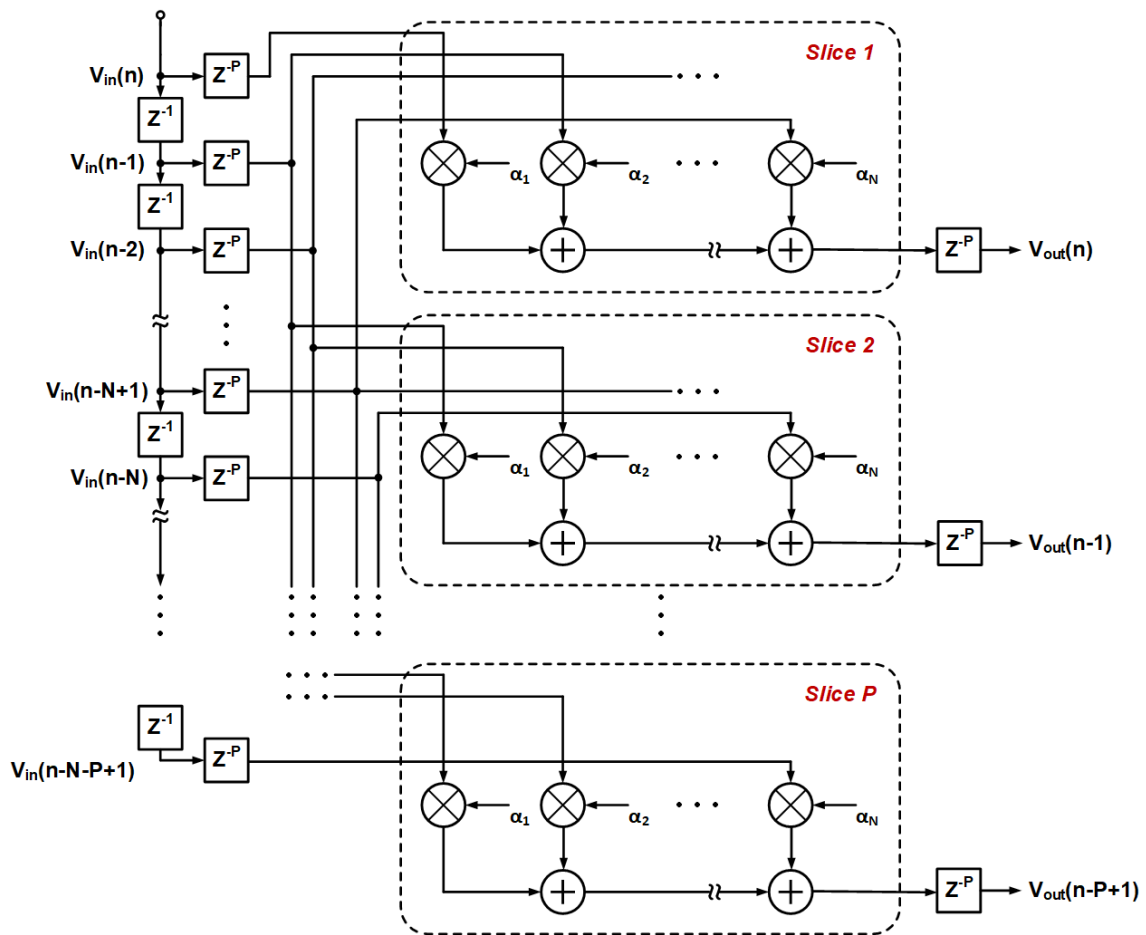
Figure 2.6. A P-way parallel implementation of a digital FFE.

A well-known drawback of linear equalizers is that not only do they cancel ISI, but they also amplify noise and crosstalk. Since linear equalizers invert the channel response, frequencies at which the channel has notches in its magnitude response can have large gain peaks in the linear equalizers frequency response significantly amplifying noise and crosstalk. Hence, while linear equalizers are effective at cancelling ISI in well behaved channels they are inadequate in channels with spectral notches that can result from reflections due to connectors and via stubs. A non-linear equalizer like the DFE can overcome this drawback and hence are commonly used in both mixed-signal and ADC-based receivers.

2.2.2 Non-Linear Equalizers

One example of a non-linear equalizer is the DFE. The DFE offers significant advantage over a linear equalizer since it can cancel postcursor ISI without noise and crosstalk amplification. Once the decision of a symbol becomes available at the output of the slicer, it is fedback into a multiplier with one symbol delay.
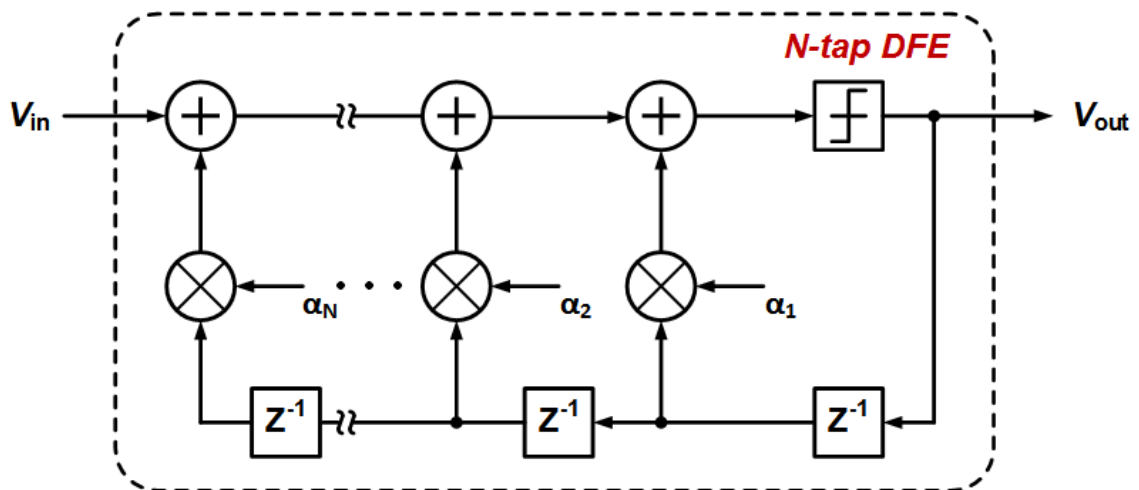
Figure 2.7. N-tap conceptual full rate DFE implementation.

The decision is multiplied with a DFE coefficient and this value is subtracted from the newly arrived symbol. If the DFE coefficient is equal to the first postcursor ISI value then essentially the postcursor ISI value is removed from the newly arrived symbol. Several decision can be fedback as shown in Fig. 2.7 to cancel multiple postcursor ISI terms. Since the DFE can only cancel postcursor ISI, an FFE-DFE combination is frequently used with their taps co-optimized. The impact of having a DFE is illustrated in the simulation results of Fig. 2.8. A data rate of 64Gb/s and PAM-4 modulation is assumed with the transmitter swing being 0.9 V_{ppd}. A CTLE with 15dB of peaking at 16GHz and 3-taps of embedded FFE provide analog equalization. A receiver jitter random jitter of 300fs$_{rms}$ and a random noise of 3 mV$_{rms}$ at the ADC input is also assumed. The ADC has a resolution of 6-bits and is followed by a DSP with a FFE-DFE equalizer. Comparing Fig. 2.8(b) and Fig. 2.8(c) it can be seen that increasing the number of FFE taps beyond 19 taps brings about very little improvement in the BER. At this point, the BER is limited by the SNR. However by introducing a DFE and optimizing the FFE taps with the DFE improves the BER significantly.

(a)

14
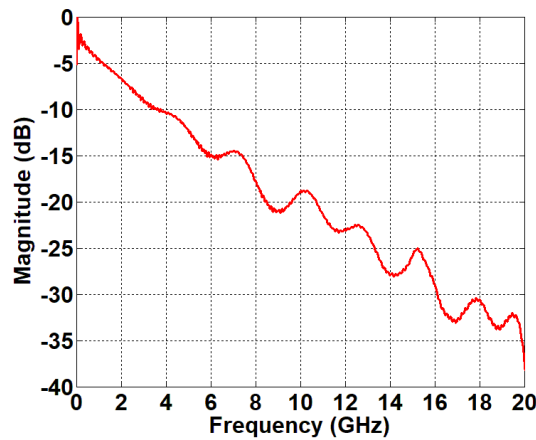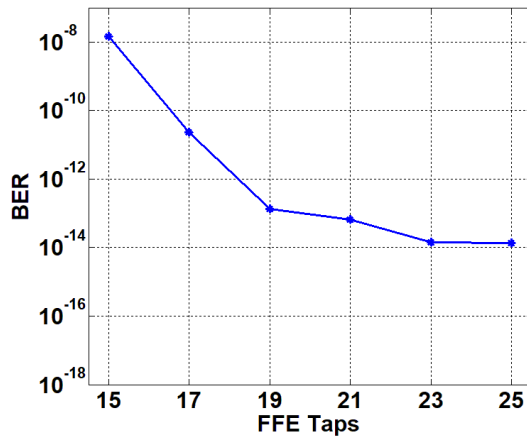
(b)
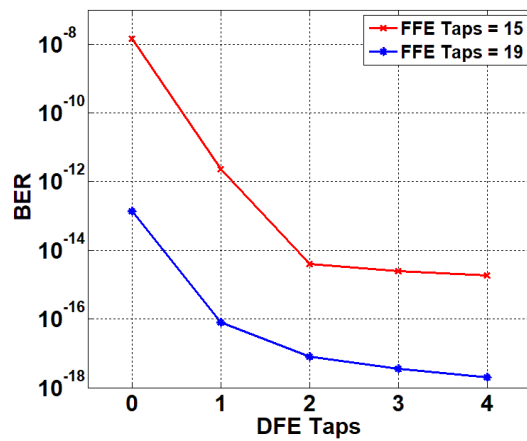
(c)

Figure 2.8. (a) A Channel with 31dB loss at 16GHz is utilized to show the impact of (b) the number of digital FFE taps on BER and (c) the improvement achieved with a digital DFE.

The DFE, however, is difficult to implement due to the challenging feedback timing path. In each cycle of operation, the decision at the output of the slicer has to pass to the output of the delay element, it has to then get scaled in the multiplier by the DFE coefficient, the scaled value has to pass through multiple summers where it is subtracted from the newly arrived symbol and the scaled decision values of other previous decisions, the resulting equalized symbol has to be

sliced to generate the new decision for the next cycle of operation. All of the above operations need to be completed in 1 symbol or 1 unit interval (UI) of time. The conceptual full rate implementation of Fig. 2.7 has one decision element, all the summers and a multiplier in the critical feedback timing path. This is often a very difficult timing path to meet. The critical feedback timing path is also significantly longer than the iteration bound since the combinational logic delay is very unevenly distributed between the delay elements. While the parallel implementation shown in Fig. 2.9 brings the critical path delay closer to the iteration bound, additional techniques are necessary to reduce the critical path delay for high data wireline receivers. Two commonly employed techniques that can significantly reduce the critical path delay are loop-unrolling and look-ahead multiplexing.

A. Loop-Unrolling

The idea of loop-unrolling [17] is to precompute all possible equalized values before a decision is actually fed back. The precomputed possible equalized values are then sliced to obtain all the possible decisions for the input symbol. These decisions are fed to a multiplexer which selects the correct decision by making use of the past decisions that are fed back. Hence, the decision is fed back only to the final multiplexer forming a multiplexer loop. This final multiplexer is now in the 1UI critical path and the summer and the slicer have been removed from this critical timing path. A general N-tap PAM-2 loop-unrolled architecture is shown in Fig. 2.10. The summers and slicers can be thought of as a precomputation section that can be pipelined and hence offers relaxed timing paths to design. The cost of reducing the critical path delay is an increase in circuit complexity. In a PAM-2 modulation system, with N taps of DFE, the number of summers and slicers required for loop unrolling is $\sum_{i=1}^{N} 2^i$ and 2^N respectively.

P-way Parallel 2-tap PAM-2 DFE Timing Paths
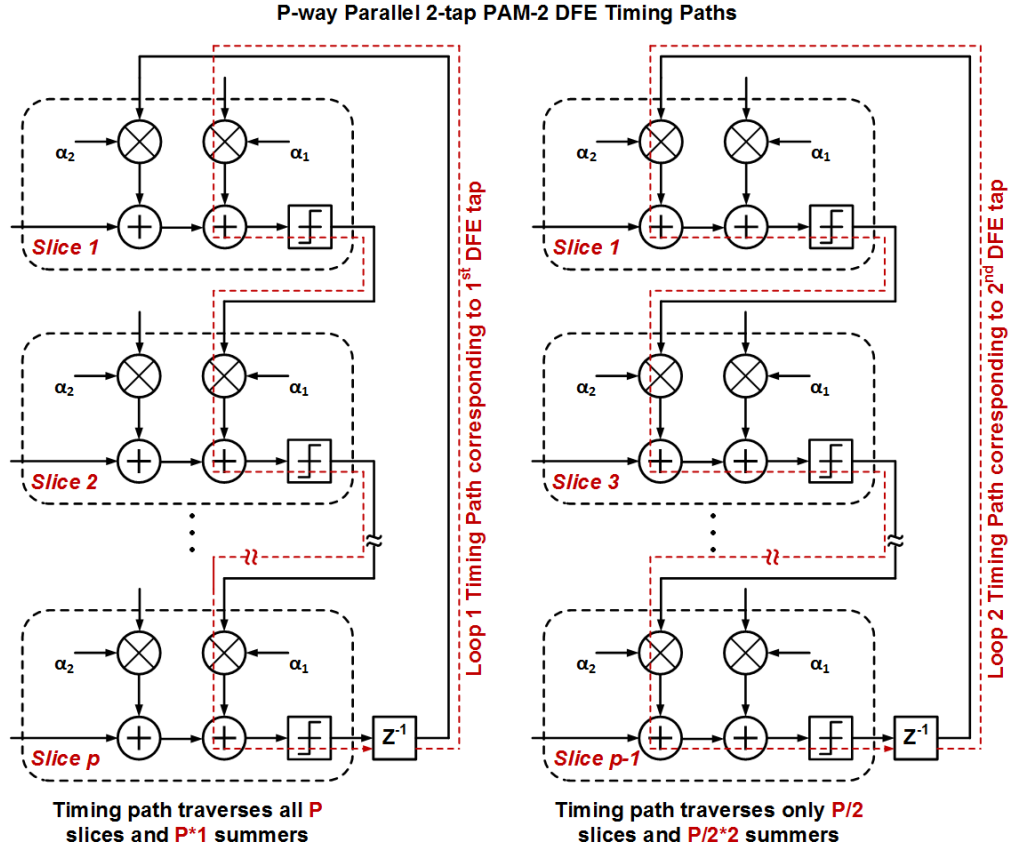
Figure 2.9. A P-way parallel implementation of a 2-tap DFE.

B. Look-Ahead Multiplexing

Since the final decision selection multiplexer is now in the critical feedback timing path, techniques are necessary to reduce delay in this multiplexer loop. Pipelining and parallel implementations cannot be used to speed up a multiplexer loop. The authors in [17] introduce a technique known as look-ahead multiplexing to speed up multiplexer loops in high speed DFE implementations. The technique is further illustrated in [18]. The 2:1 look-ahead multiplexer loop can be described using the following equations:

$$Y_n = A_n Y'_{n-1} + B_n Y_{n-1}. \tag{2.4}$$

17

Equation 2.4 describes a 2:1 multiplexer loop. The previous output Y_{n-1} is fed back as the select line for generating the current output, Y_n from the current inputs A_n and B_n. The previous output Y_{n-1} can be written as

$$Y_{n-1} = A_{n-1}Y'_{n-2} + B_{n-1}Y_{n-2}, \qquad (2.5)$$

Substituting (2.5) in (2.4),

$$Y_n = (A_n A'_{n-1} + B_n A_{n-1})Y'_{n-2} + (A_n B'_{n-1} + B_n B_{n-1})Y_{n-2}. \qquad (1.6)$$

From equation 2.6, we see that the dependence of Y_n on Y_{n-1} has been removed. Hence, the delay tolerated in the feedback path has been doubled. This technique can be extended to further relax the feedback timing path. Fig. 2.11 shows the look-ahead technique for a 2:1 multiplexer loop and it can be seen that the relaxation in the feedback timing path comes at the cost of additional multiplexers. The number of 2.1 multiplexers needed for a 2-tap multiplexer loop with a look-ahead factor of LF is $2^N(LF - 1) + \sum_{i=1}^{N} 2^{N-i}$.

2.3 Statistical Modeling of High-Speed Serial Receivers

The growing complexity of high speed links systems make it impractical to use time domain Monte Carlo (transient) simulations alone to predict the system performance, where the number of bits required to validate typical bit error rate (BER) requirements ($< 10^{-12}$) becomes prohibitive and hence statistical techniques become necessary. While these statistical tools are growing mature for binary links, conventional modeling approaches for ADC-based receivers and digital equalization use ADC performance metrics based on mean-square error (MSE), such as signal-to-noise and distortion ratio (SNDR) or effective number of bits (ENOB) [19], [20]. Since these metrics characterize the ADC performance for a single tone, they are unsuitable for a broadband system such as an ADC-based receivers. The existing statistical techniques for mixed-signal receivers and their extension to ADC-based receivers is presented in the next chapter.
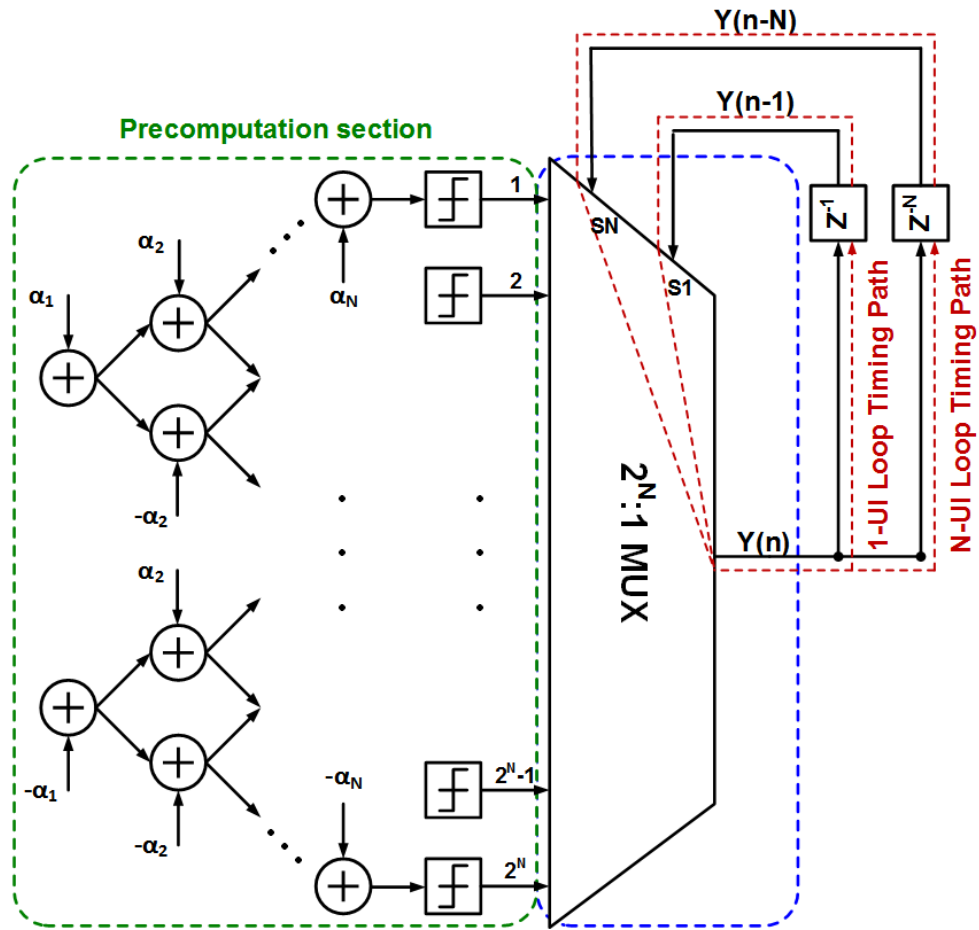
Figure 2.10. A loop-unrolled N-tap PAM-2 DFE.
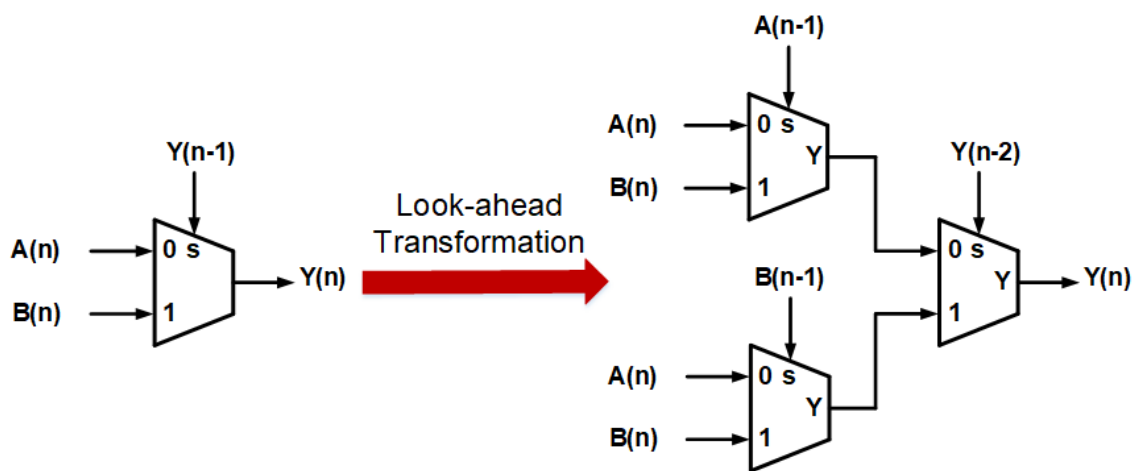
Figure 2.11. 2-way look-ahead transformation of a 2:1 multiplexer loop.

19

3. HYBRID STATISTICAL ADC-BASED RECEIVER MODELING[*]

Accurate modeling of serial link receivers with high-speed analog-to-digital converters (ADCs) is necessary to understand the various trade-offs involved and to prevent over designed power hungry systems. This chapter presents a hybrid statistical modeling framework for ADC-based serial link receivers. The framework builds upon existing statistical modeling techniques [8-10] for mixed-signal receivers and adds the support of ADC quantization noise, radix errors (integral and differential nonlinearity (INL/DNL)), and time-interleaving mismatches. A rapid, purely statistical simulation mode is utilized to model systems with small front-end nonlinearity and ADC INL/DNL, while a hybrid approach is utilized to model INL/DNL.

3.1 Statistical BER Modeling

Statistical simulation techniques that are often used to model mixed-signal serial link receivers serve as the base for inclusion of additional ADC-based receiver non-idealities. In the absence of jitter and random noise, the signal at the channel output can be written as shown in equation 2.1 and repeated here for convenience.

$$z(t) = \sum_k b_k c(t - kT), \tag{3.1}$$

where b_k is the transmitted symbol, k is the symbol index, T is the symbol period, and $c(t)$ is the channel pulse response that is extracted by convolving the channel impulse response with a single pulse. An example of a 10Gb/s NRZ pulse response is shown in Fig. 3.1. Further improvements to this pulse response with linear equalization (CTLE, FFE) is modeled by convolving the equivalent

equalizers' impulse responses with this channel pulse response. DFE is modeled by subtracting the DFE coefficients from the sampled post-cursor ISI components, with error propagation being generally ignored. After sampling, t is replaced with nT and the sampled equalized channel output $y(n)$ can be written as

$$y(n) = \sum_k b_k p(n-k),\qquad(3.2)$$

where $p(n)$ is the sampled equalized pulse response obtained by sampling the equalized pulse response $p(t)$. The first step in statistical analysis is to find the probability density function (PDF) of $y(n)$ due to the channel's inter-symbol interference (ISI). In order to calculate this, the individual channel ISI components' PDFs are convolved together and the final ISI PDF can be written as

$$f_{ISI}(v) = f_{ISI,-i} * f_{ISI,-i+1} * \dots * f_{ISI,j-1} * f_{ISI,j},\qquad(3.3)$$

where for binary NRZ modulation the individual ISI components' PDFs are written as

$$f_{ISI,m}(v) = \frac{1}{2}(\delta(v - p[m]) + \delta(v + p[m])).\qquad(3.4)$$
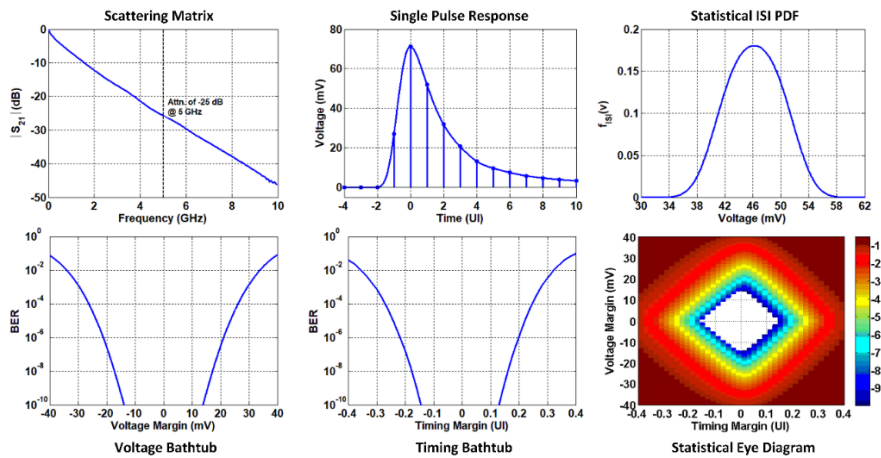
Figure 3.1. 10Gb/s NRZ modulation modeling results with a conventional mixed signal statistical modeling framework. Reprinted with permission from S. Kiran et al, IEEE ©July 4, 2018

Here $\delta(.)$ is the Dirac delta impulse function with $m \in [-i, j]$ and $m \neq 0$, and it is assumed that the channel has i pre-cursor and j post-cursor ISI taps. The statistical ISI PDF in Fig. 3.1 results from the residual ISI in an equalized pulse response, where the equalized pulse response is constructed by convolving the channel's sampled pulse response with a 5-tap FFE. Once this PDF is obtained, additional voltage noise components such as random Gaussian noise and uniform power supply noise can be included in the system by convolving the voltage noise PDFs with the ISI PDF since these components are independent. The final step is to shift the total PDF to the main cursor position at $\pm p[0]$ and perform an integration. This results in a bathtub curve which plots the BER as a function of the voltage margin.

In order to include jitter, the ISI PDF with receiver jitter can be written as

$$f_{ISI}^{\varepsilon + \varepsilon^{RX}} = \sum_n f_{\varepsilon^{RX}}(\varepsilon_n^{RX}) f_{ISI}^{\varepsilon + \varepsilon_n^{RX}}, \tag{3.5}$$

where $f_{\varepsilon^{RX}}(.)$ is the jitter PMF generated by quantizing the jitter PDF to the simulation time step and $f_{ISI}^{\varepsilon + \varepsilon_n^{RX}}$ is the ISI PDF with the sampling instant offset from the ideal position by $\varepsilon + \varepsilon_n^{RX}$. A family of ISI PDFs including the jitter effect are constructed at different sampling instants by sweeping the timing perturbation in Equation 3.5 by $\varepsilon \in [-\frac{T}{2}, \frac{T}{2}]$, and voltage and timing margin plots similar to the ones shown in Fig. 3.1 may be obtained that include receiver jitter. The techniques described so far are very similar to the ones implemented in statistical simulator engines such as Stateye [12]. It has also been assumed that the entire link is perfectly linear allowing convolution of the channel impulse response with the impulse response of the linear equalizers such as the CTLE. However, the CTLE can introduce nonlinearity that can significantly degrade BER performance particularly in PAM-4 receivers. Modeling CTLE nonlinearity in a mixed-signal link having only a CTLE as the equalizer before the slicer is relatively straight forward [21].

Consider the link system shown in Fig. 3.2 where a nonlinear CTLE has been decomposed

into a linear CTLE followed by a non-linear transfer function. The input X and the output Y of the

nonlinearity block are related by the equation

$$y = a_1 x + a_3 x^3, \tag{3.6}$$

where a_1 and a_3 are the linear gain and third non-linearity coefficient respectively. It is assumed

that the second order non-linearity is negligible. If the PDF of the signal before the non-linearity

is known, which can determined through the techniques described previously for a perfectly linear

system, the PDF at the output of the non-linear block can be simply written as

$$f_Y(y) = \frac{f_X(x)}{\frac{dy}{dx}}, \tag{3.7}$$

where $f_Y(y)$ and $f_X(x)$ are the PDFs of Y and X respectively. An assumption is also made that the

non-linear transfer function is one-to-one and monotonically increasing, which generally holds in

the case of a CTLE nonlinear transfer function. The impact of this nonlinearity is illustrated in Fig.

3.3. The simulation result of Fig. 3.3 assumes that the 1-dB gain compression point of the CTLE

transfer function is at 350mV. Mixed signal receivers commonly employ DFE for additional

equalization and hence it important to model the impact of DFE on the nonlinearity introduced by

the CTLE. Fig. 3.4 shows a mixed signal receiver with a CTLE followed by a DFE with the

summer in the DFE explicitly shown to aid the discussion of the technique employed to model the

impact of the DFE on the CTLE nonlinearity. The key point to note in this discussion is how the

PDF at the input of the summer is modified at the output of the summer due to the feedback from

the FIR filter. If the DFE cancels the kth postcursor component of the sampled equalized pulse

response $p(n)$, then the signal at the output of the DFE summer, represented by the random

variable Z, has $p(k) = 0$ with the signal before the summer, both X and Y, having $p(k) \neq 0$.
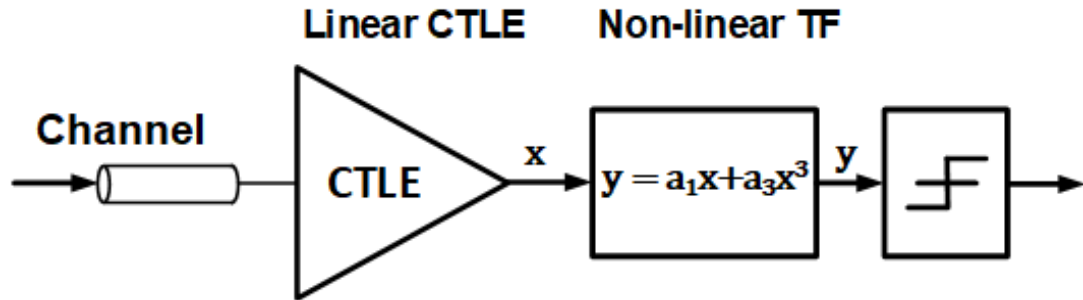
Figure 3.2. Nonlinear CTLE decomposed into a linear CTLE followed by a nonlinear transfer function.
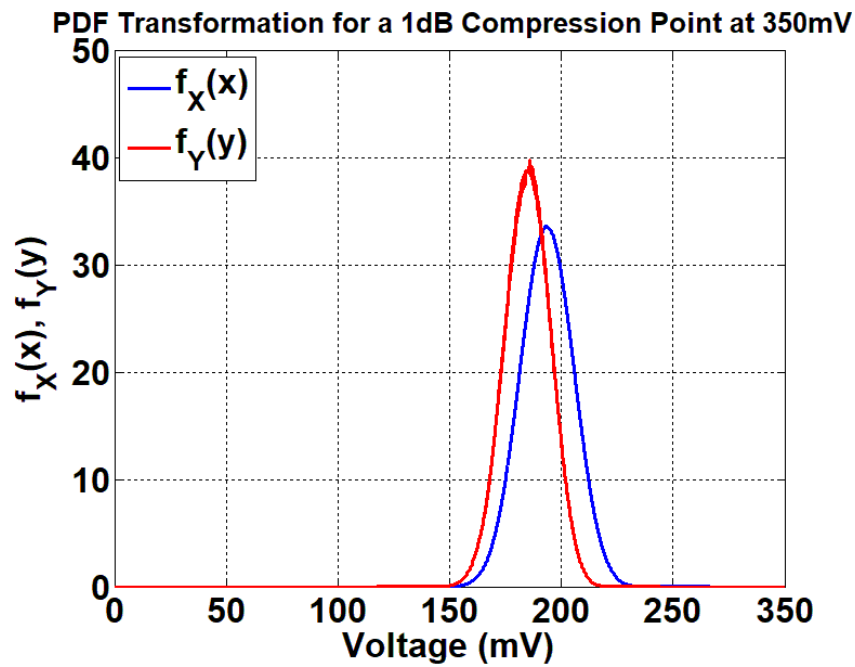
Figure 3.3. Transformation of PDF of a random variable as a result of applying monotonic one-to-one nonlinear transfer function.
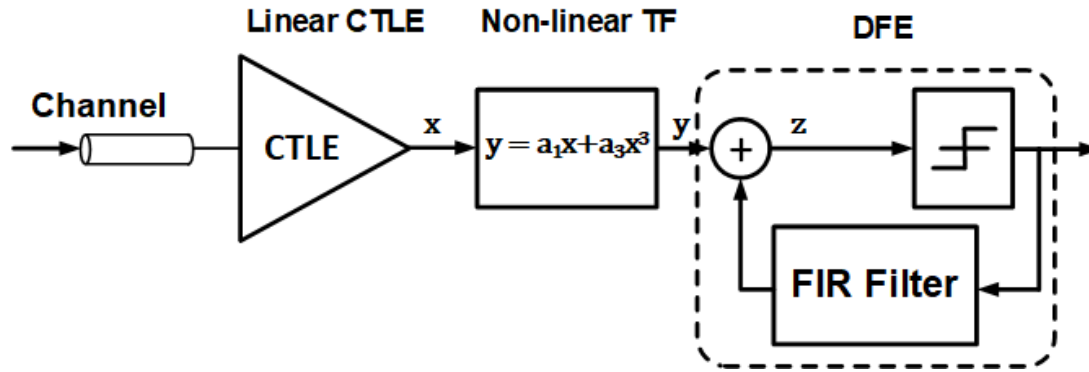
Figure 3.4. A nonlinear CTLE followed by a DFE.
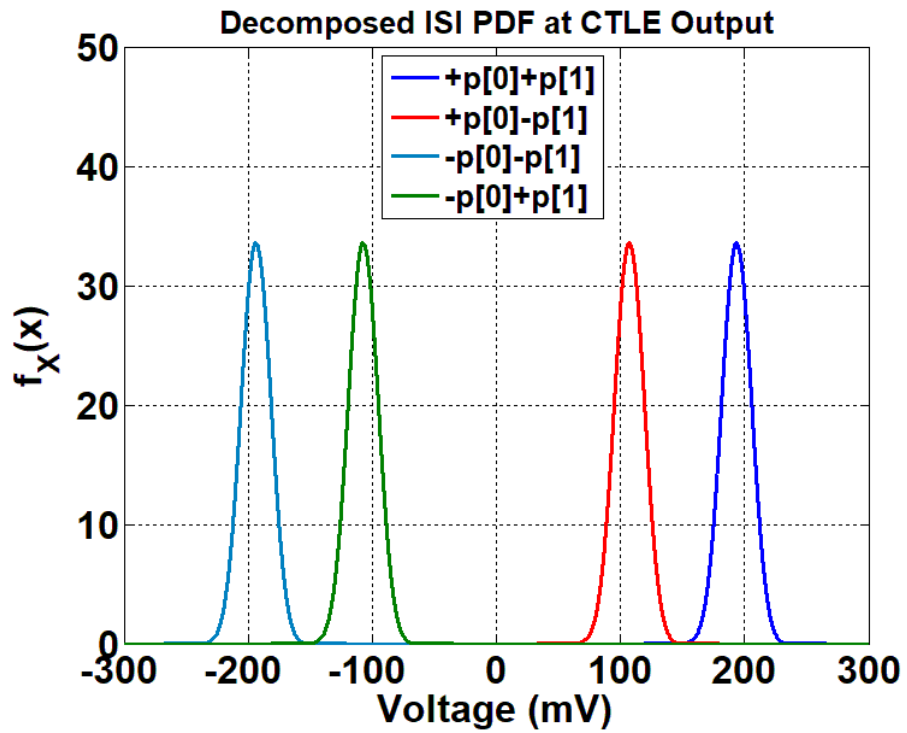
(a)
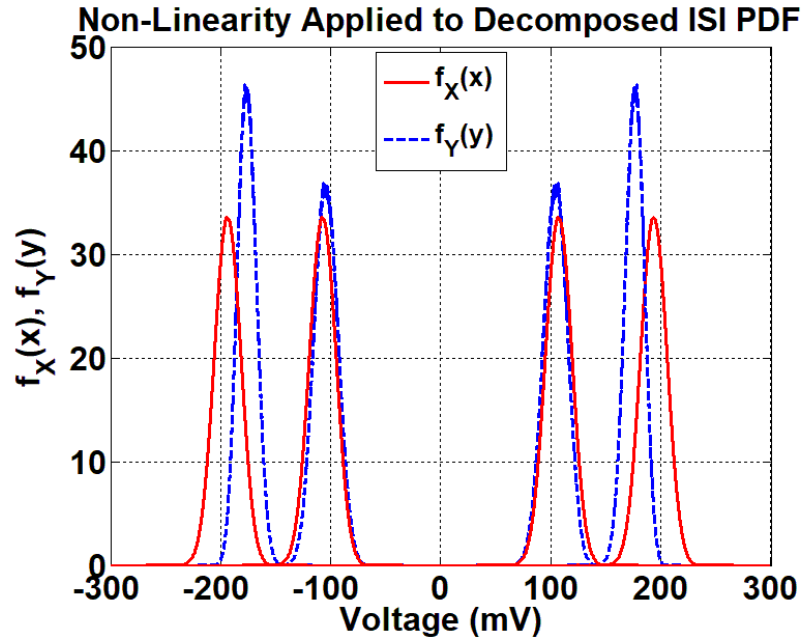
(b)
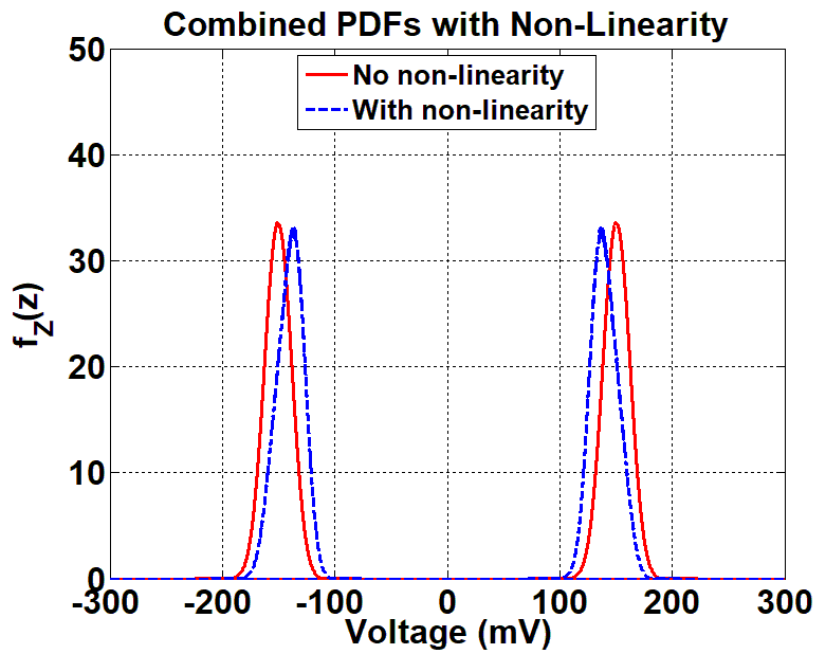
(c)

Figure 3.5. (a) Decomposed PDF at the output of the linear CTLE with the four PDFs centered at $\pm p(k) \pm p(0)$ (b) Nonlinearity applied to the 4 PDFs and the resulting PDF at the output of the nonlinear transfer function block and (c) the combined PDF obtained by setting $p(k) = 0$ at the DFE summer output.

26
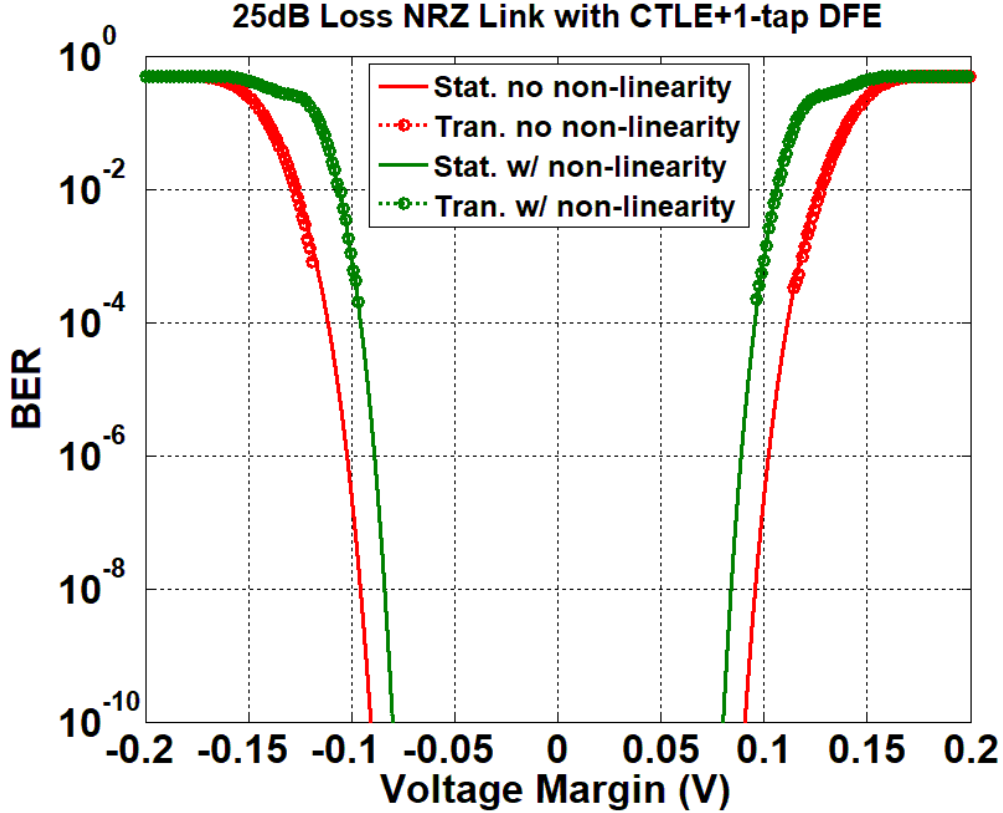
Figure 3.6. Statistical model and transient simulation results showing good matching both with and without nonlinearity.

Therefore the technique to model CTLE nonlinearity in the presence of a DFE is to decompose the ISI PDF, $f_{ISI}(v)$, into 2 PDFs where k^{th} postcursor is $\pm p(k)$, applying the PDF transformation technique of Equation 3.6 to both the PDFs and then merge the PDFs together by setting $p(k) = 0$. With reference to Equation 3.3 and Equation 3.4, the decomposition is achieved by setting $m \neq 0$ and $m \neq k$. The resulting ISI PDF is then shifted to $\pm p(k) \pm p(0)$. Note that this results in 4 PDFs instead of 2 PDFs that result from Equation 3.3 and Equation 3.4. All of the above discussion applies to a 1-tap DFE for a link employing PAM-2 modulation but can be easily extended to multiple tap DFE and PAM-4 modulation. The nonlinearity modeling technique is illustrated using Fig. 3.5. The simulation results assume a transmitter swing of $0.6V_{ppd}$ with no Tx

27

equalization. The receiver comprises of a CTLE and a 1-tap DFE with the nonlinear transfer function yielding a 1-dB compression point of 250mV. The statistical model is compared with transient simulation in Fig. 3.6 and excellent matching is obtained verifying the technique. To the mixed signal simulation framework various ADC specific impairments are added. These are detailed in the sections that follow.

3.2 ADC Quantization Noise

Quantization error is formally deterministic for a given input signal, additional justification is necessary to include an equivalent quantization noise PDF similar to independent random noise. It was shown in [22] that under certain conditions that are generally met with ADC resolutions used in high-speed link applications, quantization error can be treated as an uncorrelated random variable with a white spectrum that can be treated as an additive noise term known as quantization noise. The uniform PDF for quantization noise is obtained through an area summation process as shown in Fig. 3.7. The probability of having a particular quantization error q is probability of the input signal x falling at $x_i + q$ where x_i is quantized level in any of the quantization intervals. This is equivalent to cutting the input signal's PDF into strips of width Δ, the quantization interval, and summing them up. From another perspective, the quantization process works to concentrate the input signal PDF within each quantization interval into a single quantized level at the center of the quantization interval. This is mathematically equivalent to convolving the input signal PDF with a uniform PDF with the width of the uniform PDF equal to the quantization interval and then sampling the resulting PDF. Therefore, the quantizer's output PDF is very similar to the PDF of the sum of the input signal and an independent uniformly distributed noise quantity. This approach has been called the pseudo quantization noise (PQN) model. An important issue in ADC-based

high speed link receivers is that the quantized input signal is generally equalized with a digital

FFE, resulting in quantization noise amplification.
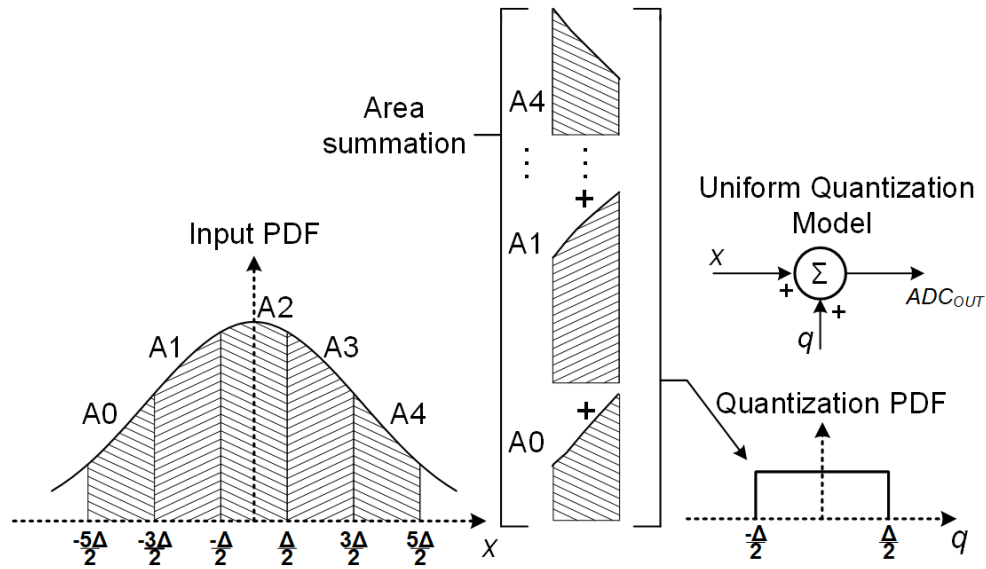
Figure 3.7. Input PDF and equivalent quantization noise PDF construction. Reprinted with permission from S. Kiran et al, IEEE ©July 4, 2018.
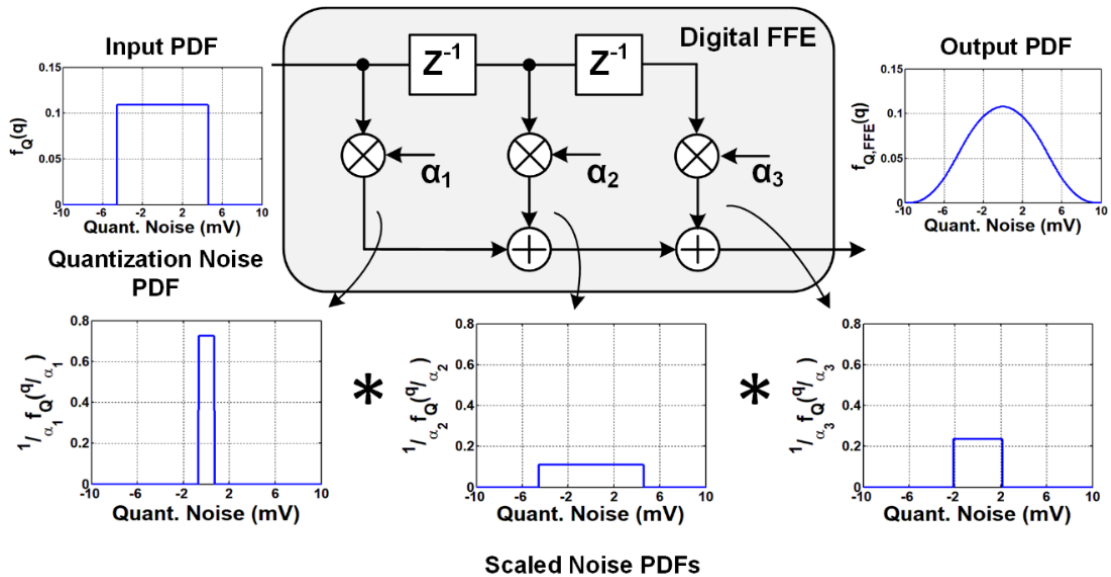
Figure 3.8. Modeling of quantization noise amplification through the digital FFE.

In order to include this effect, the quantization PDF at the ADC output, f_Q, is scaled by different FFE coefficients and the resulting PDFs are convolved together, as shown in Fig. 3.8, to arrive at the final quantization noise PDF $f_{Q,ffe}$ which is written for a K-tap FFE as

$$f_{Q,ffe} = \frac{1}{\alpha_1} f_Q\left(\frac{q}{\alpha_1}\right) * \frac{1}{\alpha_2} f_Q\left(\frac{q}{\alpha_2}\right) * \dots * \frac{1}{\alpha_K} f_Q\left(\frac{q}{\alpha_K}\right). \tag{3.8}$$

The ADC quantization noise modelling approach is verified by comparing transient simulations and statistical modeling results of 10Gb/s NRZ operation over the channel with 25dB loss at the Nyquist frequency from Fig. 3.1. These simulations utilize a 0.6V$_{ppd}$ transmit swing without TX equalization and the receiver employs a 5-tap digital FFE with a coefficient resolution of 8 bits. Utilizing 14-bit DSP resolution to have negligible round-off errors, the simulation results of Fig. 3.9(a) and (b) show that good matching is achieved as the ADC resolution is varied from 3 to 6 bits for cases with an ADC input random noise of 1mV$_{rms}$ and 2mV$_{rms}$. For the channel under test, at least 5 bits of ADC resolution is necessary to obtain an open eye with a BER less than 10^{-10}. While the BER performance is poor, the model still displays good matching with a 3-bit resolution ADC that is generally the lowest resolution used in ADC-based wireline receivers.

DSP round-off errors are also included in the model using a similar approach. This round-off generally occurs at the multiplier outputs to reduce the resolution required in the subsequent adders and pipelining sequential elements. The probability of a particular round-off error is the probability of the corresponding ADC output occurring, which is obtained by computing the ISI PDF at the ADC output. This is essentially the same process as the area summation process for computing the ADC quantization error PDF. The resultant round-off error PMF at the different multiplier outputs are assumed independent and are convolved with the ISI PDF, similar to how the ADC quantization error PDF is included in the statistical model. Fig. 3.9(c) shows the

30

simulation results when the FFE multiplier resolution is limited to a relatively low 6 bit value, which is the same as the ADC resolution. Even with this low DSP resolution, good matching is obtained between the statistical model and the transient simulations. Assuming the 2mV_{rms} noise case used in Fig. 3.9(b), the BER=10^{-10} voltage margin reduces from 31.3 mV to 9.3 mV when the DSP resolution is reduced from 14 bits to 6 bits. Note that, while these purely-statistical techniques works well for an ADC with low INL/DNL and allows for rapid simulations, this approach breaks down with appreciable non-linearity and the technique described in the next sub-section is required.

3.3 Radix Errors

The most commonly used quantizers are the uniform radix-2 type that map the input to one of 2^R equally spaced levels, where R is the ADC resolution.

(a)

31
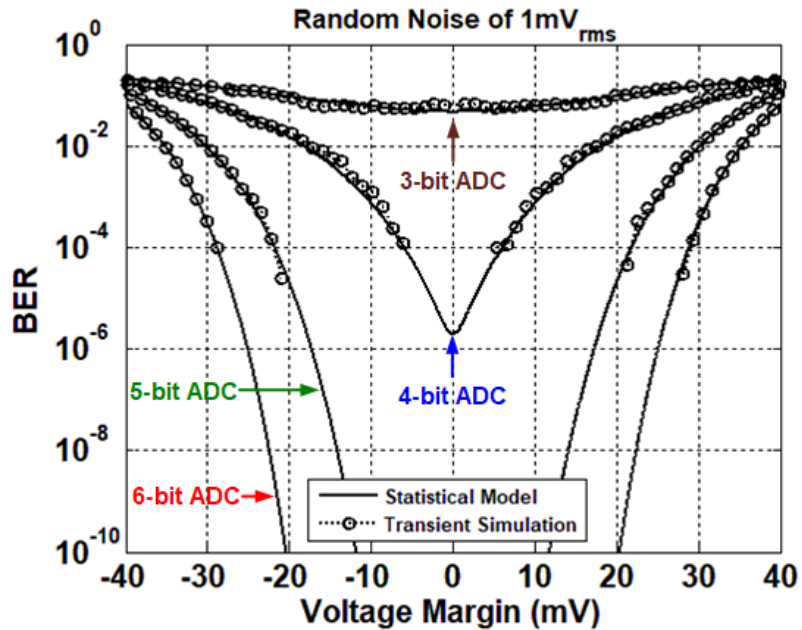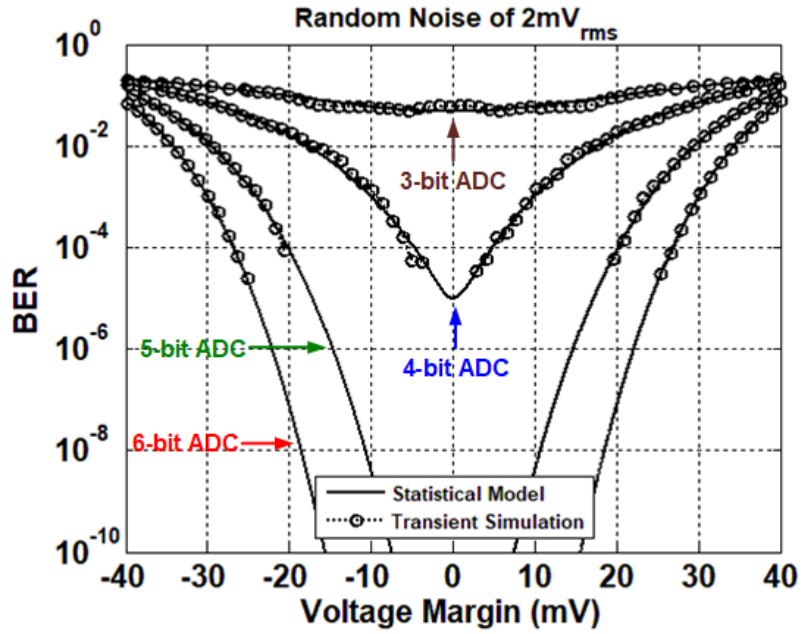
(b)
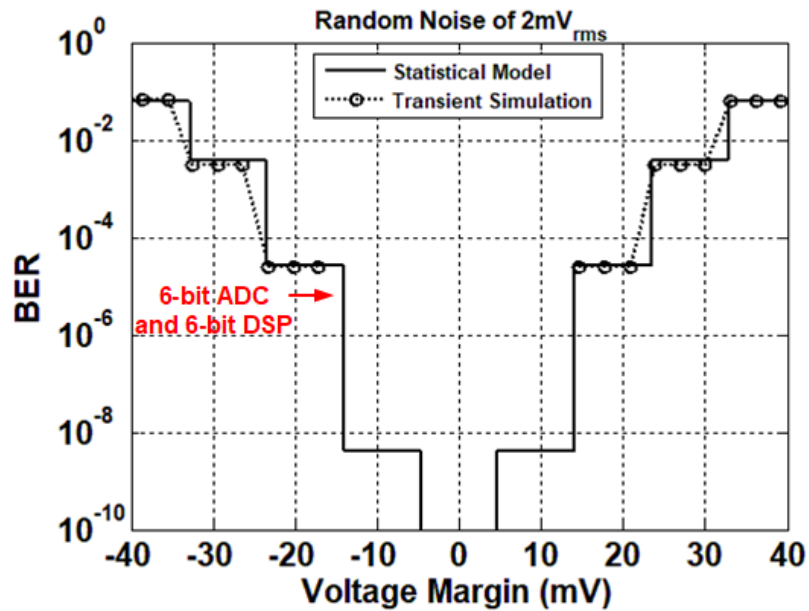
(c)

Figure 3.9. Comparison of 10Gb/s NRZ voltage bathtub curves for the 25dB loss channel of Fig. 3.1 produced with the quantization noise modeling technique and transient simulations. The ADC resolution is varied from 3-6 bits with an ADC input random noise of (a) $1mV_{rms}$ and (b) $2mV_{rms}$. (c) The DSP resolution is reduced to 6 bits for the $2mV_{rms}$ case to show the impact of DSP round-off error. Reprinted with permission from S. Kiran et al, IEEE ©July 4, 2018

32

However, quantizers exhibit non-idealities due to process variations and circuit mismatches, resulting in modified quantizer thresholds. Due to the modified thresholds, quantization is non-uniform and this causes the quantization noise to be no longer uncorrelated with the input [16]. This introduces 2 difficulties in modeling quantization noise as described in section 3.2. First, in order to find the quantization noise PDF at the output of the digital equalizer, quantization noise PDFs that are scaled by the FFE coefficients cannot be convolved together as shown in Fig. 3.8. This necessitates a transient simulation to find the quantization PDF at the output of the digital equalizer. The second difficulty is that the quantization noise PDF at the output of the digital equalizer extracted through a transient simulation cannot be convolved the ISI PDF. This second challenge to including these radix errors in the modeling framework is addressed by generating level-dependent quantization noise PDFs. Recall that the ISI PDFs obtained from Equation 3.3 are centered at $+p[0]$ and $-p[0]$. Consider first a scenario where at the output of the equalizer there is no residual ISI and the two ISI PDFs are simply delta functions at $+p[0]$ and $-p[0]$. Two quantization noise PDFs, denoted as Q^+_{pdf} and Q^-_{pdf}, are extracted through transient simulations when the current symbol is 1 and -1 respectively. This requires tracking the current symbol from the ADC input to the digital equalizer output. Hence, these quantization noise PDFs are said to be extracted with 1 symbol tracking in this case. For every quantization noise value in Q^+_{pdf} and Q^-_{pdf}, the signal value at the equalizer output is a deterministic value of $+p[0]$ and $-p[0]$, respectively. The resultant signal with the quantization noise added is simply the sum of $+p[0]$ and all the quantization noise values in Q^+_{pdf} and the sum of $-p[0]$ and all the quantization noise values in Q^-_{pdf}. The resultant signal PDF is obtained by shifting Q^+_{pdf} to be centered on $+p[0]$ and shifting Q^-_{pdf} to be centered on $-p[0]$. This is done through a convolution operation,

33

where $+p[0]$ is convolved with Q_{pdf}^+ and $-p[0]$ is convolved with Q_{pdf}^-. Note, that it is not necessary for the residual ISI to be zero and this technique can be employed as long as the residual ISI at the output of the equalizer is small.

From the discussion so far, in the presence of non-uniform quantization the signal with ISI and the quantization noise are made conditionally independent with the condition being the current symbol having a specific value of +1 or -1. To handle scenarios where there is significant residual ISI at the equalizer output, this technique is further extended with the condition being specific symbol patterns. For example, if the significant residual ISI term is the first postcursor ISI term, then the conditions are the symbol patterns "-1-1", "-1+1","+1-1", and "+1+1" for the previous and the current symbol, respectively. In general, referring to Equation 3.3 and Equation 3.4, if a significant residual ISI term at position i is present at the equalizer output, then the ISI PDF is computed by making $m \neq 0$ and $m \neq i$. The resulting ISI voltage PDFs are then shifted to $\pm p\,[0] \pm p[i]$, yielding 4 ISI PDFs in place of 2 ISI PDFs that are obtained without this additional decomposition. Quantization noise PDFs are then extracted through transient simulations when the current received symbol is ± 1 and the received symbol giving rise to the ith ISI component is ± 1. This technique is illustrated in Fig. 3.10, where 2 of the 4 decomposed ISI PDFs at $p[0] \pm p[i]$ and their corresponding quantization noise PDFs are shown. Note that if a large number of significant residual ISI terms are present, then running multiple transient simulations can increase the total simulation time. Thus, the amount of symbols that are tracked and the utilized quantization noise PDFs can be varied to trade-off accuracy versus simulation time. This radix error modeling technique is verified for the case of a 6-bit ADC with a compressive INL profile with maximum INL of 2 LSB as shown in Fig 3.11(a). The INL profile is said to be compressive because for certain inputs the ADC with non-linearity has a smaller slope in the output code than an ideal ADC

34

without non-linearity. The analog front-end non-linearity can also be merged with the ADC non-linearity to get an effective ADC transfer characteristic. 20Gb/s PAM-4 modulation with a transmit swing of 900mV$_{ppd}$ over the channel with 25dB loss at the Nyquist frequency from Fig. 3 is utilized to more clearly illustrate the impact of any receiver non-linearity. A longer 12-tap digital FFE and a 1-tap DFE is also employed due to the PAM-4 modulation sensitivity to residual ISI.
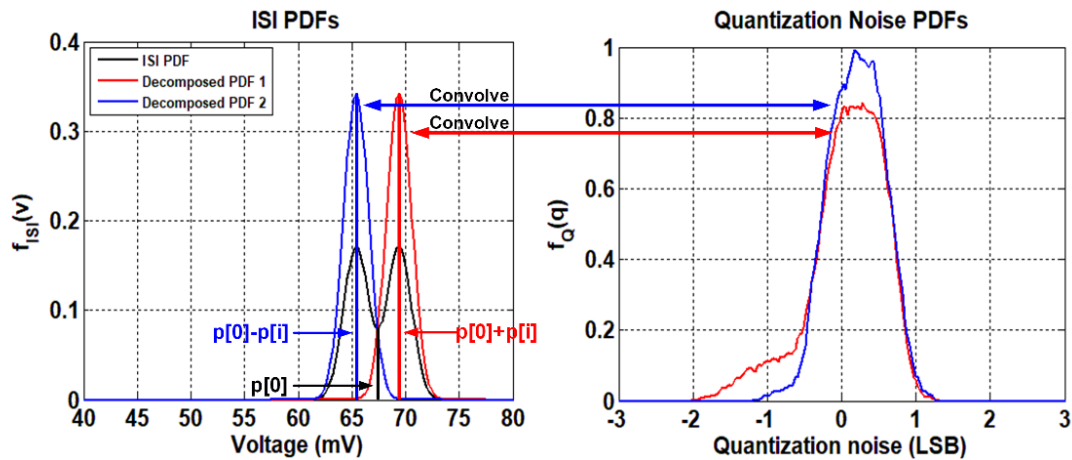
Figure 3.10. Decomposing of the ISI PDF and convolving with the corresponding quantization noise PDF. Reprinted with permission from S. Kiran et al, IEEE ©July 4, 2018

Fig. 3.11(b) shows the PAM-4 voltage bathtub curves for an ADC without non-linearity, which allows for rapid simulation via direct convolution of the FFE-shaped quantization noise PDF with the ISI PDF. Fig. 3.11(c) shows the PAM-4 voltage bathtub curves for the ADC with 2 LSB peak INL. Utilizing the 12-tap FFE and 1-tap DFE allows for a small amount of residual ISI and the use of only one symbol tracking in producing the level-dependent quantization noise PDFs. Excellent matching is obtained between the hybrid statistical model and transient results. In the simulation of Fig 3.11(d), one significant ISI term is introduced by a having a suboptimal DFE

coefficient equal to 70% of its ideal value. With this residual ISI, tracking of two symbols is required to achieve good matching of the hybrid statistical model with transient simulations.
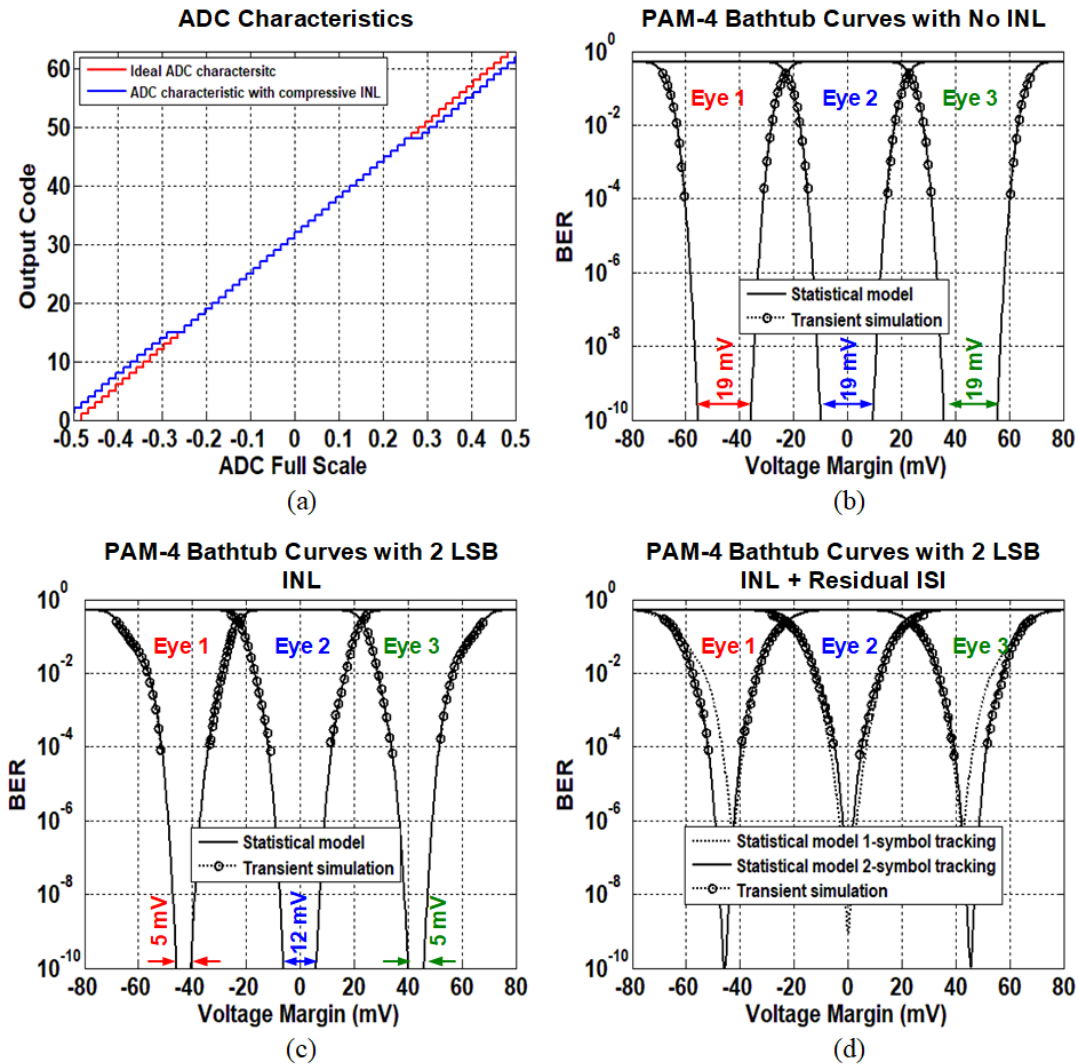
Figure 3.11. (a) Ideal and compressive 6-bit ADC characteristics. (b) 20Gb/s PAM-4 voltage bathtub curves for an ideal ADC, (c) an ADC with 2-LSB INL and small post-equalization residual ISI, and (d) an ADC with 2-LSB INL and a significant first postcursor ISI component after equalization. Reprinted with permission from S. Kiran et al, IEEE ©July 4, 2018

It is interesting to note that with one significant residual ISI term, the middle eye is worse than the outer two eyes. This is because the middle eye has the same worst case patterns in terms of ISI and

quantization noise and their impacts combine with the same polarity. While for the outer eyes, the worst case patterns for ISI and quantization noise are different. The outer eyes' worst case ISI patterns and the corresponding quantization error terms combine with opposite polarities and reduce the impact of each other. Similarly, the worst case patterns for quantization error and the corresponding residual ISI errors again combine with opposite polarities. It should be noted that this is not a general result, but represents one possibility of how quantization noise and ISI can interact with each other. Overall, different transfer functions and FFE taps values can produce different results.

3.4 Time-Interleaving Mismatch Errors

Time-interleaving is utilized in order to enable the use of ADC-based receivers for multi-Gb/s operation. With time-interleaving, M parallel converters, each at a sampling rate of f_s/M, give an aggregate sampling rate of f_s. However, new types of errors are generated due to mismatches existing between different parallel channels. These mismatches can be divided into four types: gain, bandwidth, sampling time skew, and offset errors.

Each time-interleaved channel can experience a different static gain due to mismatches in the parallel track-and-holds (T/Hs), reference circuitry, and other gain stages in the signal path. These device mismatches, along with layout asymmetries, also result in the different parallel ADCs displaying different effective bandwidths. While ideally the multiple clock phases used to sample the input signal are uniformly spaced, device mismatches and layout asymmetries in the clock generation and distribution to the parallel T/H blocks cause skew errors that shift the sampling instance for each parallel ADC. Finally, static offsets in the T/Hs, reference circuitry and comparators shift each parallel ADC's transfer characteristic.

The effect of time-interleaving errors on ADC performance has been previously studied in terms of degradation in SNDR [23]. However, since the most important metric in ADC-based receivers is the BER, techniques to analyze the effect of different ADC mismatches on BER are necessary. The procedure shown in Fig. 3.12 is utilized to include the time-interleaving errors in the statistical model. For an M-channel time-interleaved system, M different pulse responses are extracted utilizing the transmission channel, receiver front-end, and parallel ADC channel responses. This results in M different continuous pulse responses that capture the parallel ADC channels' specific gain and bandwidth. These pulse responses are then sampled, taking into account the timing skew errors, to yield M different sampled pulse responses. The new pulse responses are finally equalized through the digital FFE/DFE and the M equalized pulse responses are used to generate the ISI PDFs required for obtaining BER curves. As an example, consider the case with no channel mismatches present and digital FFE utilized, the equalized pulse response, $g[n]$, is represented using the convolution equation as

$$g[n] = \sum_{k}^{K-1} \alpha[k]h[n - k], \qquad (3.9)$$

where $h[n]$ is the ideal channel pulse response with N ISI taps and $\alpha[k]$ is a digital FFE with K coefficients such that $N \geq K$. Note that Equation 3.9 can be rewritten using a Toeplitz matrix representation [24]. Now, consider an M-way time-interleaved ADC with the previously described mismatches present. Each new input to the FFE comes from the next time-interleaved channel in relation to the previous input. In this scenario, M different pulse responses are obtained depending on which of the M channels provides the sample for the first FFE tap. The pulse responses are obtained by modifying the Toeplitz matrix, as shown in Equation 3.10.

$$
\begin{bmatrix} g_l[0] \\ g_l[1] \\ g_l[2] \\ \vdots \\ g_l[L] \end{bmatrix} = \begin{bmatrix} h_l[0] & h_{((l+1))_M}[1] & h_{((l+2))_M}[2] & \cdots & h_{((l+N-1))_M}[N-1] & \cdots & 0 \\ 0 & h_l[0] & h_{((l+1))_M}[1] & \cdots & h_{((l+N-2))_M}[N-2] & \cdots & 0 \\ 0 & 0 & h_l[0] & \cdots & h_{((l+N-3))_M}[N-3] & \cdots & 0 \\ \vdots & \vdots & \vdots & \ddots & \vdots & \ddots & \vdots \\ 0 & 0 & 0 & \cdots & h_{((l+N-K))_M}[N-K] & \cdots & h_{((l+N-1))_M}[N-1] \end{bmatrix}^T \begin{bmatrix} \alpha[0] \\ \alpha[1] \\ \alpha[2] \\ \vdots \\ \alpha[K-1] \end{bmatrix} \qquad (3.10)
$$
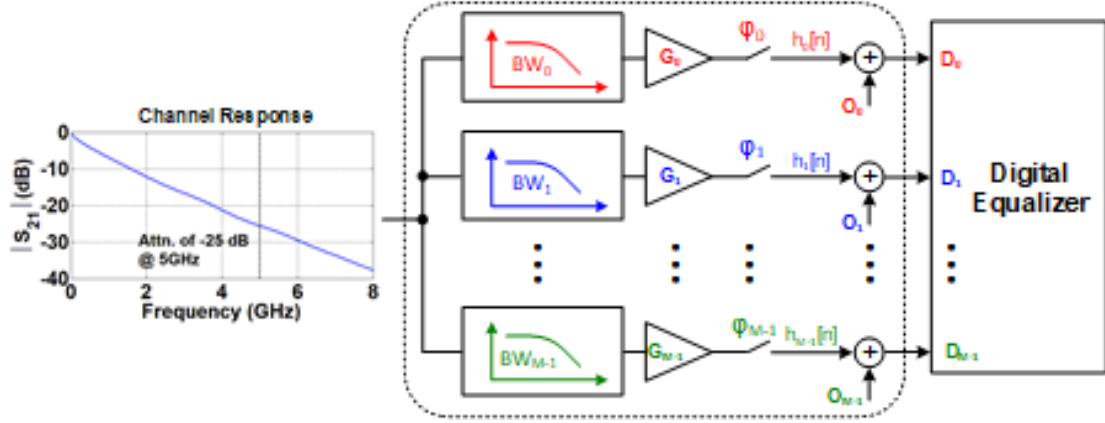
Figure 3.12. Modeling of time-interleaving ADC errors. Reprinted with permission from S. Kiran et al, IEEE ©July 4, 2018

Here l ranges from 0 to $M-1$, L is equal to $N+K-1$, and the $((.))_M$ operator represents the modulo M operation. Fig. 3.13 shows the procedure of combining the residual ISI components from the lone pulse responses of the different time-interleaved channels. Let the M pulse responses in the left half of Fig. 3.13 each have i non-zero precursor values and j non-zero postcursor values. When the main cursor of the lth pulse response, $g_l[i]$, is at the FFE output, the residual precursor ISI components contributed by all the M channel responses are $g_{((l+1))_M}[i-1]$, $g_{((l+2))_M}[i-2]$, and so on up to $g_{((l+i))_M}[0]$. The residual postcursor ISI components contributed by all the M channel responses are $g_{((l-1))_M}[i+1]$, $g_{((l-2))_M}[i+2]$, and so on up to $g_{((l-j))_M}[i+j]$. This is illustrated in the collection of ISI contributions from different channels at one particular time instant of interest shown in the right half of Fig. 3.13. The PDFs of these ISI components are

convolved together as shown in Equation 3.11. This results in M different ISI PDFs, f_{ISI_l} with $l \in [0, M-1]$, and the PDF with all the mismatches accounted for is the average of all these M PDFs.

$$f_{ISI_l}(v) = f_{ISI,g_{((l+i))_M}}[0] * f_{ISI,g_{((l+i-1))_M}}[1] \dots * \delta(v - g_l[i]) \dots$$

$$* f_{ISI,g_{((l-j+1))_M}}[i+j-1] * f_{ISI,g_{((l-j))_M}}[i+j]$$

(3.11)

So far, the effect of gain, bandwidth, and timing skew mismatch errors have been considered. Offset error results in an M-periodic signal at the ADC output that is filtered by the high-pass nature of the FFE. Assuming the FFE has u precursor taps and w postcursor taps, such that $K = u + w + 1$, the filtered offset values at the output of the FFE are

$$O_{out}[l] = \sum_{k=-u}^{w} \alpha[k+u]O[((l+k))_M],$$

(3.12)

where $O(l)$ are the offsets at the ADC time-interleaved channel outputs. These offset values effectively shift the ISI PDFs. The M shifted ISI PDFs are then averaged to yield a final PDF, $f_{ISI_{ti}}$, that includes all the time-interleaved errors as shown in Equation 3.13.

$$f_{ISI_{ti}} = \frac{1}{M}\sum_{l=0}^{M-1} f_{ISI_l}(v) * \delta(v - O_{out}[l]),$$

(3.13)

In order to verify the time-interleaving error statistical modeling techniques, transient simulations and statistical modeling results are compared for 10Gb/s NRZ operation over the channel with 25dB loss at the Nyquist frequency from Fig. 3.1. A 6 bit, 4-way time-interleaved ADC architecture is assumed, with the results shown in Fig. 3.14. These simulations utilize a 0.6V$_{ppd}$ transmit swing with no transmit equalization. The receiver employs a 5-tap digital FFE and 2mV$_{rms}$ random noise at the ADC input is assumed. Overall, the statistical model matches well with transient simulations for time-interleaved gain, bandwidth, timing skew, and offset errors.
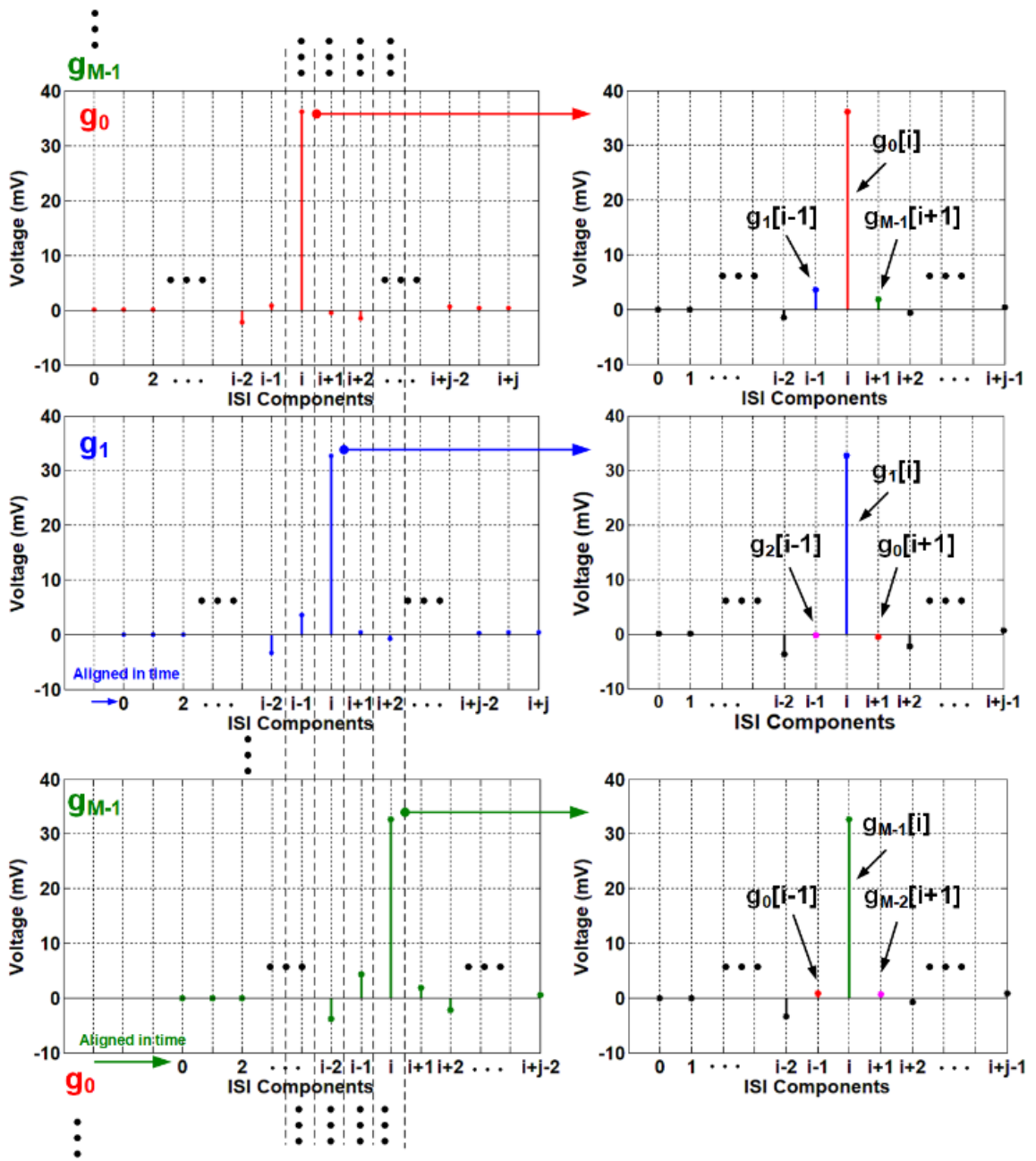
Figure 3.13. Pulse response through the digital equalizer for the M time-interleaved channels (left) and ISI contributions from different channels at one particular time instant (right). Reprinted with permission from S. Kiran et al, IEEE ©July 4, 2018

41
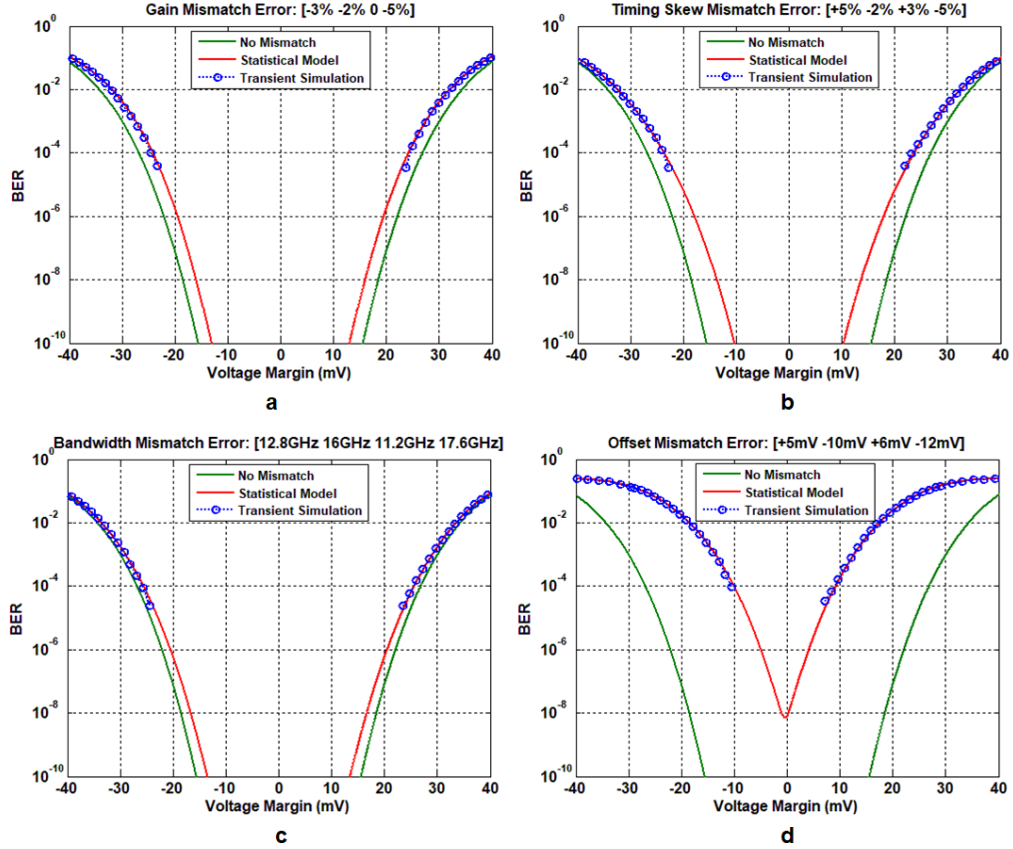
Figure 3.14. Comparison of 10Gb/s NRZ voltage bathtub curves for the 25dB loss channel of Fig. 2 produced with the time-interleaving errors modeling techniques and transient simulations. A 4-way time-interleaved ADC with 6-bit and $1mV_{rms}$ input noise is utilized with subsequent 5-tap digital FFE. Simulation results for (a) gain, (b) timing skew, (c) bandwidth, and (d) offset errors. Reprinted with permission from S. Kiran et al, IEEE ©July 4. 2018

3.5 Conclusion

Chapter 3 presented a hybrid statistical modeling framework for ADC-based serial links. It builds on existing mixed-signal statistical models that capture ISI and jitter in a perfectly linear link. A new method to model CTLE nonlinearity in the presence of DFE based on a PDF decomposition technique was introduced. Quantization noise was noise was then included by modeling it as a uniformly distributed independent noise source. The second contribution of this chapter was the modeling of non-uniform quantization in the presence of residual ISI utilizing the

PDF decomposition technique previously introduced. The final contribution of this chapter is the modeling of time-interleaving mismatches by treating the TI-ADC as LPTV system. The entire hybrid statistical model has been verified by comparing its results with a transient bit-by-bit simulation model and excellent matching has been obtained.

4. A 52GB/S ADC-BASED PAM-4 RECEIVER WITH REFERENCE SCALED 2BIT/STAGE SAR ADC AND PARTIALLY-UNROLLED DFE[†]

This chapter presents an ADC-based PAM-4 receiver employing a 32-way time-interleaved, 2-bit/stage, 6-bit SAR ADC with a single capacitive reference DAC and a DSP with a 12-tap FFE and a 2-tap DFE. A new DFE architecture that reduces the complexity of a PAM-4 DFE to that of an NRZ DFE while simultaneously nearly doubling the maximum achievable data rate is presented. Partial analog equalization is provided in the form of a programmable two stage CTLE and a 3-tap FFE that is embedded in the ADC using a non-binary FFE DAC to improve the FFE coefficient coverage space. Utilizing the partial analog equalization, a digital baud-rate CDR's Mueller-Muller phase detector is placed directly at the ADC output to avoid excessive loop delay. Architecture and circuit details along with measurement results is presented next.

4.1 PAM-4 DFE Challenges

The decision feedback equalizer (DFE) is a powerful nonlinear equalization technique that can offer a significant advantage over a linear equalizer, such as an FFE, since it can cancel post-cursor ISI without noise and crosstalk amplification. The impact of including 2-taps of DFE is shown in Fig. 4.1 by plotting the receiver voltage margin at a BER of 10^{-6} for a given number of FFE taps under 2 different noise assumptions. The simulation assumes a data rate of 52Gb/s with the channel having a loss of 30dB at the Nyquist frequency of 13 GHz. No Tx equalization is included with the transmitter having a peak to peak differential swing of $0.8V_{ppd}$. The receiver is

assumed to employ a 2-stage CTLE and a 3-tap FFE embedded in the ADC with the ADC having a resolution of 6 bits. A random noise of $3mV_{rms}$ is added to the signal at the input of the ADC. This represents the total output noise from the analog front-end and the input referred noise of the comparator itself. Fig. 4.1 shows that FFE only receiver needs about 18 taps to achieve a voltage margin greater than 10mV with very small improvements on further increasing the number of FFE taps. At this point, the voltage margin is mainly limited by random noise and timing uncertainty. However, by including 2 DFE taps, a BER of 10^{-6} with a voltage margin of 19mV can be achieved with 12 FFE taps. In order to achieve a comparable voltage margin with the FFE only receiver, 16 FFE taps and a very low random noise of $1mV_{rms}$ is necessary. Designing an analog front-end with $1mV_{rms}$ random noise at the ADC input for a 52Gb/s system would be extremely power hungry.
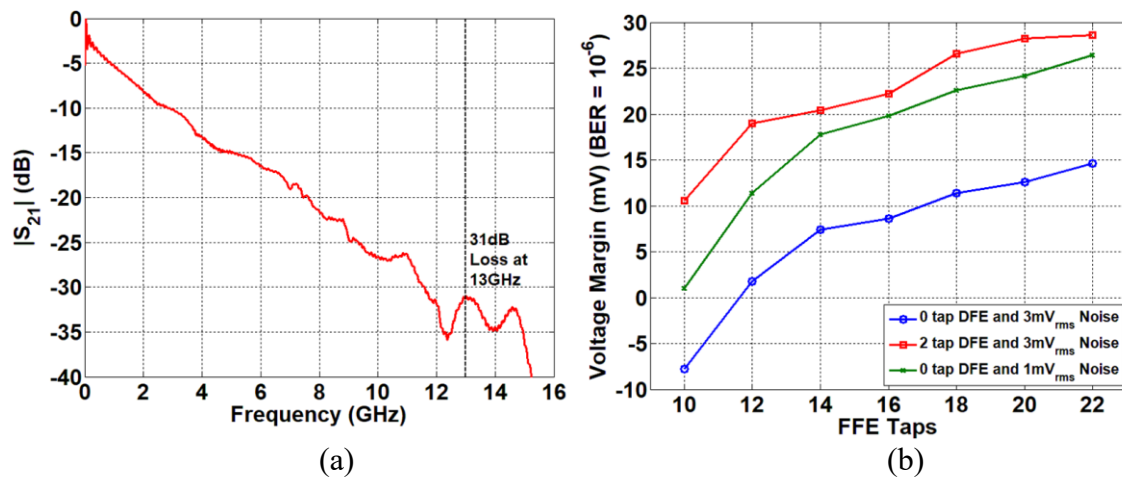
Figure 4.1. (a) Channel with 31dB loss at a frequency of 13GHz and (b) Voltage margin improvement with a DFE at a BER of 10^{-6} with a 2-tap DFE for 52Gb/s operation.

4.1.1 PAM-4 DFE Loop-Unrolling

The concept of loop-unrolling was introduced in section 2.2.2. It was shown that while loop-unrolling significantly reduced the critical path delay, it comes at the cost of increased circuit complexity. This increase in complexity is particularly severe in the case of PAM-4 modulation as the number summers and slicers for each additional DFE tap scales by 4 times instead of 2 times as in PAM-2 DFE. Fig. 4.2 shows a 2-tap loop-unrolled PAM-4 DFE that requires 20 summers and 16 slicers. In general, for an N-tap DFE, the number of summers and slicers needed are $\sum_{i=1}^{N} 4^i$ and 4^N respectively. While the dramatic increase in gate count is one major challenge in a loop-unrolled PAM-4 DFE, the other major challenge is the longer critical path delay in a PAM-4 DFE multiplexer loop compared to the critical path delay in a PAM-2 DFE multiplexer loop.
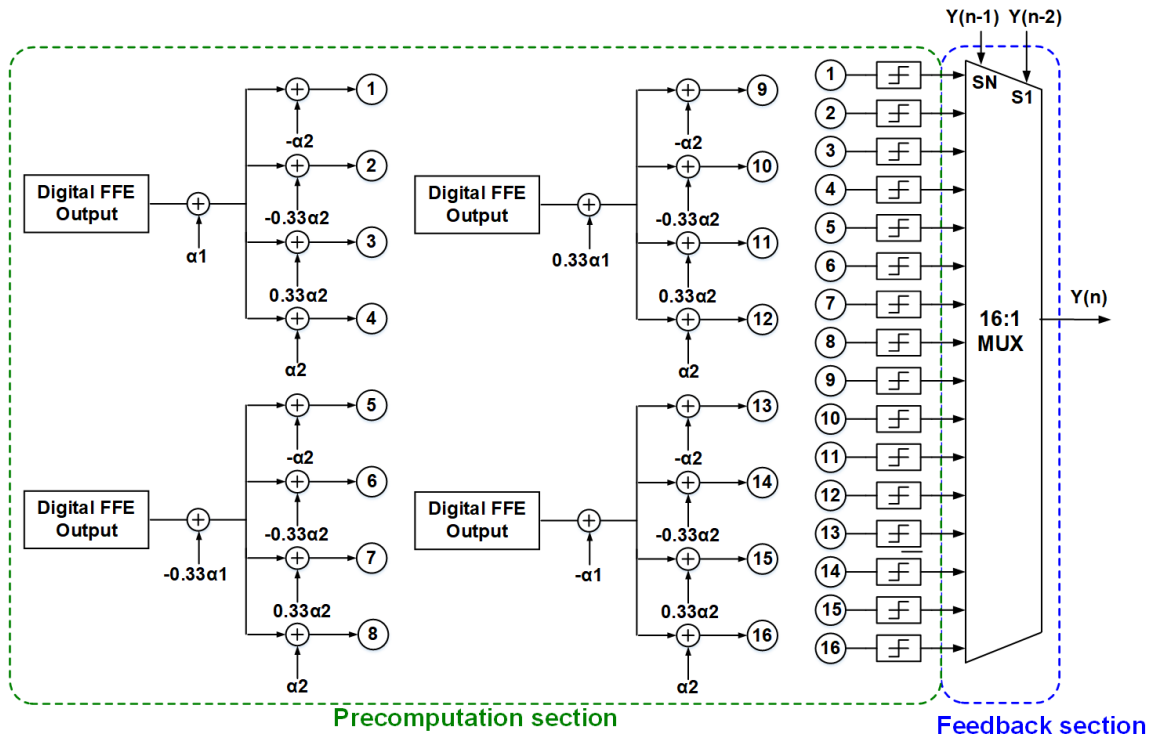
Figure 4.2. DFE loop-unrolling process for a 2-tap PAM-4 DFE.

In a PAM-4 DFE, the critical path has to pass through multiple 4:1 multiplexers, as shown in Fig. 4.3, instead of 2:1 multiplexers as in a PAM-2 DFE. Fig. 4.3 shows the timing paths for a 2-tap PAM-4 DFE implemented with P parallel paths. Either of these two paths or a path that switches between these two paths can be the critical timing path depending on the actual routing and gate delays resulting from digital auto place and route flow. This increased delay necessitates the use of higher look-ahead when look-ahead multiplexing is used.
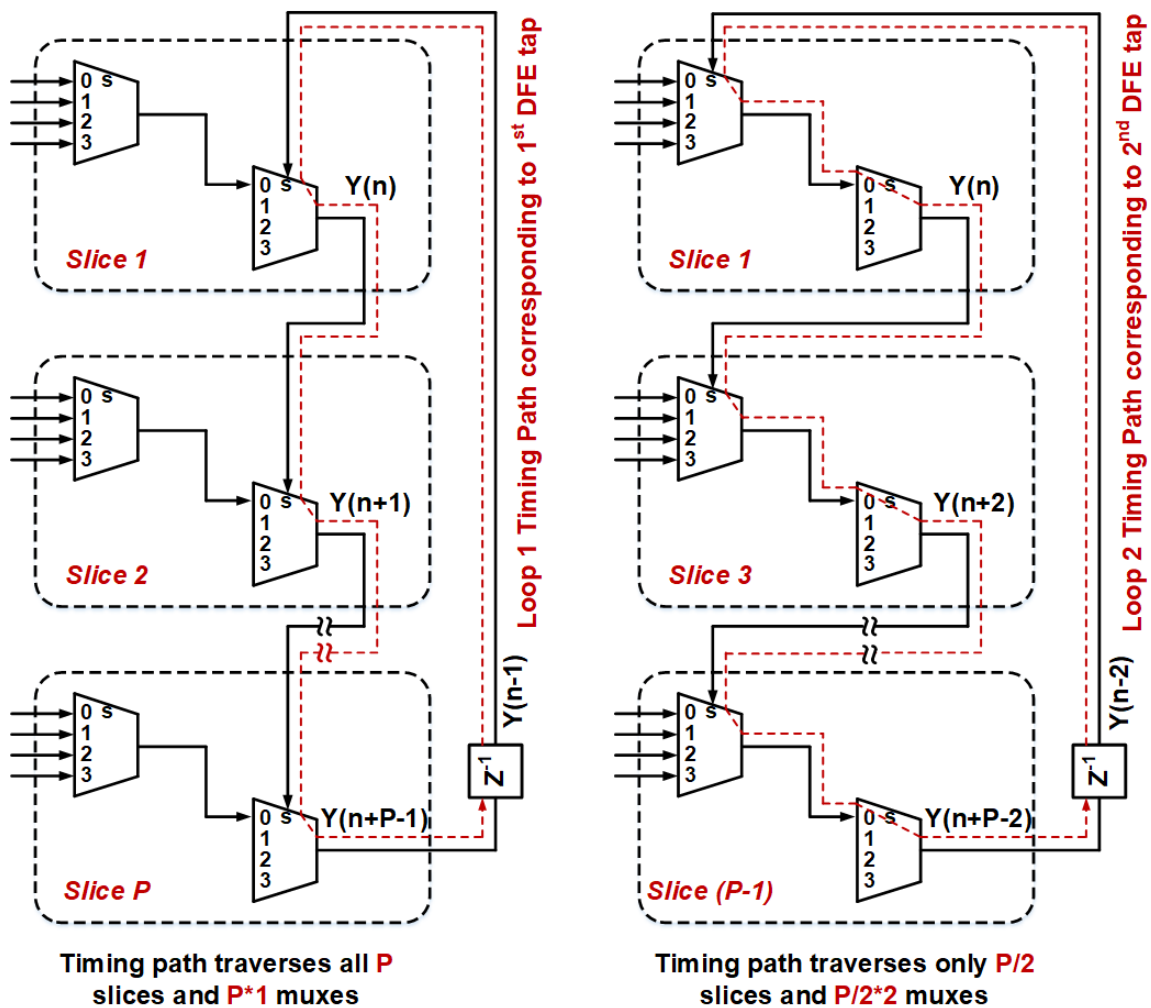
Figure 4.3. Timing paths in a 2-tap PAM-4 DFE implementation with P parallel paths.
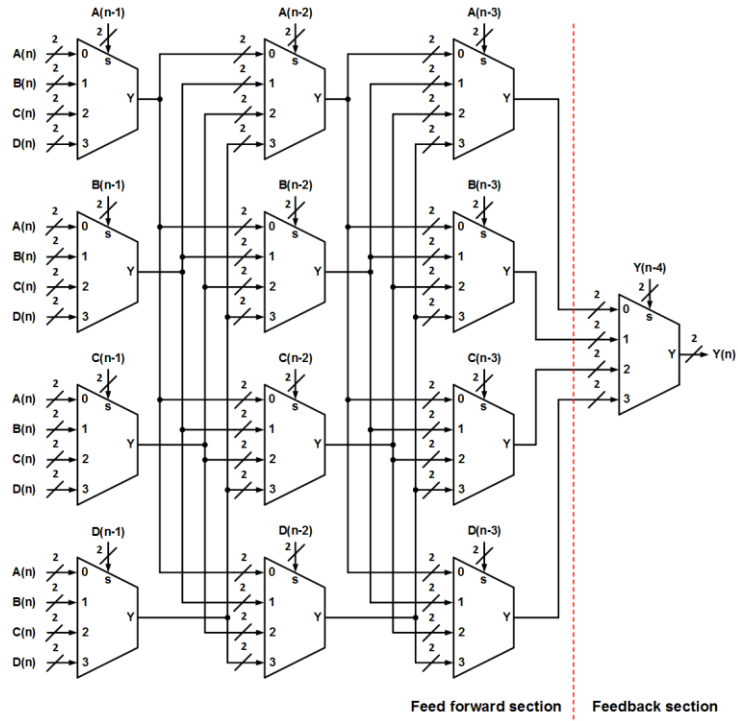
Figure 4.4. 1-tap DFE with a look-ahead factor of 4.
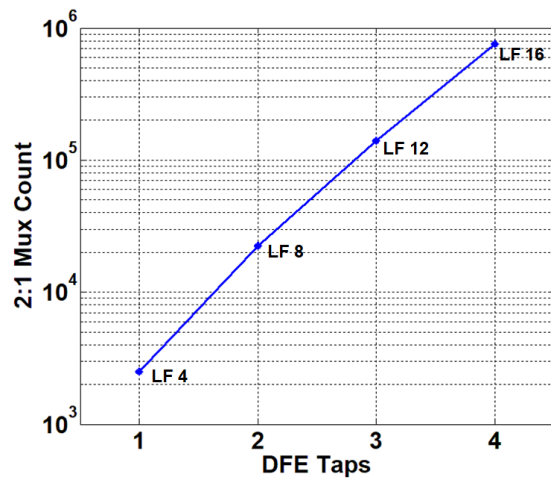
Figure 4.5. 2:1 mux count obtained by digital synthesis flow for a 52Gb/s PAM-4 DFE in 65nm technology for various DFE tap lengths.

Fig. 4.4 shows a 1-tap PAM-4 look-ahead multiplexer with a look-ahead factor for 4. Look-ahead multiplexing technique also results in a dramatic rise in multiplexer count with an increase in DFE tap count as shown in Fig. 4.5. The number of 2:1 multiplexers needed for an N-tap DFE implemented with P parallel paths and a look-ahead factor of LF is $6 * P * ((LF - 1) * 4^N + \sum_{i=1}^{N-1} 4^i)$.

4.2 Receiver Architecture

Fig. 4.6 shows the complete ADC-based receiver architecture. The key components of the architecture are an analog front-end consisting of a CTLE, a 32-way time-interleaved 6-bit SAR ADC, a 64-way parallel DSP consisting of a 12-tap FFE and a 2-tap DFE with an additional parallel FFE for simplifying the DFE architecture, a phase generation block that generates 8 1-UI spaced clocks needed by the track and hold circuits by dividing an external clock by 4, and a baud rate digital phase interpolator based CDR loop employing a Mueller-Muller phase detector. Fig. 4.7 shows the analog front-end consisting of a 2 stage CTLE, a gain stage and a source follower stage. Programmable capacitor banks in the CTLE provides 8.5-15 dB of gain peaking at a frequency of 13GHz. The resistor in the second stage CTLE allows for variable DC gain and is used to ensure the CTLE-VGA front end output swing spans the full scale range of the ADC. By reducing the strength of the ISI components and boosting the main cursor, the CTLE increases the ratio of the main cursor to the quantization noise without having to design a higher resolution ADC. The output of the CTLE drives an 8-way time-interleaved track and hold (T/H) circuit. The schematic of the T/H circuit is shown in Fig. 4.8. The T/H circuit consists of a bootstrapped switch followed by a source follower. Due to the presence of a high pass path comprising of the resistor R and the capacitor C, the source follower reduces to a flipped voltage follower (FVF) at high frequencies leading to bandwidth extension [25] while providing some flexibility is setting the bias conditions.

The cross-connected NMOS transistors Mgb1 and Mgb2 provide a DC gain boost. The T/H buffer has a gain of -2.2dB without gain boosting while with gain boosting the buffer is designed to have a gain of 1.6dB.
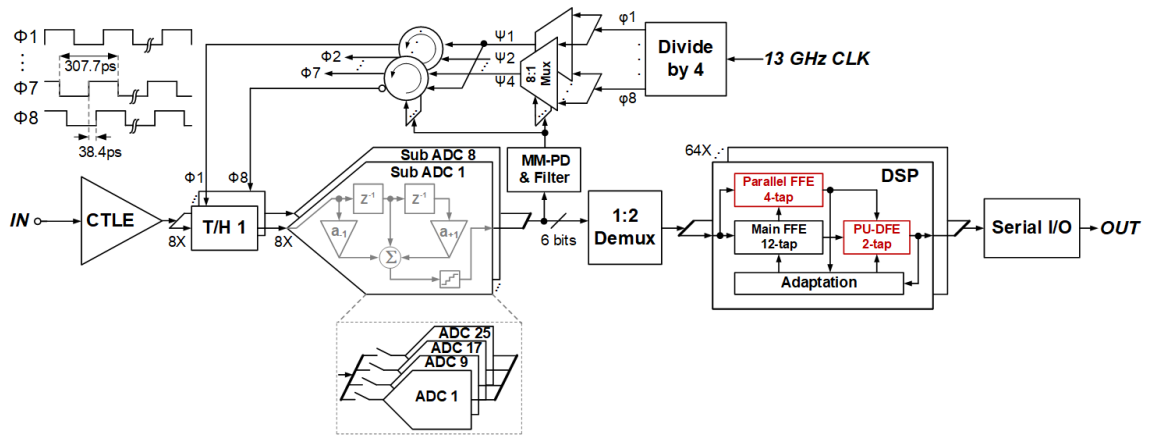
Figure 4.6. The complete receiver architecture.
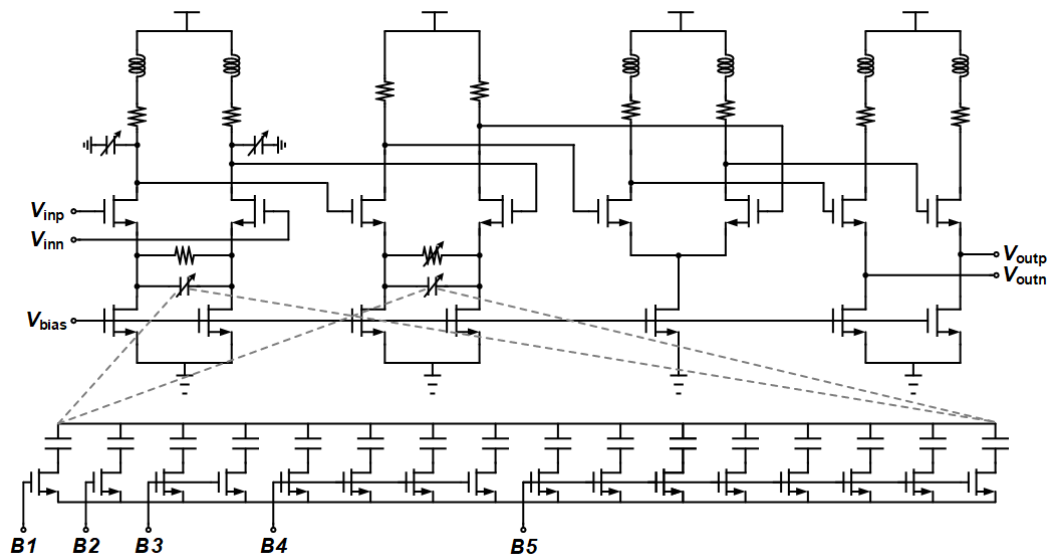
Figure 4.7. 4-stage CTLE-VGA analog front-end.
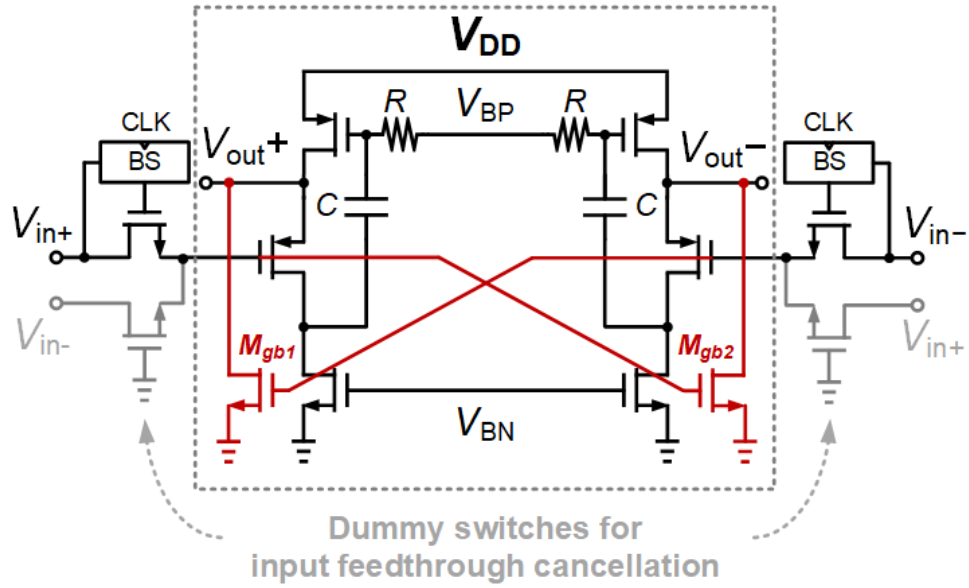
Figure 4.8. Schematic of the track and hold circuit consisting of a bootstrapped switch and gain boosted FVF.
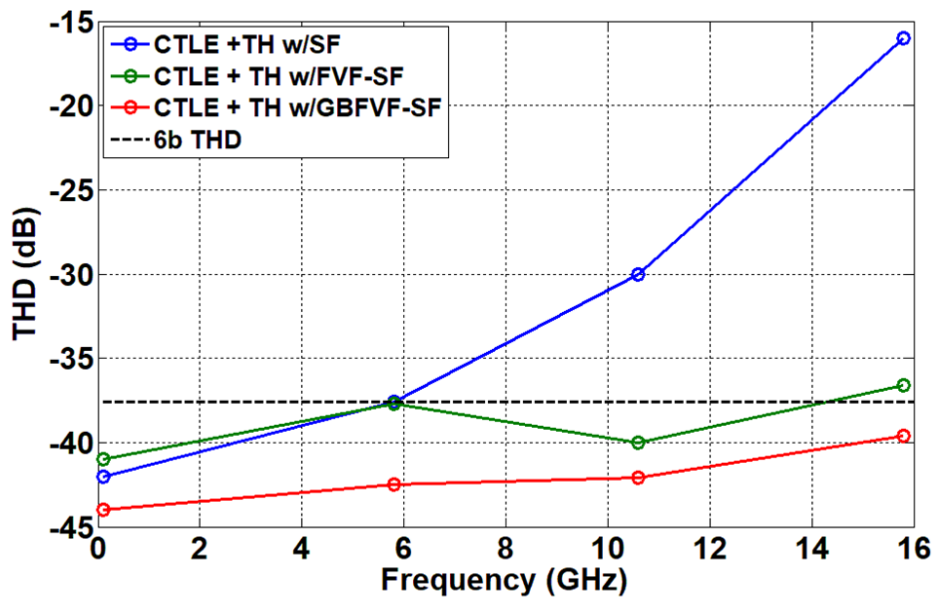
Figure 4.9. Simulated THD comparison for a simple source voltage follower, a FVF, and a gain boosted FVF.

51

For a constant ADC full scale range, this causes the output swing of the stages preceding the T/H buffer to be lower and hence improves their linearity. Fig. 4.9 shows the post-layout linearity in terms of total harmonic distortion (THD) for the analog front-end with the T/H buffer being a simple source follower, the bandwidth extended FVF and the gain-boosted FVF. The gain-boosted FVF shows an improvement of more than 3dB up to 10GHz.

Eight of these T/H blocks are arranged in a time-interleaved fashion with each T/H block sampling at 3.25 GS/s using 8 1-UI spaced 3.25 GHz clocks to give an aggregate sampling rate of 26 GS/s. Bias current control is provided in the T/H buffer to calibrate gain mismatches between the interleaved T/H blocks. The 8 critical sampling phases are generated from a differential 13 GHz clock by dividing it with a CML latch based divide by 4 block as shown in Fig. 4.10 [26]. The 38.4ps spaced phases then pass through a bank of 64 current mode phase-interpolators controlled by the CDR loop [27-28]. The output of the phase interpolators are skew calibrated by a digitally controlled variable delay line with a delay step of 90 fs. The sampling phase is set by a baud rate CDR loop that employs a Mueller- Muller phase detector and proportional and integral loop filter [29]. A 3-tap FFE embedded in the ADC provides additional analog equalization before quantization noise is added to the signal. The equalization provided by the CTLE and the embedded FFE allows the placement of the CDRs Mueller-Muller phase detector directly after the ADC to avoid excessive loop delay [30]. The ADC employed in this design is a 32-way time-interleaved 6-bit SAR ADC with a 2-bit/stage, loop-unrolled unit ADC. The time-interleaved ADC has 8 sub-ADCs, leading to 8 critical sampling phases, with each sub-ADC having 4 unit ADCs. The DSP, which has 64 parallel slices, employs a FFE-DFE combination with an additional parallel FFE to significantly reduce the DFE complexity. The main FFE has 12 taps with 3 pre-cursor and 8 post-cursor taps while the DFE has 2 loop-unrolled taps canceling the 1st two post-

cursor ISI components. The parallel FFE has 4-taps with 1 pre-cursor and 2 post-cursor taps. All

the coefficients in the DSP are set through the SS-LMS algorithm.
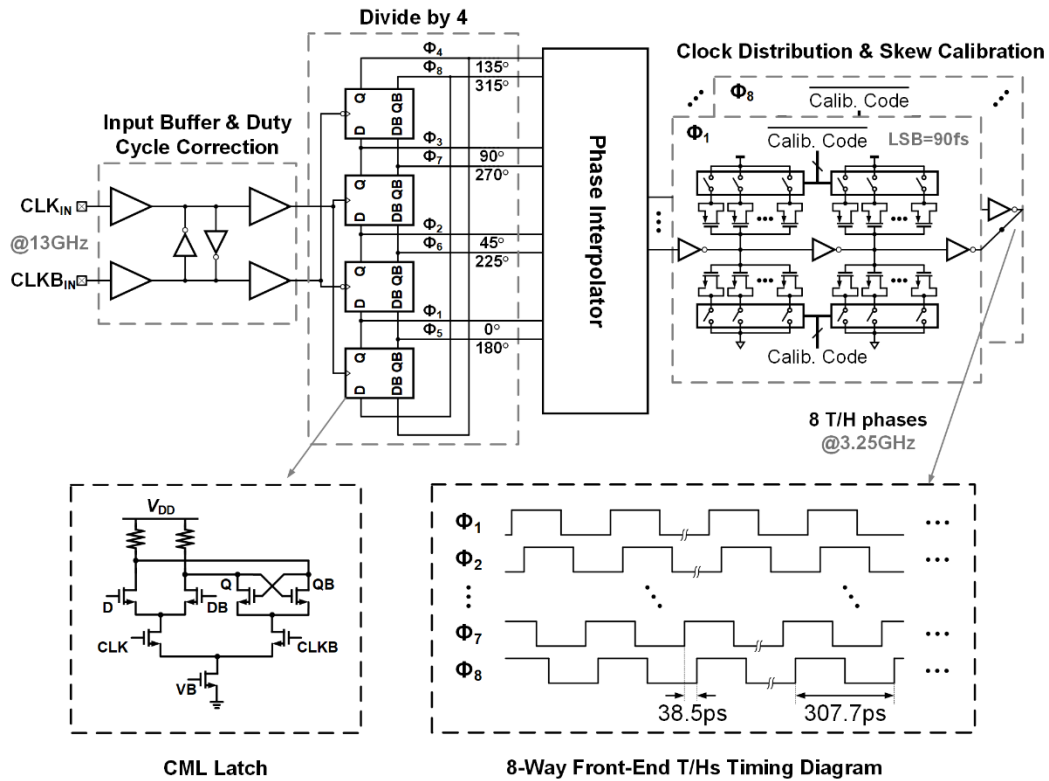
Figure 4.10. Phase generation block that generates the 8 1-UI spaced phases by dividing an
external 13GHz clock and the timing diagram showing the 8 phases.

4.3 ADC Design

Time-interleaved SAR ADCs are a power efficient way of implementing multi-GS/s ADCs

in CMOS technology. However, it is desirable to keep the time-interleaving factor low in order to

reduce the loading on the analog front-end to simplify the time-interleaved channel mismatch

calibration. This requires the design of high speed unit SAR ADCs which can be challenging. In

order to speed up the unit SAR ADC conversion speed, techniques such as 2bit/stage [31] and

loop-unrolling [32] can be employed. Previous 2bit/stage ADCs employ multiple reference DACs

53

and 3 comparators in each 2bit/stage flash ADC [31,33]. This leads to an increased loading and power consumption for the track and hold stage and a decrease in the FFE coefficient range when FFE is embedded in the ADC using a binary FFE DAC [6]. This design introduces techniques to address these issues as will be described in the sections that follow.

4.3.1 Time-Interleaved ADC Architecture

Fig. 4.11 shows the block diagram of the 32-way 6 bit 26 GS/s converter with 3-tap embedded FFE. The front-end T/H consists of 8 sub channels working at fs/8 = 3.25 GS/s, and each sub T/H drives 4 unit asynchronous 2b/stage SARs operating at fs/32 = 812.5 MS/s. Each unit ADC digitizes the difference between its current sample that is sampled on the reference DAC and the scaled and summed immediately preceding and succeeding symbols that are sampled on a dedicated non-binary FFE DAC, to implement a 3-tap FFE with 1-precursor and 1-postcursor tap.

4.3.2 Unit ADC Architecture

Fig. 4.12 shows the loop-unrolled 2-bit/stage unit ADC that has three stages for the 6-bit conversion. Each stage employs a 2-bit flash ADC as the quantizing block with the reference levels internally generated by intentionally skewed comparator regeneration stages. The reference levels for the flash ADC of each stage scale according to the stage, from 0 to $\pm 1/4 V_{ref}$ for the second stage to $\pm 1/64 V_{ref}$ for the third stage and hence are not dynamically set. This allows the use of a single DAC and removes the overhead of multiple DACs present in other multi-bit/stage implementations [31,33]. The main cursor signal is top-plate sampled to avoid any signal attenuation caused by the comparator input capacitance and routing parasitics.

32-Way TI ADC with 3-Tap Embedded FFE
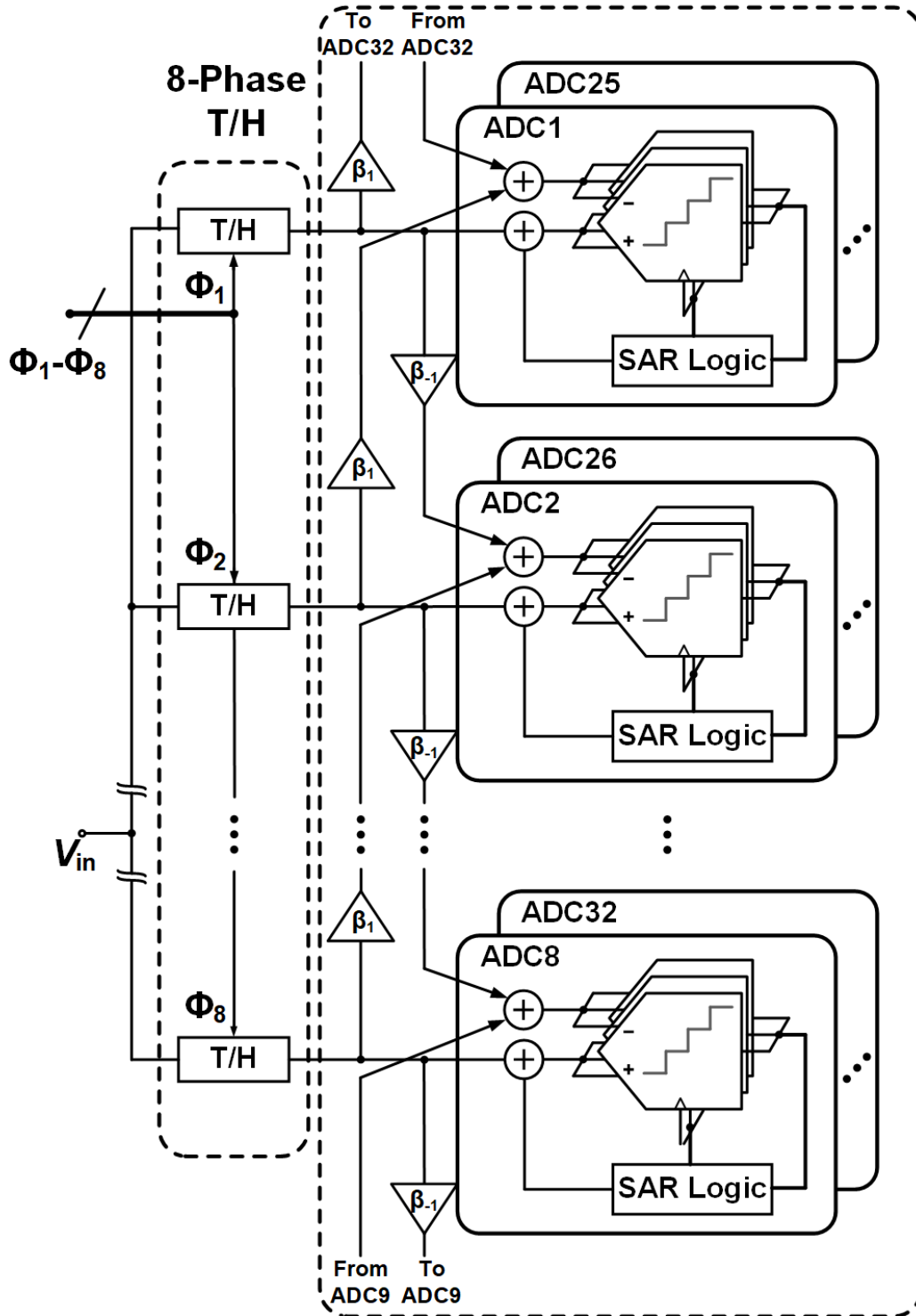
Figure 4.11. Block diagram of the 32-way time-interleaved SAR ADC.
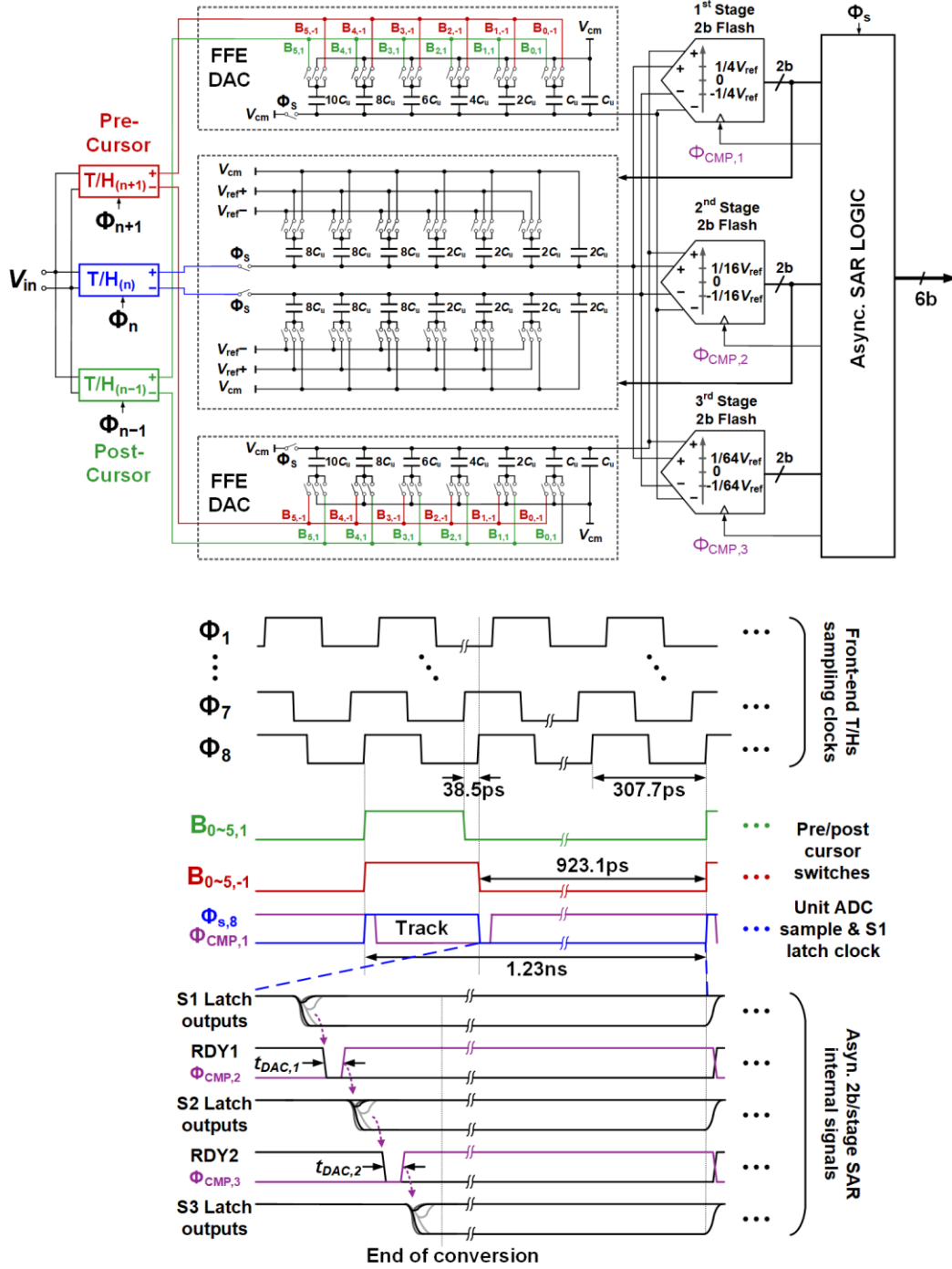
Figure 4.12. Unit ADC architecture and timing diagram.

The unit SAR ADCs operate on a 812.5MHz 25% duty cycle clock leading to a track time of 307.7ps and a conversion time of 923.07ps as shown in Fig. 4.12. Loop-unrolled architecture leads to a significant reduction in the logic delay in the feedback path from the comparator to the DAC switches [32]. It also ensures that the comparators need to be reset until all the stages have completed evaluation. The flash ADC stages 1 and 2 generate the RDY signal which triggers the comparison in the subsequent stage. Delay lines are provided to delay the RDY signal to ensure sufficient time for DAC settling (tDAC1 and tDAC2). Each of the 2-bit stages generate a 3-bit thermometer code that is fed back to a segmented thermometer DAC directly without an additional decoder to reduce logic delay. The 4b custom DAC is constructed with Cu = 1fF unit capacitors which allows for adequate matching for 6-bit resolution and the merged switch capacitor scheme (MCS) [34] is employed for good switching efficiency. At the end of conversion of all the three stages, the comparators are reset while the signal is being tracked and their outputs are retimed using the same clock.

In order to embed a 3-tap FFE, samples from T/H blocks sampling the pre and post signal values with respect to the current signal value are sampled onto the bottom-plate of a differential FFE DAC. These pre and post samples are scaled and summed on the FFE DAC before they are effectively subtracted from the main cursor sample due to the differential connection at the flash ADC input. The use of 2-bit flash ADCs as the quantization block presents the challenge of the FFE DAC being loaded with 9 comparator input stages. There is the potential for significant attenuation from the comparator input capacitance due to the pre and post samples being bottom-plate sampled, which could lead to a decreased range for the FFE coefficients.
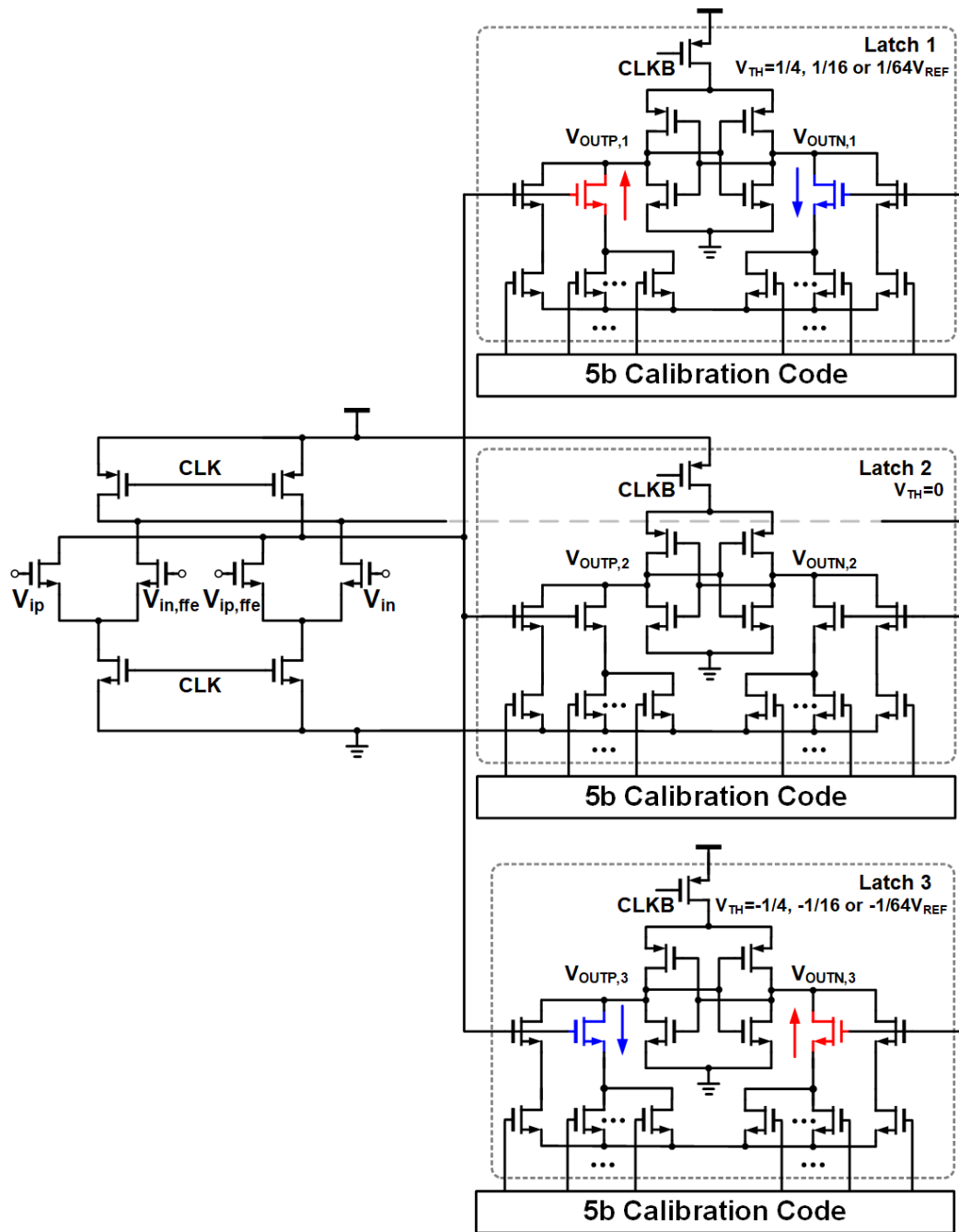
Figure 4.13. Shared-input stage 2-bit flash ADC schematic.
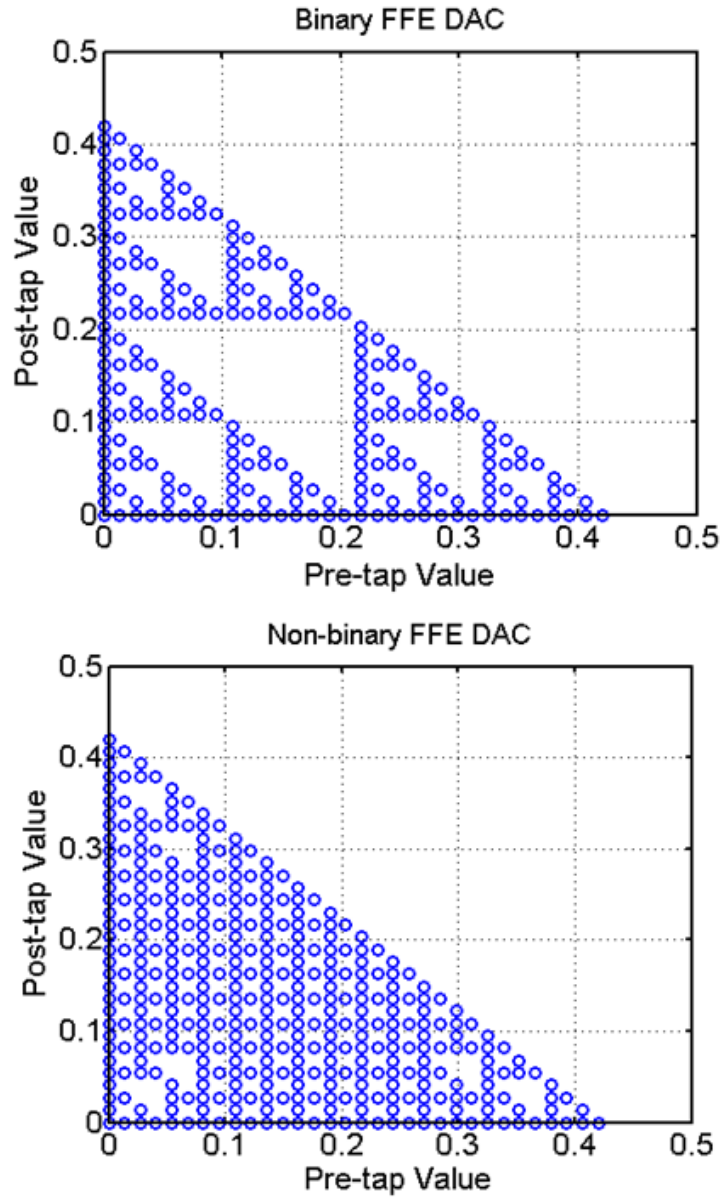
Figure 4.14. Improved 6-bit resolution embedded FFE coefficient coverage map with non-binary FFE DAC.

In order to reduce the loading of the comparators on the FFE DAC, the input stage of the 3 comparators of the flash ADC are shared (Fig. 4.13). This reduces the effective DAC loading by 3X. Since the pre and post FFE samples are sampled on the same DAC, not all FFE coefficient

combinations are possible. As shown in Fig. 4.14, improved coefficient coverage is achieved with the implementation of a non-binary FFE DAC. Bottom plate sampling on the FFE DAC results in a gain of 0.48, which sets the range for the tap coefficient values.

4.4 DSP Design

The key architectural details of the DSP is presented in this section. As shown in Fig. 4.15, the main path through the DSP consists of a 12-tap FFE and a 2-tap DFE. In addition a low complexity parallel FFE with 4 taps is utilized to significantly reduce the DFE complexity.

4.4.1 Main and Parallel FFE

In comparison to an NRZ receiver, a PAM-4 receiver is more sensitive to residual ISI [30]. This necessitates the use of a longer span FFE than generally used in an NRZ receiver. However, the implementation of the FFE taps itself can be modulation format independent. Canonical signed digit (CSD) representation, which represents numbers with the least number of 1s possible, is a well-known power efficient way of representing numbers when performing multiplications with a constant number, like in the case of an FFE.
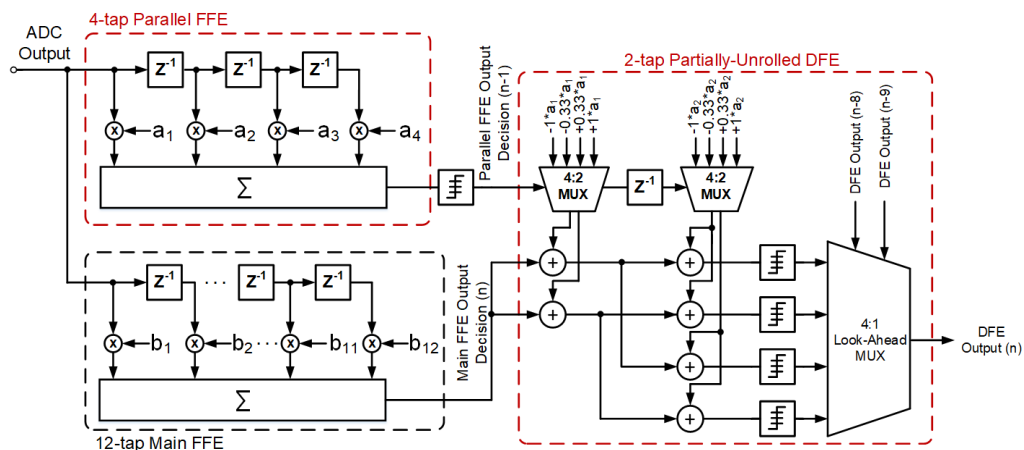
Figure 4.15. DSP architecture showing the 12-tap main FFE, 4-tap parallel FFE and the 2-tap loop-unrolled PAM-4 DFE. Reprinted with permission from S. Kiran et al, IEEE ©April 2018

60

In this work, the FFE coefficients are represented using CSD representation with an additional restriction of having only a maximum of 2 1s for each coefficient. This restriction ensures each multiplication operation reduces to 2 shifts and 1 addition operation. Additional simplification of the FFE is achieved by having a reduced range for taps 9 to 12 of the main FFE since these tap values are typically small. The taps of the main FFE are co-optimized with the DFE according to the MMSE solution using the SS-LMS algorithm. This can result in two significant ISI terms at the first two post-cursor positions that will be cancelled by the DFE later on. Hence, at the output of the main FFE, there is very little useful information that can be further exploited for simplifying the DFE architecture. The taps of the parallel FFE are set to achieve the lowest BER possible at its output, again using the MMSE criterion. The resulting partially equalized signal at the parallel FFE output can be now be exploited to simplify the DFE architecture as will be described next.

4.4.2 Partially-Unrolled DFE

The key idea of the partially-unrolled DFE is as follows. As described earlier, during the loop-unrolling process in the DFE, all four possible values for the previous symbols are used to precompute all the possible equalized values for the current symbol. For example, in a 2-tap PAM-4 DFE, to compute all the possible equalized values for the symbol at time n, 4 possible choices for the symbol at time $n-1$ and 4 possible choices for the symbol at time $n-2$ are used, resulting in 16 possible equalized symbol values. If the previous symbols have been partially equalized, as it is at the output of the parallel FFE, then 2 of the most unlikely values for each of the previous symbols can be safely discarded during the loop-unrolling process without incurring an error that impacts the overall target BER. Hence, it can be said that the loop is only partially unrolled. With reference to Fig. 4.16, which shows the PDF of the received signal at the output of parallel FFE

and the CDF for normalized transmitted symbol 0.33, if the previous symbol falls in region 1, then the transmitted symbol most likely corresponds to the normalized values of -1 or -0.33. Hence, during the loop unrolling process, DFE coefficients corresponding to symbols 0.33 and 1 are not used in precomputing the possible equalized symbols for the current symbol. Similarly, for symbols falling in region 2, symbols -1 and +1 are eliminated in the loop- unrolling process and for symbols falling in region 3, symbols -1 and -0.33 are eliminated during the loop unrolling process. Continuing with the example of the 2-tap DFE, since there are now 2 choices for both the symbols at time instants $n - 1$ and $n - 2$, there are only 4 possible equalized values for the current symbol. The number of sums to be computed has therefore been reduced from 16 to 4 for a 2-tap DFE as shown in Fig. 4.16.

Apart from reducing the gate count due to a lower number of summers and slicers required, PU-DFE also reduces the number of multiplexer required to implement the look-ahead multiplexer loop. The critical feedback timing path in a conventional PAM-4 DFE implementation consists of a 4:1 multiplexer whereas, in PU-DFE it consists of a 2:1 multiplexer. This reduces the critical path length by nearly half and doubles the maximum data rate achievable for a given look-ahead factor in the multiplexer loop. The look-ahead multiplexer loop in a PU-DFE is shown in Fig. 4.17.

4.4.3 Critical Path Optimization

For each of the past symbols that have been loop-unrolled, a 2-bit past decision has to choose the correct choice among the 2 options generated during the loop-unrolling process. With reference of Fig. 4.18(a), when the parallel FFE output falls in Region 1 the input to summing elements in the DFE are -1*a1 and -0:33*a1 signifying that the partial decision for the symbol is 00 and 01 respectively. Now if the actual decision on the previous symbol, which is fed back to the multiplexer after a delay of LF due to the fact that the multiplexer has a look-ahead factor of

LF, is 00 then the select line S of the multiplexer has to be 0 and if the it is 01 then the select line has to be 1. This is shown in the table on the right. Note that the output of the decision elements are assumed to be gray coded. Similar analysis can be carried out for symbols falling in Region 2 and Region 3. The key point to note from the table in Fig. 4.18(a) is that for the same value of the delayed previous symbol Y_{n-LF}, the select line for the multiplexer can be either a 0 or 1 depending on the region where the parallel FFE output happens to fall in. This ambiguity is resolved by using an additional variable R to indicate which region the parallel FFE output fell in. The select line can be written as a function of R and Y_{n-LF} as shown in Equation 4.1. The additional combinational logic delay of 3 gates in the path of the select line of the final multiplexer increases the critical path delay and therefore any advantage that can be obtained with the PU-DFE architecture in terms of reduced delay in the critical path might be lost due to this overhead.

$$S = R\overline{Y_{n-LF}[0]} + Y_{n-LF}[1]\overline{Y_{n-LF}[0]} + RY_{n-LF}[1], \tag{4.1}$$

This overhead logic can be removed by 2 simple modifications to the DFE architecture. First, the PAM-4 levels are binary coded and second the input to the summing elements in the DFE selected through the 4:2 mux are swapped when the parallel FFE output falls in region 2. This results in the implementation as shown in Fig. 4.18(b) and from the resulting table it is clear that the select line of the multiplexer, S, is simply $Y_{n-LF}[0]$. Hence, no additional combinational logic is necessary to generate the select line. The additional delay introduced in the 4:2 mux for swapping its output in Region 2 can be easily tolerated as this delay is not in the timing critical multiplexer loop. This simple trick can nearly double the maximum achievable data rates.
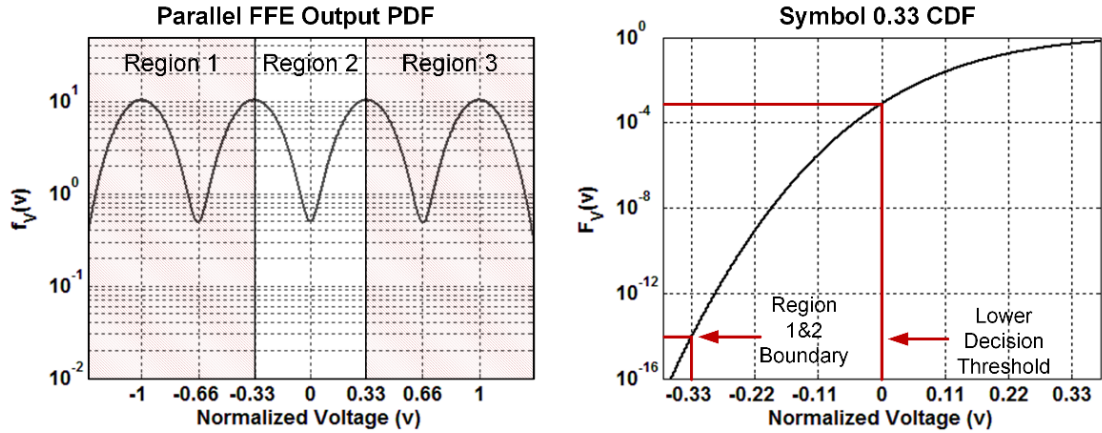
Figure 4.16. PDF of the signal at the output of the parallel FFE and the CDF for 0.33 symbol. Reprinted with permission from S. Kiran et al, IEEE ©April 2018
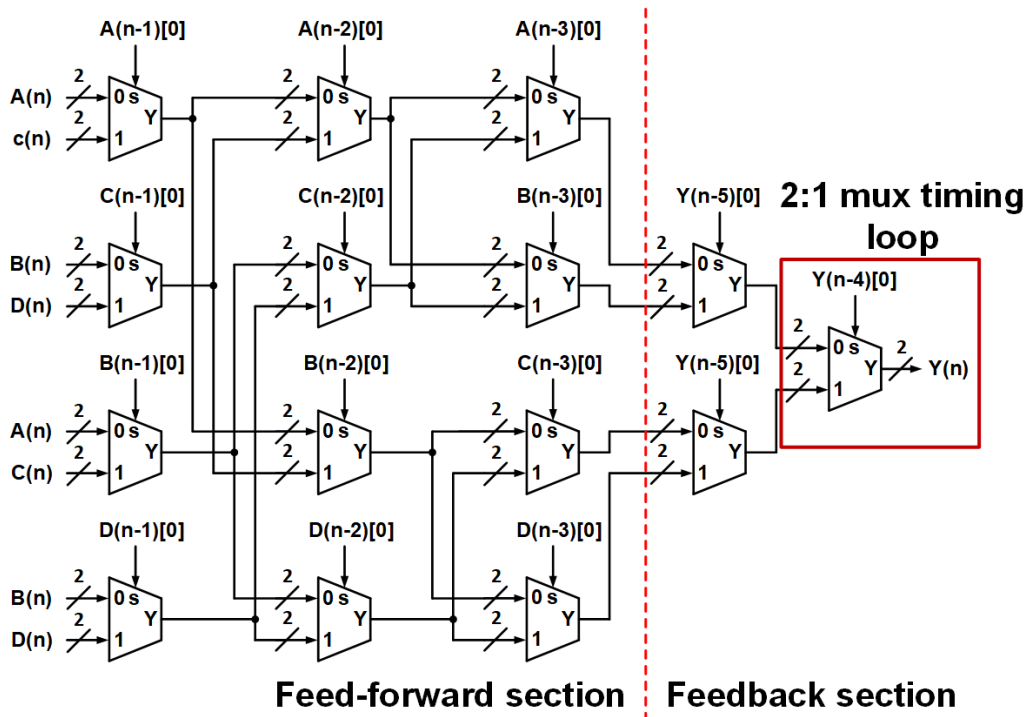
Figure 4.17. Partially-unrolled 2-tap PAM-4 look-ahead multiplexing with a look-ahead factor of 4.
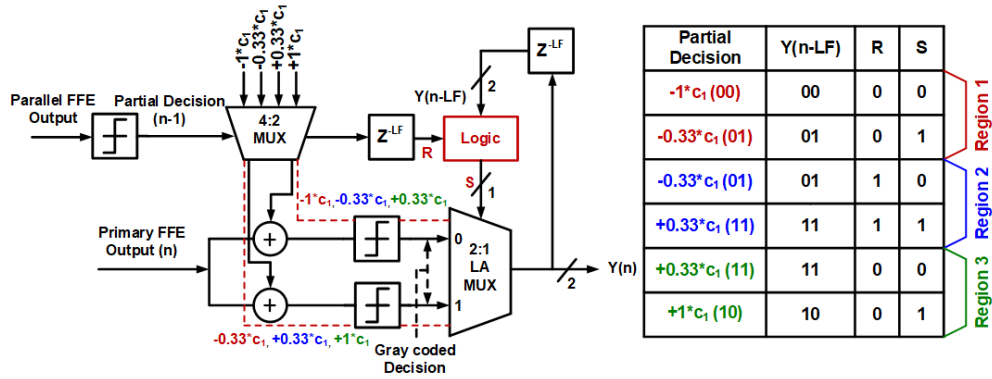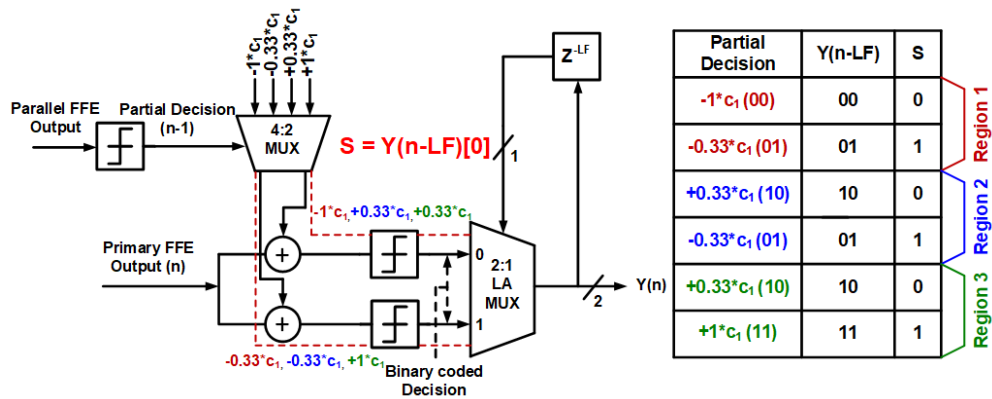
Figure 4.18. (a) Straight forward and (b) optimized implementation of mux selection logic.

Fig. 4.19 compares the gate count for a 2-tap conventional PAM-4 DFE and PU-DFE in 65nm technology for various look-ahead factors implemented using a digital synthesis flow. The PU-DFE architecture has about 3X lower gate count compared to the traditional architecture. Fig. 4.20 shows the power consumption comparison for the two architectures with the overhead from the parallel FFE included in the case of the PU-DFE architecture. PU-DFE architecture has about 2X lower power consumption. Fig. 4.21 shows the maximum achievable data rate in 65nm

technology for the two architectures with the PU-DFE architecture achieving about 2X higher data rate compared to the conventional architecture.

4.4.4 Advantages of PU-DFE

The advantages of PU-DFE are summarized in Table 4.1.

Architecture	Number of Summers	Number of Slicers	Number of multiplexers	Timing Loop
Conventional DFE	$\sum_{i=1}^{Ndfe} 4^i$	4^{Ndfe}	$6 * (4^N(LF - 1) + \sum_{i=1}^{N} 4^{N-i})$	4:1 multiplexers
PU-DFE	$\sum_{i=1}^{Ndfe} 2^i$	2^{Ndfe}	$2 * (2^N(LF - 1) + \sum_{i=1}^{N} 2^{N-i})$	2:1 multiplexers

Table 4.1. Complexity comparison between conventional PAM-4 DFE and PU-DFE.
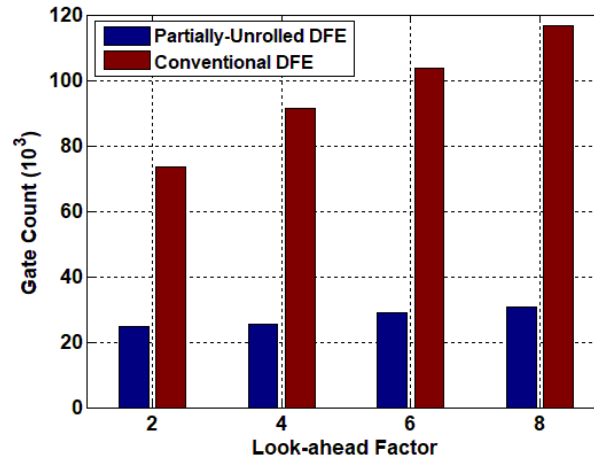
Figure 4.19. Gate count comparison between a conventional DFE and PU-DFE for a 2-tap PAM-4 DFE in 65nm technology.
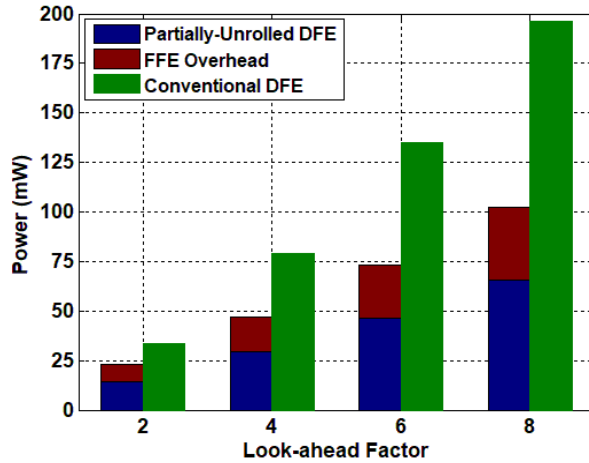
Figure 4.20. Power consumption comparison between a conventional DFE and PU-DFE for a 2-tap PAM-4 DFE in 65nm technology.
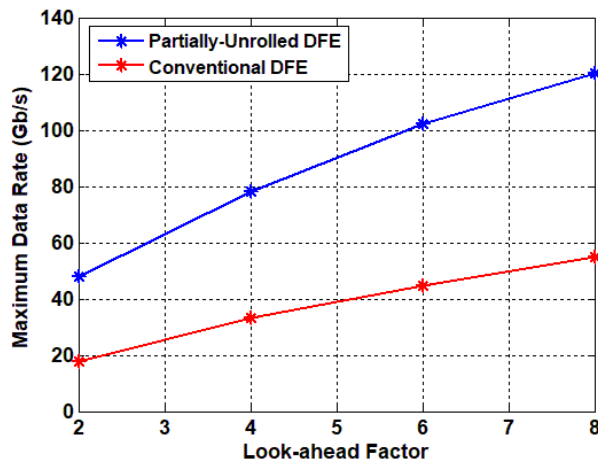
Figure 4.21. Maximum achievable data rate comparison between a conventional DFE and PU-DFE for a 2-tap PAM-4 DFE in 65nm technology.

4.5 Measurement Results

Fig. 4.22 shows the chip micrograph of the PAM-4 ADC based prototype fabricated in GP 65nm process. The total chip area is 2.61mm2 with the core ADC and the DSP occupying 0.41mm^2 and 1.17mm^2 respectively. A set of 6 high-speed output buffers with a multiplexer at the input that

can select either the ADC output or the DSP output help characterize the ADC and the DSP

separately. The receiver is characterized at 2 data rates of 32Gb/s and 52Gb/s corresponding to

ADC sampling rates of 16GS/s and 26GS/s respectively.

4.5.1 ADC Characterization

Before the ADC characterization begins, termination resistor tuning and CTLE-VGA

analog front-end offset calibration is performed. Each of the 284 comparator offsets in the TI-ADC

are calibrated by applying a differential DC input equal to the desired threshold for that particular

comparator and tuning the threshold of the comparator until an equal distribution of ones and

zeroes are obtained at the output. Skew between the different sampling phases is calibrated using

a foreground technique where a sinusoid at a frequency equal to the sampling rate is applied and

the output from the 8 sub-ADCs are made equal by digitally tuning a bank of variable delay lines.

Gain calibration is performed by tuning the bias current of the T/H buffer.
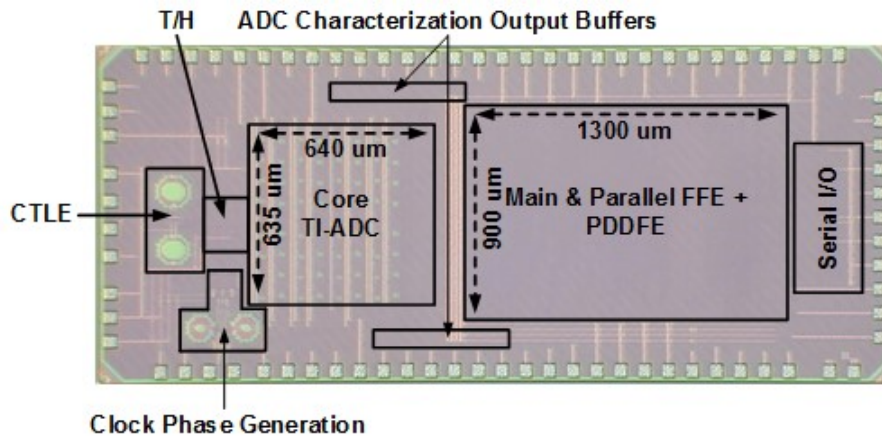
Figure 4.22. ADC-based PAM-4 chip micrograph Reprinted with permission from S. Kiran et al,
IEEE ©April 2018.
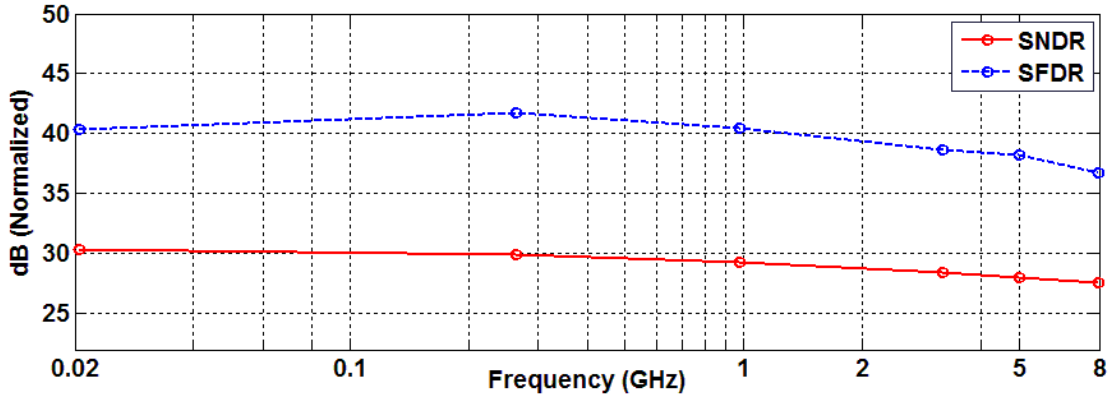
Figure 4.23. SNDR and SFDR vs input frequency at fs = 16GHz.
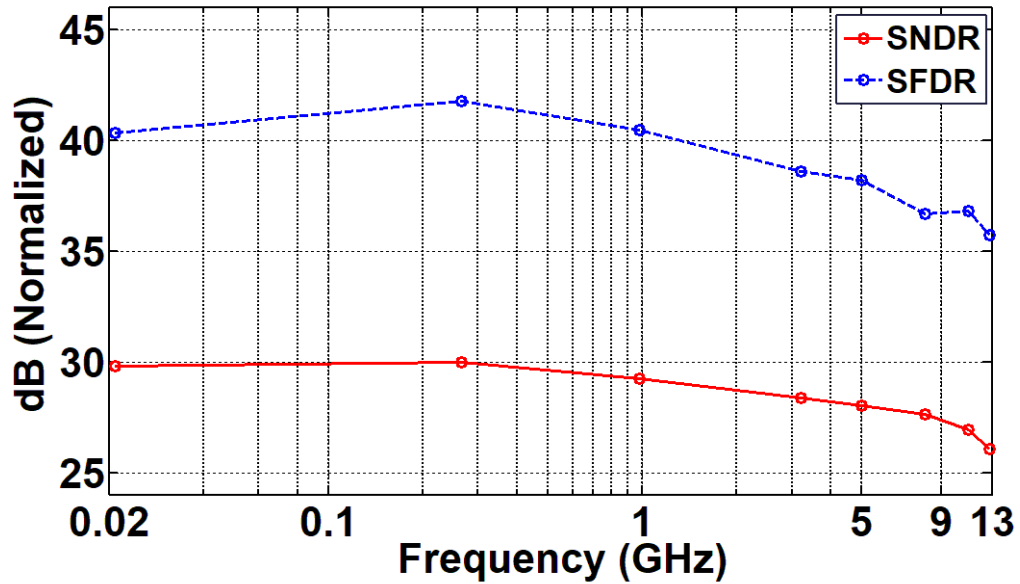
Figure 4.24. SNDR and SFDR vs input frequency at fs = 26GHz.

Fig. 4.23 and Fig. 4.24 shows the SNDR and SFDR as a function of the input frequency for a sampling rate of 16GS/s and 26GS/s respectively. A low frequency SNDR of 30.29 dB giving an ENOB of 4.74 bits is achieved for both sampling rates of 16GS/s and 26GS/s. At the sampling rate of 16GS/s, a Nyquist frequency SNDR of 27.58 giving an ENOB of 4.29 bits is achieved while

at the sampling rate of 26GS/s, a Nyquist frequency SNDR of 26.14dB giving an ENOB of 4.05 bits is achieved. The high frequency SNDR is limited by jitter and residual timing skew. Fig. 4.25 shows that the maximum DNL and INL values for the ADC are -0.22LSB and -0.53LSB.
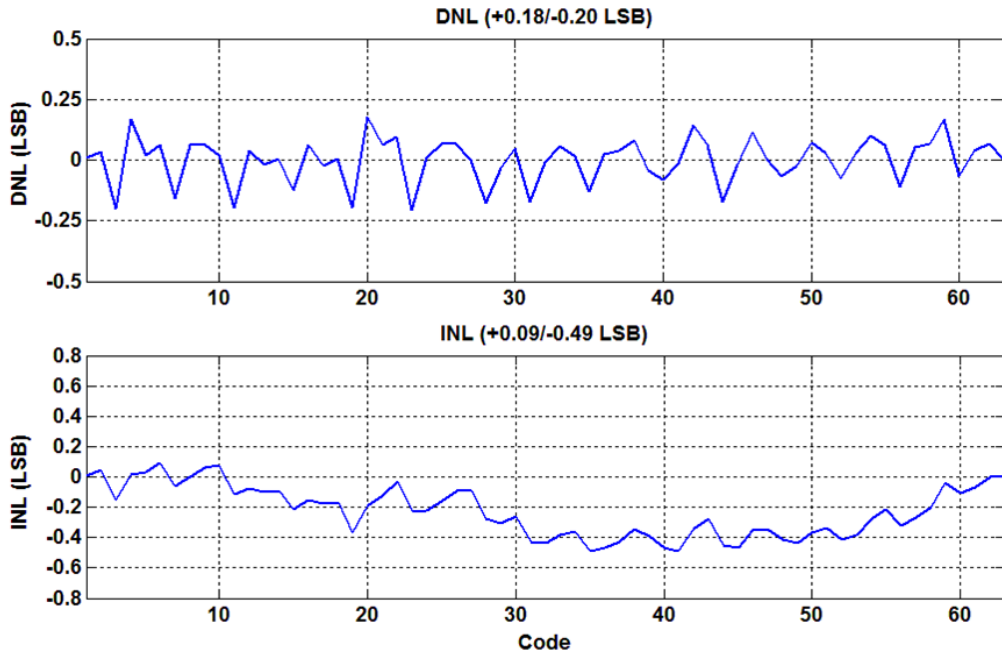
Figure 4.25. Measured INL/DNL plot.

4.5.2 Analog Front-End Characterization

The frequency response of the analog front-end is characterized by sweeping the input signal frequency while looking at the ADC output. The resulting frequency response for various CTLE settings is shown in Fig. 4.26. The analog front-end provides a gain peaking of 8.5dB to 15dB at 13GHz.
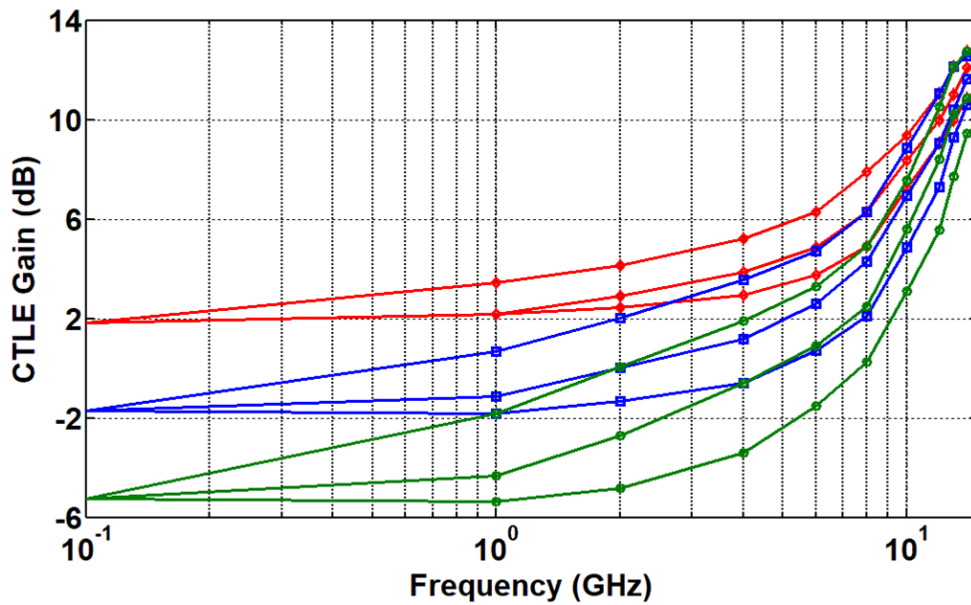
Figure 4.26. Measured CTLE magnitude response.

4.5.3 Receiver Characterization

The measured channel responses for both 32Gb/s and 52Gb/s characterization is shown in Fig. 4.27. The complete receiver performance is characterized at two data rates of 32Gb/s and 52Gb/s using the test setup in Fig. 4.28 (top and bottom respectively). For 32Gb/s operation two NRZ bitstreams from a Xilinx FPGA board are power combined to produce PAM-4 data. The data is then transmitted over two channels with effective losses of 27dB and 30dB. The measured timing bathtub curve is shown in Fig. 4.29(a). For the 27dB loss channel a BER $< 10^{-11}$ is achieved while for the 30dB loss channel a BER $< 10^{-9}$ is achieved. For testing at 52Gb/s, PRBS-15 PAM-4 data from a custom Tx chip with no transmit equalization passed over two channels of losses 26dB and 31dB. The resulting BER performance is shown in Fig. 4.29(b). A BER less than 10^{-8} is achieved for a 26 dB loss channel and a BER of less than 10^{-6} is achieved for a 31 dB loss channel. For both 32Gb/s and 52Gb/s operation the timing bathtub curves are obtained by stepping the phase

71

interpolator codes with the CDR in open-loop. Results with the CDR activated are also shown for both 32Gb/s and 52Gb/s operation for channels losses of 27dB and 26dB respectively, verifying that the CDR locks near the optimal BER point. The recovered clock jitter histogram showing random jitter of 939fs$_{rms}$ is shown in Fig. 4.30.

      Table 4.2 summarizes the receiver performance and compares it with other ADC-based receivers at data rates above 25 Gb/s. The complete 52Gb/s ADC-based receiver achieves a power efficiency of 8.05 pJ/bit, including all the front-end, ADC, and DSP power. Utilizing the CTLE front-end, embedded 3-tap FFE in the ADC, and the DSP with the PU-DFE allows for compensation of comparable channel loss to the other PAM-4 receivers without employing any transmit equalization.
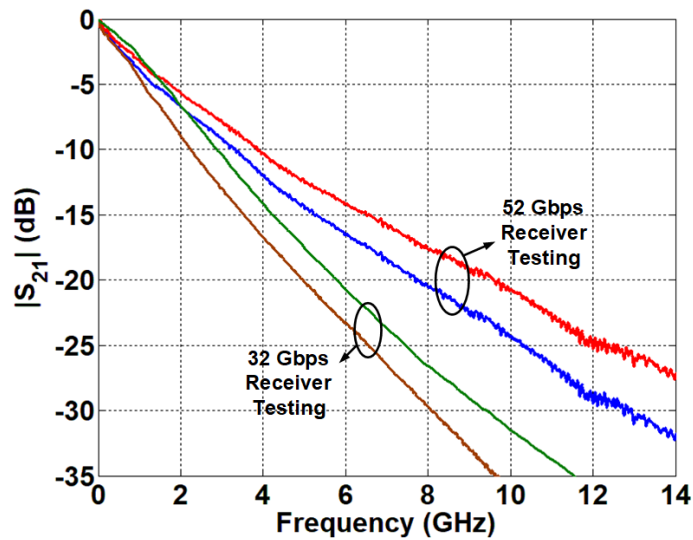
Figure 4.27. Measured channel responses.
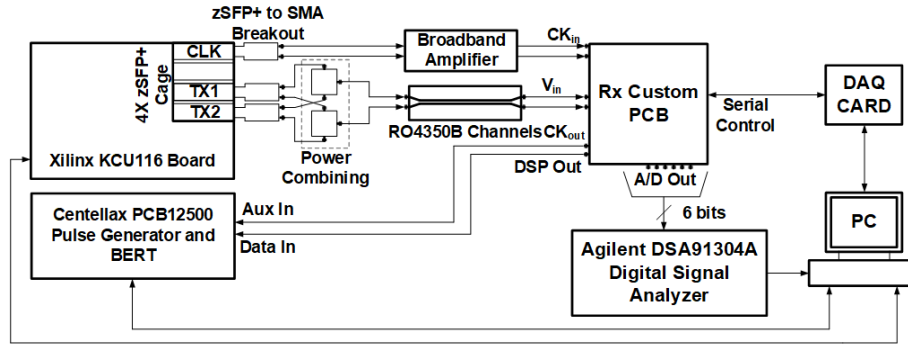
32Gbps Test Setup
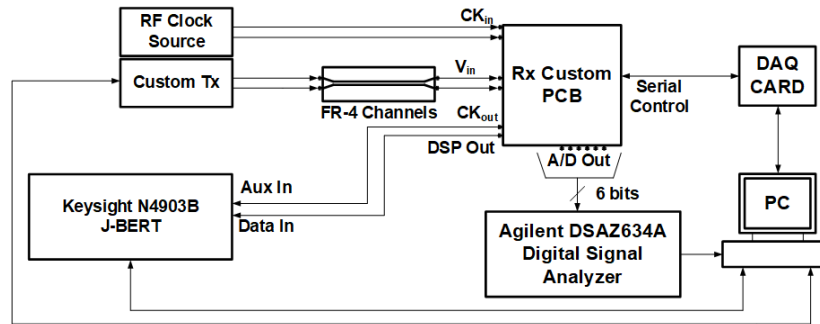
52Gbps Test Setup

Figure 4.28. Receiver characterization setup for 32Gb/s operation and 52Gb/s operation.

(a)

73
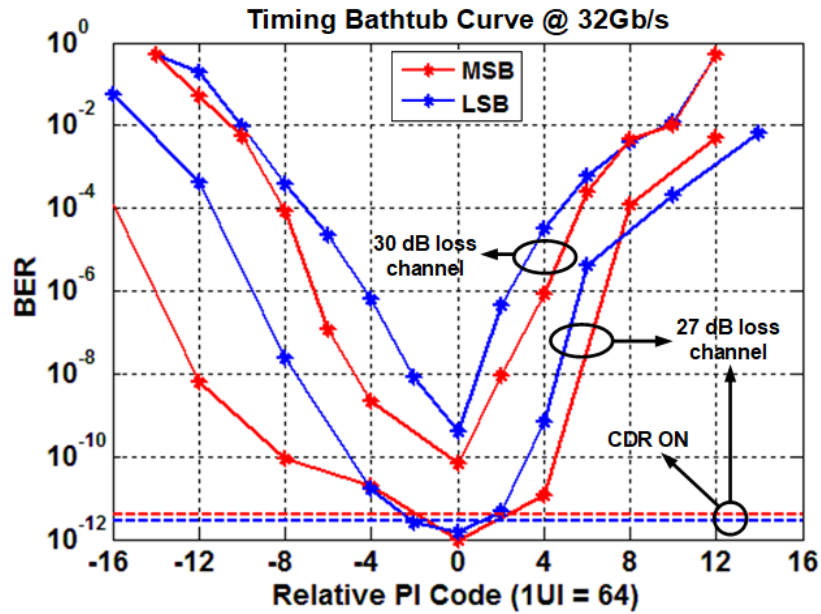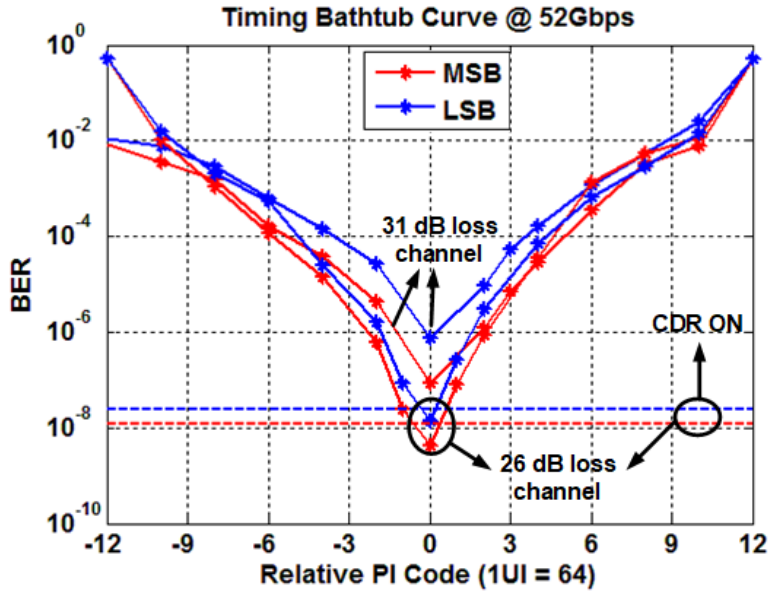
(b)

Figure 4.29. Measured timing bathtub curves for (a) 32Gb/s operation (and (b) 52Gb/s operation.
 (a) Reprinted with permission from S. Kiran et al, IEEE ©April 2018
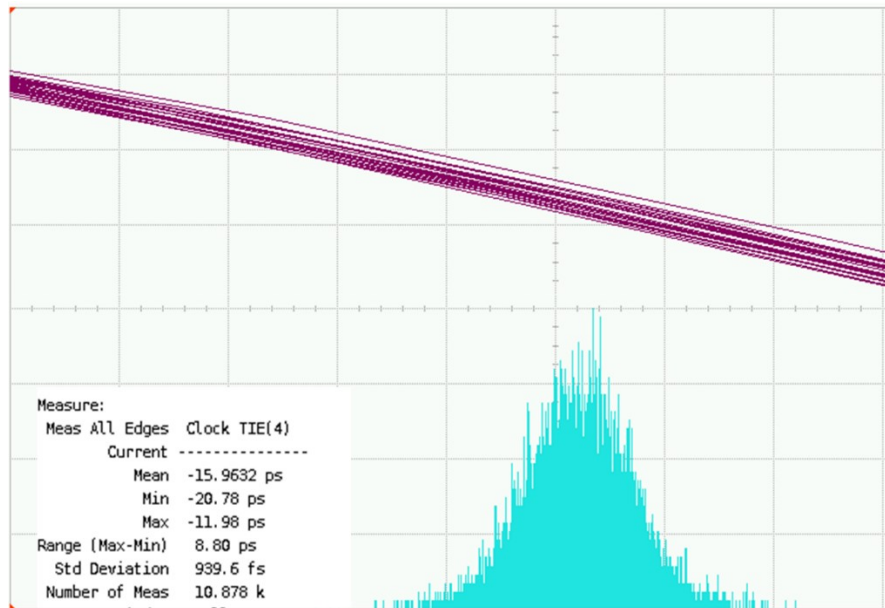
Figure 4.30. Measure recovered clock jitter histogram. Reprinted with permission from
S. Kiran et al, IEEE ©April 2018

74

Specification	Cui[2]	Frans[1]	Aurangozeb[4]	Upadhyaya[5]	Wang[6]	This Work
Technology	28 nm CMOS	16 nm FinFET	65 nm CMOS	16 nm FinFET	16 nm FinFET	65 nm CMOS
Power Supply (V)	N/A	0.9, 1.2 and 1.8	N/A	0.85, 0.9, 1.2 and 1.8	0.9 and 1.2	1.0 and 1.2
Maximum Data Rate (Gb/s)	32	56	28	56	64.375	52
ADC Sample Rate (GS/s)	16	28	14	28	32.1875	26
ADC Structure	TI-SAR	TI-SAR	TI-Flash	TI-SAR	Folding Flash	TI-SAR
Pre-Equalization	CTLE	CTLE	Passive Equalization	CTLE	CTLE	CTLE + 3-tap Embedded FFE
Post-Equalization	N/A	24-tap FFE + 1-tap DFE	3 to 8-tap FFE*	14-tap FFE + 1-tap DFE	16-tap FFE*	12-tap FFE + 2-tap DFE
Resolution (bit)	8	8	2 to 5.5	3 to 7	6	6
ENOB @ Nyquist	5.85	4.9	4.1	4.43	4.31	4.05
Area (mm^2)	0.89	N/A	0.2025	N/A	0.1625	2.62
Maximum Compensated Channel Loss (dB)	32 @ 8GHz	31 @ 14GHz	30 @ 7GHz	32 @ 14GHz	29.5 @ 16.09	31 @ 13GHz
Analog Front End + ADC Power (mW)	320	370	130	N/A	283.9	236
DSP Power (mW)	N/A	N/A	N/A	220	N/A	183

Power Efficiency (pJ/bit)													
AFE+ADC	DSP	10	N/A	6.61	N/A	4.64	N/A	N/A	3.9	4.41	N/A	4.54	3.52

* Off-chip

Table 4.2. Performance summary.

4.6 Conclusion

This chapter presented a 52 Gb/s PAM-4 receiver with a time-interleaved 6-bit SAR ADC with 2-bit/stage unit ADC and embedded 3-tap FFE. A new PU-DFE architecture reduces the PAM-4 DFE complexity to that of NRZ DFE to both provide reduced gate count and higher data rate operation. The receiver achieves a measured BER $< 10^{-6}$ with a 31 dB loss channel without employing any transmit equalization.

5. CONCLUSION AND FUTURE WORK

5.1 Conclusion

ADC-based receivers enable power digital equalization techniques to handle higher loss than mixed-signal receiver can. However, both the ADC and the DSP can be power hungry leading to worse power efficiency compared to mixed-signal receivers. Multi-level modulation schemes such as PAM-4 only further exacerbate this problem by introducing additional design challenges.

To tackle the power efficiency problem, accurate modeling of link systems and design techniques specific for multi-level modulation schemes are necessary. This dissertation first presented a hybrid statistical modeling framework that incorporates ADC specific errors such as quantization noise in the presence of non-linearity and residual ISI and time-interleaving ADC mismatch errors that can be utilized to study the trade-offs of different choices. The statistical techniques were verified with bit-by-bit transient simulations that showed excellent matching.

In the second part of this dissertation, a complete 52Gb/s PAM-4 receiver was presented that introduced a new DFE architecture called the partially-unrolled DFE (PU-DFE) that reduced the PAM-4 DFE complexity to that of PAM-2 DFE while simultaneously nearly doubling the maximum achievable data rate. The receiver was able to achieve a BER less than 10^{-6} while operating over a channel with 31dB loss with no transmit equalization. The receiver was also able to achieve a power efficiency of 8.06pj/bit when the entire front-end, ADC, and DSP power is considered.

In this chapter two additional ADC based receiver architectures, based on error correction and analog multi-tone modulation, will be described that has potential to achieve low power operation and increased jitter robustness as the unit interval shrinks, respectively.

5.2.1 Single Parity Check Code for ADC-Based Serial Link

Taking advantage of the partial equalization afforded by embedding a low-overhead linear equalizer in the ADC, previous work [11] has proposed dividing received symbols in to two categories: reliable and unreliable. Symbols falling close to decision threshold are classified as unreliable and symbols far away from the decision threshold as reliable. A significant amount of power can be saved in the DSP by enabling the equalizer to function only for the unreliable symbols and power gating it for the reliable symbols.

Building on this idea, if the transmitter inserts one parity check bit for every N-1 transmitted bits, the received symbols that are classified as unreliable can be discarded, i.e. treated as erasures and then can be filled up using the single parity check (SPC) condition. Thus every single bit erasure in a block of N bits can be filled up. If there are more than 2 erasures in a block, the block is not modified and probability of having an error in this block is the same as the pre-SPC BER. For this system, the post-SPC BER is given by

$$P_{error} = (1 - (P_{erase}{}^N + NP_{erase}(1 - P_{erase})^{N-1})) * P + P_2. \tag{5.1}$$

Here P_{error} is the post-SPC BER, P_{erase} is the probability of an unreliable symbol or erasure, P is the pre-SPC BER and P_2 is the probability that a symbol classified as reliable is erroneous. Equation 15 assumes that the probability of erasures for any symbol is independent of the other symbols. This is in general not true since the channel introduces correlation among the different symbols. In order to avoid correlations and burst errors, interleaving and de-interleaving

becomes necessary as shown in Fig. 5.1 [35]. Finally, the impact of SPC on ADC-resolution in shown in Fig. 5.2. Fig. 5.2 shows the improvement in BER with the proposed erasure filling scheme for different ADC resolutions. For a target BER of 10^{-12} at a data rate of 64Gb/s, up to 2 bits of ADC resolution can be saved using the proposed scheme. The simulation results in Fig. 5.2 assume a transmit swing of 0.9 V_{ppd} and a noise sigma of 2.5mV at the ADC input. Equalization in the analog domain is provided by a CTLE and a 3-tap embedded FFE. Equalization in the digital domain is provided by a 15-tap FFE.
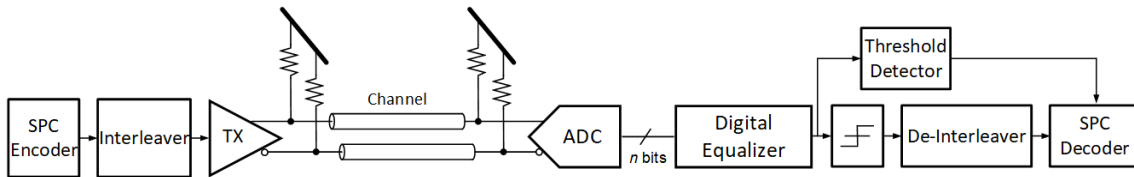
Figure 5.1. Transceiver architecture for implementing a single parity check code based architecture. Interleaving and de-interleaving are employed to avoid burst errors.
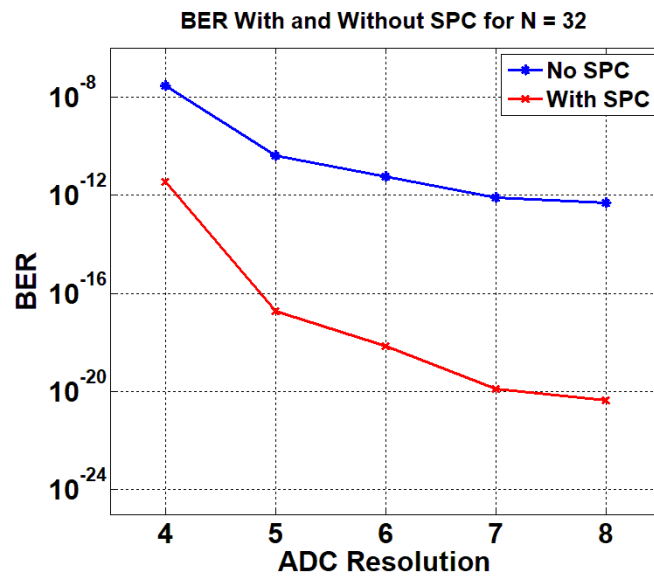
Figure 5.2. BER vs ADC resolution with and without SPC code based erasure filling scheme.

5.2.2 Frequency Domain ADC-Based Serial Link Receiver Architecture

As the high-speed data symbol times shrink, transmission over both severe low-pass electrical channels and dispersive optical channels result in significant inter symbol interference. This necessitates increased equalization complexity, consideration of more bandwidth-efficient modulation schemes, such as baseband PAM4 and coherent QAM, and the use of forward error correction. Serial links that utilize an analog-to-digital converter (ADC) receiver front-end offer a potential solution, as they enable more powerful and flexible digital signal processing (DSP) for equalization and symbol detection and can easily support advanced modulation schemes. Unfortunately, sampling clock jitter places fundamental performance limitations on common time-interleaved ADC architectures, necessitating clock generation and distribution circuitry that achieve rms jitter of a few hundred femtoseconds. Jitter degrades performance in these systems because, although the sampling clocks of a time-interleaved ADC run at a fraction of the Nyquist-rate frequency, every channel still produces jitter-induced noise from sampling the full input-signal bandwidth, whose power is given $\sigma_n^2 = \left(\sqrt{2}\pi BA\sigma_j\right)^2$, where B and A are the signal bandwidth and amplitude, respectively. Therefore, although the sampling rate in each channel of a time-interleaved ADC is relaxed by the number of channels, the jitter requirement is the same as in a single-channel ADC. By limiting the signal bandwidth at the sampler, as in an OFDM system, significant jitter robustness can be achieved since for an N-channel receiver the jitter induced noise is $\sigma_n^2 = \left(\sqrt{2}\pi BA\sigma_j/N\right)^2$ [36].

This section presents architectures that are robust to jitter by either employing multiple channels with increased symbol period time or by splitting a conventional PAM-M baseband signal in to multiple frequency channels before the ADC samples the input signals.

Fig. 5.3 shows the proposed frequency-domain ADC-based receiver. The input CTLE drives the front-end channels that have a mixer for down-conversion, a Bessel low-pass filter, and an ADC for sampling and digitization. These digitized samples are then processed by the FIR filters in the DSP and their outputs are combined to either perform symbol estimation in PAM-4 baseband mode or to perform both inter-channel interference (ICI) and ISI cancellation in multi-tone mode. The receiver can handle either a baseband modulated signal such as PAM-4 modulation or a multi-tone signal comprising of a combination of baseband and 1 or more QAM signals.
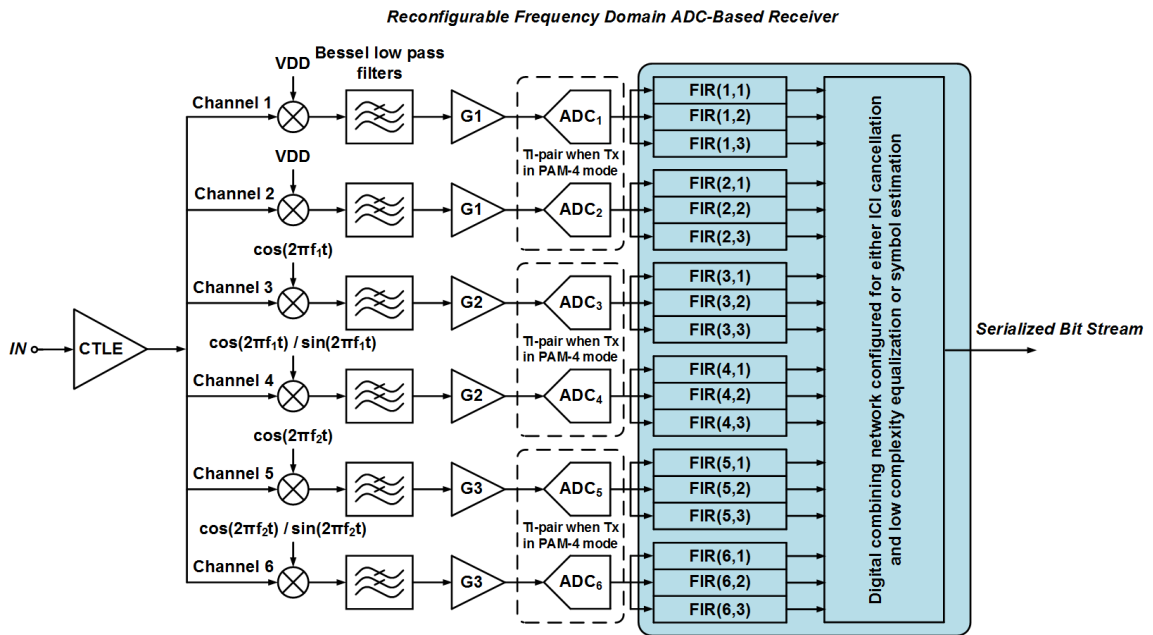
Figure 5.3. Analog multi-tone modulation reconfigurable receiver.

When the input signal is baseband modulated, the receiver acts a frequency channelizing receiver. For a 128Gb/s receiver employing PAM-4 modulation with a symbol rate of 64GS/s, the receiver is configured as a 3-channel frequency channelizing receiver. The ADC pairs in two adjacent channels are configured to works as a time-interleaved ADC. The first two mixers act as

dummy mixers and Bessel low pass filters pass only the low frequency content of the signal through to the ADC to be digitized. The next set of mixers in channel 3 and channel 4 employ an LO frequency of 21.33 GHz which is 1/3rd the baud rate. The final set of mixers in channel 5 and channel 6 employ an LO frequency of 32 GHz which ½ the baud rate. The LO frequencies are an integer ratio of the baud rate to make the sampled system LTI [37]. The architecture is similar to a hybrid filter bank ADC with the key difference being that the digital reconstruction filter performs direct symbol estimation and does not implement the perfect reconstruction FIR filters [38]. The mixer is followed by a low pass filter with the jitter robustness increasing as the order of the filter increases. The 5th order low pass filter is a practical choice.

A 128 Gb/s multi-tone signaling scheme can employ 5 12.8 GS/s channels consisting of 1 baseband PAM-4 channel, 1 QAM-64 channel centered at 25.6 GHz and 1 QAM-4 channel centered at 51.2 GHz. In this scenario the receiver employs channel 1 for receiving the baseband PAM-4 signal with channel 3 and channel 4 employed for the QAM-64 signal and channel 5 and channel 6 utilized for the QAM-4 signal. Channel 2 is disabled in this operation mode. Fig.5.4 shows the signal PSD at the transmitter and a channel having 30 dB loss at 32 GHz which is used to present the simulation results.

Fig. 5.5 shows the jitter robustness comparison for a traditional time-interleaved system, PAM-4 baseband modulation system, the 5-channel multi-tone signal described in the previous section and a QAM-32 system. For a target BER of 10^{-12}, the Fig. 5.5 shows that the 128 Gb/s frequency channelized PAM-4 receiver provides 1.6X improvement in jitter robustness compared to the time-interleaved system. The 5-channel multi-tone signal provides close to 6X improvement while the QAM-32 system provides about 3X improvement. The improvement in jitter robustness for the 128 GS/s PAM-4 system comes from the fact that the input signal is frequency channelized

into 3-channels before it is sampled. The high frequency attenuation provided by the 5th order Bessel low pass filter reduces the signal bandwidth and improves the jitter robustness. For the 5-channel multi-tone signal the improvement in jitter robustness comes from a combination of 2 effects. First, the lower symbol rate of 12.8 GS/s results in a wider pulse compared to the PAM-4 time-interleaved system and this leads to reduced timing sensitivity. This is illustrated in Fig. 5.6. Second, the mixer self-equalization [39] results in the sampler's input signal being equalized and hence the residual ISI contribution from a sub-optimal sampling point is greatly reduced. This is evident in the multi-tone pulse response in Fig. 5.6 for channel 3 and channel 5. The jitter robustness of QAM-32 system is due to the same reason as the 5-channel multi-tone system. However, the QAM-32 system has a higher symbol rate of 25.6 GS/s and hence is more susceptible to jitter. It should be noted that the simulation results of Fig. 5.5 also assume an equal jitter on the mixer LO clocks.
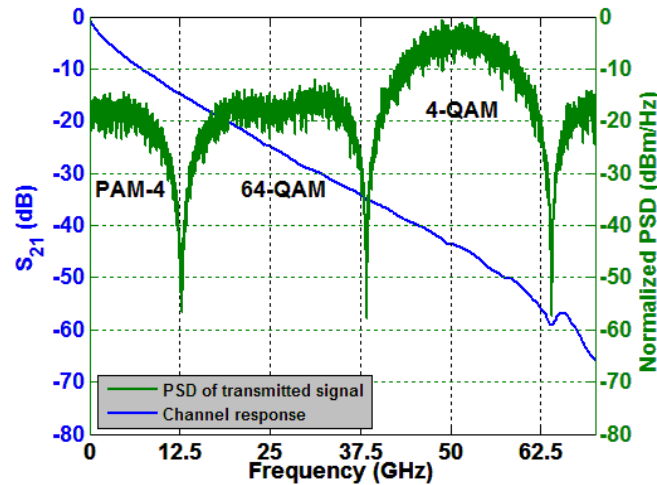
Figure 5.4. Channel response and 5-channel multitoned analog modulated signal.
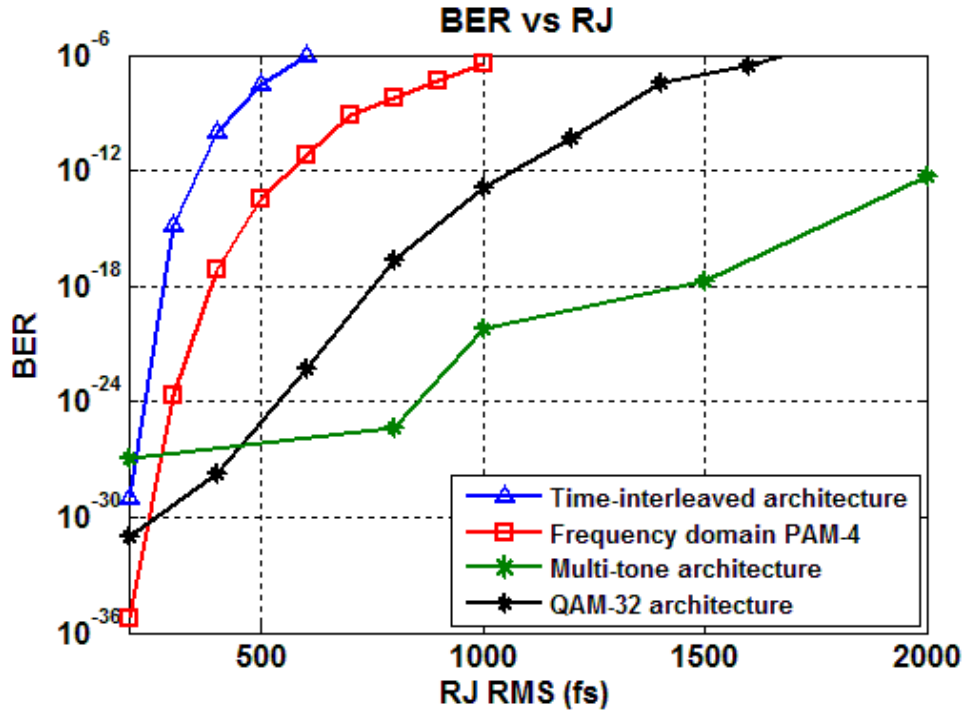
Figure 5.5. Jitter robustness comparison for different modulation schemes.
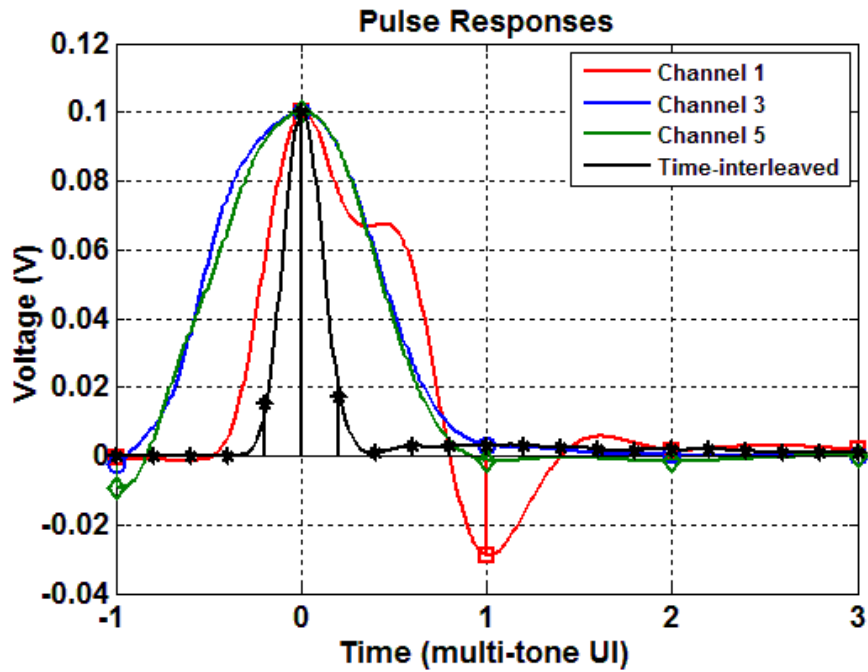
Figure 5.6. Pulse response 128 Gb/s PAM-4 and 5-channel multi-tone modulation.

83

In summary, an ADC-based frequency domain receiver can be configured for either a baseband PAM-4 modulated signal or for a 5-channel multi-tone modulation scheme employing 1 PAM-4 channel and 2 QAM channels. Simulation results show the improved jitter robustness in comparison with a traditional time-interleaved receiver with up to 6X improvement for the 5-channel multi-tone system.

REFERENCES

1. Y. Frans *et al.*, "A 56-Gb/s PAM4 Wireline Transceiver Using a 32-Way Time-Interleaved SAR ADC in 16-nm FinFET," in *IEEE Journal of Solid-State Circuits*, vol. 52, no. 4, pp. 1101-1110, April 2017.

2. D. Cui *et al.*, "3.2 A 320mW 32Gb/s 8b ADC-based PAM-4 analog front-end with programmable gain control and analog peaking in 28nm CMOS," *2016 IEEE International Solid-State Circuits Conference (ISSCC)*, San Francisco, CA, 2016, pp. 58-59.

3. S. Rylov *et al.*, "3.1 A 25Gb/s ADC-based serial line receiver in 32nm CMOS SOI," *2016 IEEE International Solid-State Circuits Conference (ISSCC)*, San Francisco, CA, 2016, pp. 56-57.

4. Aurangozeb, A. D. Hossain, M. Mohammad and M. Hossain, "Channel-Adaptive ADC and TDC for 28 Gb/s PAM-4 Digital Receiver," in *IEEE Journal of Solid-State Circuits*, vol. 53, no. 3, pp. 772-788, March 2018.

5. P. Upadhyaya *et al.*, "A fully adaptive 19-to-56Gb/s PAM-4 wireline transceiver with a configurable ADC in 16nm FinFET," *2018 IEEE International Solid - State Circuits Conference - (ISSCC)*, San Francisco, CA, 2018, pp. 108-110.

6. L. Wang, Y. Fu, M. LaCroix, E. Chong and A. C. Carusone, "A 64Gb/s PAM-4 transceiver utilizing an adaptive threshold ADC in 16nm FinFET," *2018 IEEE International Solid - State Circuits Conference - (ISSCC)*, San Francisco, CA, 2018, pp. 110-112.

7. B. Casper, M. Haycock, and R. Mooney, "An accurate and efficient analysis method for multi-Gb/s chip-to-chip signaling schemes," in *Proc. IEEE Symp. VLSI Circuits*, June 2002, pp. 54–57.

8. K. S. Oh, F. Lambrecht, S. Chang, Q. Lin, J. Ren, C. Yuan, J. Zerbe, and V. Stojanovic, "Accurate System Voltage and Timing Margin Simulation in High-Speed I/O System Designs," *IEEE Trans. Adv. Pack.*, vol. 31, no. 4, pp. 722–730, Nov. 2008.

9. G. Balamurugan, B. Casper, J. Jaussi, M. Mansuri, F. O'Mahony, and J. Kennedy, "Modeling and analysis of high-speed I/O links," *IEEE Trans. Adv. Pack.*, vol. 32, no. 2, pp. 237–247, May 2009.

10. A. Sanders, M. Resso, and J. DAmbrosia, "Channel compliance testing utilizing novel statistical eye methodology," presented at the DesignCon, Santa Clara, CA, 2004.

11. A. Shafik, E. Zhian Tabasy, S. Cai, K. Lee, S. Hoyos and S. Palermo, "A 10 Gb/s Hybrid ADC-Based Receiver With Embedded Analog and Per-Symbol Dynamically Enabled Digital Equalization," in *IEEE Journal of Solid-State Circuits*, vol. 51, no. 3, pp. 671-685, March 2016.

12. X. Gu, K. J. Han, M. Cracraft, R. R. Donadio and Y. Kwark, "Efficient parametric modeling and analysis for backplane channel characterization," *2012 IEEE 62nd Electronic Components and Technology Conference*, San Diego, CA, 2012, pp. 1880-1885.

13. Y. Frans *et al*., "A 0.5–16.3 Gb/s Fully Adaptive Flexible-Reach Transceiver for FPGA in 20 nm CMOS," in *IEEE Journal of Solid-State Circuits*, vol. 50, no. 8, pp. 1932-1944, Aug. 2015.

14. A. Momtaz and M. M. Green, "An 80 mW 40 Gb/s 7-Tap T/2-Spaced Feed-Forward Equalizer in 65 nm CMOS," in *IEEE Journal of Solid-State Circuits*, vol. 45, no. 3, pp. 629-639, March 2010.

15. R. Boesch, K. Zheng, and B. Murmann, "A 0.003 mm2 5.2 mw/tap 20 gbd inductor-less 5-tap analog rx-ffe," in *IEEE Symp. VLSI Circuits Dig. Tech. Papers*, June 2016, pp. 170–171.

16. E. Zhian Tabasy, A. Shafik, K. Lee, S. Hoyos, and S. Palermo, "A 6 bit 10 GS/s TI-SAR ADC with low-overhead embedded FFE/DFE equalization for wireline receiver applications," IEEE J. Solid-State Circuits, vol. 49, no. 11, pp. 2560–2574, Nov. 2014.

17. S. Kasturia and J. H. Winters, "Techniques for high-speed implementation of nonlinear cancellation," Selected Areas in Communications, IEEE Journal on, vol. 9, no. 5, pp. 711–717, 1991.

18. K. Parhi, "Design of Multigigabit Multiplexer-Loop-Based Decision Feedback Equalizers," *IEEE Trans. Very Large Scale Integr. (VLSI) Syst.*, vol. 13, no. 4, pp. 489-493, Apr. 2005.

19. P. Newaskar, R. Blazquez, and A. Chandrakasan, "A/D precision requirements for an ultra-wideband radio receiver," in *IEEE Workshop on Signal Processing Systems*, Oct 2002, pp. 270–275.

20. A. Hadji-Abdolhamid and D. Johns, "A 400-MHz 6-bit adc with a partial analog equalizer for coaxial cable channels," in Proc. European Solid-State Circuits Conference, Sept 2003, pp. 237–240.

21. G. Malhotra, "Method for analytically calculating BER (bit error rate) in presence of non-linearity," DesignCon, Santa Clara, Jan. 28-31, 2014.

22. Widrow, I. Kollar, and M.-C. Liu, "Statistical theory of quantization," *IEEE Trans. Instrum. Meas.*, vol. 45, no. 2, pp. 353–361, Apr 1996.

23. Vogel, "The impact of combined channel mismatch effects in time-interleaved ADCs," *IEEE Trans. Instrum. Meas.*, vol. 54, no. 1, pp. 415–427, Feb. 2005.

24. R. M. Gray, "Toeplitz and circulant matrices: A review," *Foundations and Trends in Communications and Information Theory*, vol. 2, no. 3, pp. 155–239, 2006.

25. R. G. Carvajal et al., "The flipped voltage follower: a useful cell for low-voltage low-power circuit design," in *IEEE Transactions on Circuits and Systems I: Regular Papers*, vol. 52, no. 7, pp. 1276-1291, July 2005.

26. R. Nonis, E. Palumbo, P. Palestri and L. Selmi, "A Design Methodology for MOS Current-Mode Logic Frequency Dividers," in *IEEE Transactions on Circuits and Systems I: Regular Papers*, vol. 54, no. 2, pp. 245-254, Feb. 2007.

27. R. Kreienkamp, U. Langmann, C. Zimmermann, T. Aoyama and H. Siedhoff, "A 10-gb/s CMOS clock and data recovery circuit with an analog phase interpolator," in *IEEE Journal of Solid-State Circuits*, vol. 40, no. 3, pp. 736-743, March 2005.

28. J. L. Sonntag and J. Stonick, "A Digital Clock and Data Recovery Architecture for Multi-Gigabit/s Binary Links," in *IEEE Journal of Solid-State Circuits*, vol. 41, no. 8, pp. 1867-1875, Aug. 2006.

29. K. Mueller and M. Muller, "Timing Recovery in Digital Synchronous Data Receivers," in *IEEE Transactions on Communications*, vol. 24, no. 5, pp. 516-531, May 1976.

30. K. Gopalakrishnan *et al.*, "3.4 A 40/50/100Gb/s PAM-4 Ethernet transceiver in 28nm CMOS," *2016 IEEE International Solid-State Circuits Conference (ISSCC)*, San Francisco, CA, 2016, pp. 62-63.

31. Z. Cao, S. Yan and Y. Li, "A 32mW 1.25GS/s 6b 2b/step SAR ADC in 0.13μm CMOS," *2008 IEEE International Solid-State Circuits Conference - Digest of Technical Papers*, San Francisco, CA, 2008, pp. 542-634.

32. T. Jiang, W. Liu, F. Y. Zhong, C. Zhong, K. Hu and P. Y. Chiang, "A Single-Channel, 1.25-GS/s, 6-bit, 6.08-mW Asynchronous Successive-Approximation ADC With Improved Feedback Delay in 40-nm CMOS," in *IEEE Journal of Solid-State Circuits*, vol. 47, no. 10, pp. 2444-2453, Oct. 2012.

33. C. H. Chan, Y. Zhu, S. W. Sin, S. P. U and R. P. Martins, "A 3.8mW 8b 1GS/s 2b/cycle interleaving SAR ADC with compact DAC structure," *2012 Symposium on VLSI Circuits (VLSIC)*, Honolulu, HI, 2012, pp. 86-87.

34. V. Hariprasath, J. Guerber, S. H. Lee and U. K. Moon, "Merged capacitor switching based SAR ADC with highest switching energy-efficiency," in *Electronics Letters*, vol. 46, no. 9, pp. 620-621, April 29 2010.

35. R. L. Narasimha, N. R. Shanbhag. "Design of energy-efficient high-speed links via forward error-correction (FEC)," IEEE Transactions on Circuits and Systems-II, vol. 57,no. 5, pp. 359- 363, May 2010.

36. S. Hoyos *et al*., "Clock-Jitter-Tolerant Wideband Receivers: An Optimized Multichannel Filter-Bank Approach," in *IEEE Transactions on Circuits and Systems I: Regular Papers*, vol. 58, no. 2, pp. 253-263, Feb. 2011.

37. A. Amirkhany *et al*., "A 24 Gb/s Software Programmable Analog Multi-Tone Transmitter," in *IEEE Journal of Solid-State Circuits*, vol. 43, no. 4, pp. 999-1009, April 2008.

38. Won Namgoong, "A channelized digital ultrawideband receiver," in *IEEE Transactions on Wireless Communications*, vol. 2, no. 3, pp. 502-510, May 2003.

39. W. H. Cho *et al*., "10.2 A 38mW 40Gb/s 4-lane tri-band PAM-4 / 16-QAM transceiver in 28nm CMOS for high-speed Memory interface," *2016 IEEE International Solid-State Circuits Conference (ISSCC)*, San Francisco, CA, 2016, pp. 184-185.